

Colloids as model systems for condensed matter

Investigation of structural and dynamical properties of colloidal
systems using digital video microscopy and optical tweezers

Von der Fakultät Mathematik und Physik der Universität Stuttgart
zur Erlangung der Würde eines Doktors der
Naturwissenschaften (Dr. rer. nat.) genehmigte Abhandlung

vorgelegt von

Jörg Baumgartl

aus Basel (CH)

Hauptberichter: Prof. Dr. Clemens Bechinger

Mitberichter: Prof. Dr. Tilman Pfau

Tag der Einreichung: 8. Mai 2007

Tag der mündlichen Prüfung: 13. Juni 2007

Physikalisches Institut der Universität Stuttgart
2007

Contents

List of abbreviations	5
Zusammenfassung	7
Chapter 1. Abstract and general introduction	11
Chapter 2. Colloids as model systems	15
2.1. Definition of colloids	16
2.2. Colloids as model systems for atomic systems	16
2.3. Characterization of colloidal physics	17
2.4. Pair interaction in colloidal systems	18
2.5. Interaction of colloidal particles with strong external light-fields	21
Chapter 3. Experimental setup	25
3.1. Creation of 1D periodic potentials	26
3.1.1. Basics	26
3.1.2. Optical setup	28
3.1.3. Calibration of the substrate potential	29
3.1.4. Creation of more complex substrate potentials	31
3.2. Digital video microscopy	31
3.2.1. Video microscopical setup	31
3.2.2. Particle detection	33
3.3. Preparation of two-dimensional systems	35
3.4. Adjusting the density of colloidal systems	36
3.5. Sample cells	38
3.6. Adjusting the pair interaction of colloidal systems	39
Chapter 4. Phonon-dispersion-relation of two-dimensional crystals on substrate potentials	41
4.1. Introduction	42
4.2. Basic formalism and state of the art	43
4.3. Theoretical approach	49
4.4. Experimental approach	51
4.5. Theoretical and experimental results	53
4.6. Relevance of the results for atomic crystals	59

4.7. Summary and conclusions	61
4.8. Appendix: phonon dynamics	62
4.9. Appendix: Measurement of lattice sites	66
Chapter 5. Structural crossover in binary hard sphere mixtures	69
5.1. Introduction	70
5.2. Theoretical approach	71
5.3. Experimental method and data analysis	74
5.4. Experimental results	77
5.5. Connectivity analysis	81
5.6. MC-simulations: structural crossover at different q and η	84
5.7. Conclusions and outlook	86
5.8. Appendix: limitations of the experimental method	88
Chapter 6. Subdiffusive Brownian motion of colloidal particles on quasicrystalline substrates	91
6.1. Introduction	92
6.2. Experimental method	93
6.3. Experimental results and discussion	96
6.4. Theoretical methods and results	100
6.5. Conclusions and outlook	106
Chapter 7. New insight on the nature of confinement-induced like-charge attraction	109
7.1. Introduction	110
7.2. Experimental evidence of confinement-induced LCA	111
7.3. Experimental method and data analysis	112
7.4. Results and discussion	115
7.5. Methods to avoid optical distortions	121
7.6. Optical binding	123
7.7. Conclusions	125
Chapter 8. Summary	127
Bibliography	129
Acknowledgement	139

List of abbreviations

- 2D: two dimensions, two-dimensional
- 3D: three dimensions, three-dimensional
- KTHNY: Kosterlitz Thouless Halperin Nelson Young
- PY: Percus Yevick
- HNC: hypernetted chain
- 1D: one dimension, one-dimensional
- Nd: Neodym
- Y: Yttrium
- O: Oxygen
- CCD: charge-coupled device
- BZ: Brillouin zone
- MSD: Mean-square displacement
- DFT: Density functional theory
- MC: Monte-Carlo
- LCA: Like-charge attraction
- DLVO: Derjaguin Landau Verwey Overbeek
- OB: Optical binding

Zusammenfassung

Als kolloidale Suspensionen werden Flüssigkeiten bezeichnet, in denen Teilchen mit einer Größe zwischen 10nm und $10\mu\text{m}$ dispergiert sind. Neben ihrer technischen Relevanz für Dispersionsfarben, Gele, Öle oder Dämpfungsflüssigkeiten eignen sich kolloidale Systeme hervorragend als Modellsysteme für Vorgänge in Festkörpern bzw. Flüssigkeiten oder allgemein im Bereich der statistischen Physik. Das liegt daran, dass kolloidale und atomare Systeme – letztere bei hinreichend hohen Temperaturen – der Boltzmannstatistik gehorchen und daher vergleichbares Phasenverhalten zeigen. Aufgrund der mesoskopischen Teilchengröße können kolloidale Systeme mit optischen Videomikroskopen untersucht werden. Dadurch ist es möglich, das Verhalten einzelner Teilchen sichtbar zu machen. Bei Experimenten auf atomarer Skala ist dies nicht möglich, weil mit den hier angewendeten Streumethoden nur über alle Teilchen gemittelte Größen bestimmt werden können. Rasterkraft- und Rastertunnelmikroskopie können zwar einzelne Atome auflösen, aber diese Verfahren sind invasiv, d.h. üben Kräfte auf die untersuchten Systeme aus.

Neben der direkten Untersuchung einzelner Teilchen erlauben kolloidale Systeme, dynamische Vorgänge wie die Kristallisationskinetik zeitlich aufzulösen. Dies ist in atomaren Systemen in der Regel so nicht möglich. Des Weiteren kann in kolloidalen Systemen die Paarwechselwirkung maßgeschneidert werden. Je nach Beschaffenheit können kolloidale Teilchen zum Beispiel über Harte-Kugel-, magnetische Dipol-Dipol- oder – wie in unseren Experimenten – abgeschirmte Coulombpotenziale wechselwirken. Die Stärke der beiden letztgenannten Potenziale lässt sich dabei kontrolliert und kontinuierlich variieren. Zusätzlich zur Paarwechselwirkung kann auch die Substrat-Teilchen-Wechselwirkung maßgeschneidert werden. In diesem Zusammenhang haben sich optische Pinzetten als sehr nützlich erwiesen. Optische Pinzetten erzeugen mit Hilfe von Laserlicht sehr große elektrische Feldgradienten, die dielektrische kolloidale Teilchen in Bereiche maximaler Feldstärke treiben und dort fangen. Ausgedehnte lichtinduzierte Substratpotenziale lassen sich – wie in unseren Experimenten – mit überlappenden und aufgeweiteten Laserstrahlen realisieren.

Wir haben in diesem Rahmen die Struktur und die Dynamik kondensierter Materie in vier unabhängigen, theoretischen und experimentellen Studien untersucht, die im Folgenden zusammengefasst werden. In den Experimenten werden grundsätzlich mit einem Video- oder einem konfokalen Mikroskop Teilchentrajektorien aufgenommen und

daraus die interessierenden physikalischen Größen wie Korrelationsfunktionen, Wechselwirkungen oder mittlere Verschiebungsquadrate bestimmt.

1. *Phononen-Dispersionsrelation von zweidimensionalen Kristallen auf Substratpotenzialen.* Es ist allgemein bekannt, dass Schwingungen von Kristallgittern durch die harmonische Näherung beschrieben werden können. Die Paarwechselwirkung wird im Rahmen dieser Näherung durch Federn modelliert, und die kollektiven Gitterschwingungen separieren dadurch in unabhängige harmonischen Oszillatoren, die Phononen genannt werden. Die Wellenvektoren der Phononen und die Fourier-Amplituden der Federkonstanten werden durch die phononische Bandstruktur zueinander in Beziehung gesetzt. Die phononische Bandstruktur hat maßgeblich Einfluss auf Schallausbreitung und thermische Eigenschaften wie spezifische Wärme oder Wärmeleitfähigkeit. Um herauszufinden, ob phononische Bandstrukturen durch externe Potenziale gezielt modifiziert werden können, haben wir die harmonische Näherung auf einen zweidimensionalen hexagonalen Kristall angewendet, der sich auf einem periodischen Substratpotenzial befindet. Wir beschränkten uns auf kommensurable Substrate, bei denen sich jedes Kristallteilchen in einem Minimum des Substrats befindet. Unsere Ergebnisse zeigen, dass sich Bänder gezielt verschieben und deformieren lassen. Es ist damit tatsächlich möglich, Schallausbreitung und thermische Eigenschaften mit einem Substrat zu beeinflussen. Darüber hinaus kann eine Bandlücke erzeugt werden. Das bedeutet, dass es Frequenzbereiche gibt, in denen Schall nicht in den Kristall eindringen kann, sondern reflektiert wird. Um unsere theoretischen Ergebnisse experimentell zu verifizieren, haben wir einen Kolloidkristall präpariert und verschiedene lichtinduzierte Substrate durch interferierende Laserstrahlen realisiert. Die phononische Bandstruktur erhielten wir durch eine Fourier-Analyse der mit Videomikroskopie aufgenommenen Trajektorien. Die experimentellen Ergebnisse bestätigen die theoretischen Resultate.
2. *Struktureller Übergang in binären Mischungen von harten Kugeln.* Wir haben mit konfokaler Mikroskopie die strukturellen Eigenschaften einer binären Mischung aus Kolloidteilchen untersucht. Die Kolloidteilchen wechselwirken über ein Harte-Kugel-Potenzial und haben ein Größenverhältnis von 0.61. Wir haben, ausgehend von einem System aus ausschließlich großen Teilchen, bei konstanter totaler Packungsdichte sukzessive den Anteil an kleinen Teilchen erhöht und jeweils die radiale Paarkorrelationsfunktion bestimmt. Es ist bei asymmetrischen Mischungen, in denen entweder die große oder die kleine Partikelsorte dominiert, intuitiv klar, dass die radiale Paarkorrelationsfunktion ungefähr auf dem großen bzw. dem kleinen Teilchendurchmesser, d.h. der dominierenden Längenskala oszilliert. Die gemessenen Paarkorrelationsfunktionen zeigen, dass dies erstaunlicherweise für alle realisierten Mischungsverhältnisse von großen und kleinen Teilchen gilt, und wir beobachten für wachsenden Anteil an kleinen Teilchen einen scharfen Übergang von der großen zur

kleinen Längenskala. Dieses Verhalten bezeichnet man als strukturellen Übergang und wurde von theoretischen Arbeiten vorhergesagt. Wir haben zusätzlich untersucht, wie sich der strukturelle Übergang auf die Konfiguration von großen und kleinen Partikeln auswirkt. Dazu haben wir mit einer Triangulation Bindungen zwischen nächsten Nachbarpartikeln der gleichen Sorte bestimmt. Als Ergebnis sehen wir für die asymmetrischen Mischungen Netzwerke aus ausschließlich großen bzw. kleinen Partikeln, die bis zum strukturellen Übergang hin über das ganze System ausgedehnt sind und dort abrupt aufgebrochen werden. Dies haben wir auch in Monte-Carlo-Simulationen beobachtet, die für verschiedene Größenverhältnisse und totale Packungsdichten der Teilchen durchgeführt wurden. Mit diesen Ergebnissen hoffen wir, zum Verständnis des komplexen Verhaltens von realer Materie beizutragen, die sich meist aus Bausteinen unterschiedlicher Größe zusammensetzt.

3. *Subdiffusive Brownsche Bewegung von kolloidalen Teilchen auf quasikristallinen Substratpotenzialen.* Wir haben die diffusive Bewegung von Kolloiden auf lichtinduzierten, quasikristallinen Substratpotenzialen mit fünf-zähliger Symmetrie untersucht. Das Substratpotenzial wurde mit fünf schräg einfallenden und dann überlappenden Laserstrahlen erzeugt. Benachbarte Strahlen hatten dabei einen Winkel von 72° zueinander. Um die Diffusion zu analysieren, haben wir das mittlere Verschiebungsquadrat aus den für verschiedene Laserintensitäten und mit Videomikroskopie gemessenen Trajektorien bestimmt. Als Ergebnis beobachten wir einen Bereich, in dem das mittlere Verschiebungsquadrat in der Zeit mit einer Potenz kleiner als eins, also langsamer als im Fall von normaler Diffusion, ansteigt. Dieses Verhalten wird als subdiffusiv bezeichnet. Das subdiffusive Verhalten kann als Thermalisierungsprozess auf dem quasikristallinen Substrat aufgefasst werden. Dieses hat nämlich eine charakteristische Verteilung der Tiefen der Potenzialtöpfe, und ein Teilchen muss diese Verteilung durch Diffusion erkunden, um zu thermalisieren. Das erklärt auch unsere Beobachtung, dass der subdiffusive Bereich mit wachsender Substratstärke länger anhält; das diffundierende Teilchen wird länger in den Töpfen gefangen und braucht daher länger, um zu thermalisieren. In Übereinstimmung mit dieser Interpretation wachsen die gemessenen mittleren Verschiebungsquadrate wieder normal, d.h. linear in der Zeit, wenn der Thermalisierungsprozess beendet ist. Unsere Ergebnisse stimmen qualitativ gut mit theoretischen Resultaten überein, die durch Simulationen und Lösen von Ratengleichungen erhalten wurden. Subdiffusion spielt eine wichtige Rolle in Gläsern und organischen Zellen. Unser Teilchen-Substrat-Modellsystem erlaubt, Subdiffusion in Abhängigkeit von einer kontinuierlich variierbaren Wechselwirkung zu untersuchen.
4. *Neue Erkenntnisse über die Ursache der Attraktion zwischen gleichnamigen Ladungen in eingeschränkten Geometrien.* Die Paarwechselwirkung in ladungsstabilisierten

kolloidalen Suspension ist, abgesehen von einer sehr kurzreichweitigen van-der-Waals-Wechselwirkung, rein repulsiv. Mehrere Gruppen haben allerdings unabhängig voneinander eine langreichweitige Anziehung zwischen kolloidalen Teilchen beobachtet, wenn sich die Teilchen zwischen zwei Glasplatten (Abstand etwas größer als der Teilchendurchmesser) befanden. Dieses Phänomen konnte nicht erklärt werden. In unserer experimentellen Untersuchung haben wir zwei Teilchen in einem leicht defokussierten Laserstrahl gefangen, die Verteilung der Teilchenabstände gemessen und daraus die Paarwechselwirkung bestimmt. Unsere Ergebnisse zeigen, dass die ungewöhnliche attraktive Wechselwirkung von einem optischen Artefakt herrührt, der systematische Fehler in den mit Videomikroskopie gemessenen Abständen verursacht. Wir konnten diesen systematischen Fehler ausmessen und die Paarpotenziale korrigieren. Als Ergebnis erhielten wir eine rein repulsive Paarwechselwirkung, die perfekt mit der in ladungsstabilisierten Suspensionen erwarteten, Yukawa-artigen Wechselwirkung übereinstimmt. Der optische Artefakt rührt von überlappenden Teilchenbildern her, die ungefähr doppelt so groß wie die Teilchen selbst sind. Wir können außerdem erklären, warum die scheinbare attraktive Wechselwirkung nur in sehr dünnen Messzellen beobachtet wurde. Die repulsive Yukawa-artige Wechselwirkung wird in dünnen Zellen sehr stark abgeschirmt, weil durch das kleine Zellenvolumen die Konzentration an Salzionen sehr hoch ist. Dadurch kommt es dann zum Überlapp der Teilchenbilder. Wir haben die scheinbare Attraktion folgerichtig auch in dicken Zellen bei hinreichender Zugabe von Salz beobachtet.

1

Abstract and general introduction

Colloidal physics is an interdisciplinary field of research which has attracted considerable and persistently increasing interest during the last three decades. Colloids consist of particles which have a typical size between $10nm$ and $10\mu m$ and which are dispersed in a liquid. Besides the technological relevance for dispersion paints, oils, gels and damping fluids, colloids serve as model systems for complex atomic systems due to the thermodynamic affinity. Physical processes are governed by Boltzmann statistics on both the colloidal and – at sufficiently high temperatures – the atomic scale; colloidal and atomic systems therefore e.g. exhibit comparable phase behavior. The major benefit of colloidal systems arises from the mesoscopic particle size which allows convenient and non-invasive particle imaging with optical microscopes. One is therefore not restricted to the analysis of averaged physical quantities as typically obtained in scattering experiments on atomic matter. Moreover, particle-particle and particle-substrate interactions in colloidal systems can be both realized in a large variety and modified continuously. In particular, optical tweezers provide a powerful tool to induce particle-substrate interactions through the use of modern laser technology.

A multitude of both theoretical and experimental studies focused on two-dimensional (2D) colloidal systems. The most prominent example is the famous Kosterlitz-Thouless-Halperin-Nelson-Young (KTHNY) theory [1–3] which, to date, has been verified through several experiments using two-dimensional (2D) colloidal systems [4, 5]. The KTHNY theory is a general theory of ordering, metastability and phase transitions in 2D systems and is therefore relevant for atomic systems including electrons on liquid helium and adsorbates on solid substrates such as films. In addition, colloidal systems allowed observation of an intriguing effect termed light-induced freezing [6–11] where a light-induced substrate induces freezing of a liquid adsorbate.

Since 15 years, 2D experiments in colloidal physics are paralleled by three-dimensional (3D) experimental studies employing confocal microscopy which allows 3D imaging [12]. To date, a large variety of experiments has been performed including investigation of glasses and glass transitions [13–16], template directed crystallization [17], systems with tunable interactions [18] and hard-sphere systems [19]. The major challenge is the fabrication of so-called photonic crystals [20] which exhibit a photonic band gap. Photonic crystals therefore allow directed photon emission.

In this work, we both experimentally and theoretically studied structural and dynamical properties of condensed matter employing colloidal particles as model systems. The studies are presented and discussed in independent chapters. These are outlined in the following after having briefly summarized two introductory chapters which describe the basic physics, methods and techniques applied in our experiments.

Chapter 2 contains an introduction to charged colloidal suspensions which were used in our experiments. In particular, both the particle pair interaction and the basics of optical tweezers, i.e. the interaction of dielectric particles with strong light fields, are presented. With this, we describe in Chapter 3 how to create extended substrate potentials through the use of the optical-tweezer technique. In addition, we outline video microscopy which allows particle imaging and detection and we show how to achieve precise control of both the particle density and the pair interaction strength.

We both theoretically and experimentally explore in Chapter 4 how phonon band structures of 2D crystals are modified through substrate potentials. The theoretical model is based on the so-called harmonic approximation which models both the particle pair interaction and the particle-substrate interaction through springs. As a result, we observe the occurrence of band gaps and both shifting and deformation of bands. This is verified through our experiments using charged colloidal suspensions and light-induced substrates. Our results may help to gain insight on how to customize thermal properties of solid matter such as specific heat or heat conductivity both crucially depending on the phonon band structure. In addition, our results may bring forward a young field of research concerned about so-called phononic crystals. These exhibit a phononic band gap and consequently reflect sound with a frequency within the band gap. Phononic crystals are therefore also termed deaf materials.

In Chapter 5, we experimentally investigate the structural properties of a binary hard-sphere mixture of big and small colloidal particles using confocal microscopy. We first prepared a sample consisting of only big particles and then subsequently increased the fraction of small particles. For each mixture, we determined the radial pair correlation function. As a result, we observe a marked change of the oscillation in the pair correlation function (from a wavelength slightly larger than the big particle diameter to a wavelength slightly larger than the small particle diameter). This behavior is termed structural crossover and has been recently predicted by theoretical studies.

Moreover, we show that structural crossover is related to the size of networks consisting of only equally sized particles connected through nearest-neighbor bonds. This is supported by Monte-Carlo simulations performed at different ratios of the particle sizes and packing fractions. With our results, we intend to help understanding the complex behavior of systems in nature and technology which are mostly mixtures of differently sized particles.

Chapter 6 presents our experimental studies on single-particle diffusion in the presence of a quasicrystalline light-induced substrate. As a result, we find subdiffusive behavior characterized by an increase of the mean-square displacement in time according to a power law with, in contrast to normal free diffusion, the power smaller than unity. Our results suggest that subdiffusion is associated with a thermalization process; quasicrystalline substrates are non periodic and exhibit a characteristic distribution of potential well depths which a diffusing particle must explore to thermalize. In addition, we find that normal diffusion is recovered at large times when the particle has thermalized. Together with the numerical studies discussed in Chapter 6 as well, we intend to understand subdiffusion more deeply since it plays an important role in both physics (diffusion in glasses and narrow pores) and biology (diffusion in cells).

In Chapter 7, we investigate the pair interaction in colloidal suspensions confined between two glass plates. Although a purely repulsive pair interaction is expected, several groups have independently reported an anomalous so-called like-charge attraction. Our results demonstrate that like-charge attraction arises from overlapping particle images which cause erroneous distance measurements. In addition, we explain the role of confinement; under confined conditions, the repulsive pair interaction is highly screened which leads to overlapping particle images. We also discuss how to avoid or, at least, to correct for optical artifacts; one can use specific particles whose images do not overlap or employ a new particle-detection method which accounts for erroneous distance measurements.

Parts of this work have been published elsewhere:

1. J. Baumgartl. *Lichtinduzierte Phasenübergänge in kolloidalen Suspensionen*. Diploma thesis, Universität Konstanz, 2003.
2. J. Baumgartl and C. Bechinger. On the limits of digital video microscopy. *Europhys. Lett.*, 71:487, 2005.
3. J. Baumgartl, J. L. Arauz-Lara, and C. Bechinger. Like-charge attraction in confinement: myth or truth?. *Soft Matter*, 2:631, 2006.
4. H. H. von Grünberg and J. Baumgartl. Lattice dynamics of two-dimensional colloidal crystals subject to external light potentials. *Phys. Rev. E*, 75(5):051406, 2007.
5. J. Baumgartl, R. P. A. Dullens, M. Dijkstra, R. Roth, and C. Bechinger. Experimental observation of structural crossover in binary mixtures of colloidal hard spheres. *Phys. Rev. Lett.*, 98(19):198303, 2007.

2

Colloids as model systems

ABSTRACT

This chapter first provides the definition of colloids. Then, colloids are motivated as model systems and colloidal physics is characterized. Finally, a more detailed discussion is given on both the pair interaction between colloidal particles and on the interaction of colloidal particles with external light fields.

2.1. DEFINITION OF COLLOIDS

Colloids refer to small particles which have typical sizes between $10nm$ and $10\mu m$ and which are dispersed in another material. The dispersed particles are large enough to describe the solvent as a continuous and homogeneous background yet they are small enough to display Brownian motion.

The definition of colloids does not depend on the state of aggregation of either the dispersed particles or the solvent. Both, colloidal emulsions (droplets in a liquid) and suspensions (solid particles in a liquid) constitute a colloid. Milk and gloss paint are typical examples for colloids, the former an emulsion and the latter a suspension.

The colloidal suspensions used in this thesis are composed of synthetic particles dispersed in water. The particles have an electrical charge leading to an electrostatic pair interaction between the particles. Besides charged particles, neutral and paramagnetic particles are also commonly used. These interact via hard-core and magnetic dipole-dipole interaction, respectively.

It is typical in colloidal physics to use imprecise terminology, referring to the dispersed particles themselves as colloids. In the following we will follow this convention.

2.2. COLLOIDS AS MODEL SYSTEMS FOR ATOMIC SYSTEMS

Brownian motion arises from collisions between particles and solvent. As a result, the kinetic energy E_{kin} of the colloids is closely tied to the kinetic energy of the solvent particles, i.e., the kinetic energy of the colloids obeys the Boltzmann distribution,

$$p(E_{kin}) \propto \exp\left(-\frac{E_{kin}}{k_B T}\right) \quad (2.1)$$

with $k_B = 1.38 \cdot 10^{-23} J/K$ the Boltzmann constant and T the temperature in units of K . If the colloids are subjected to an external potential, the potential energy also conforms to the Boltzmann distribution according to the Virial theorem,

$$p(E_{pot}) \propto \exp\left(-\frac{E_{pot}}{k_B T}\right) \quad \text{or} \quad p(\mathbf{r}) \propto \exp\left(-\frac{E_{pot}(\mathbf{r})}{k_B T}\right). \quad (2.2)$$

The second equation points out that the distribution of the potential energy yields the distribution of the colloid's position \mathbf{r} .

The kinetic and the potential energy of atomic particles are distributed according to (2.1) and (2.2) provided that quantum fluctuations can be neglected, a valid assumption if the temperature is sufficiently large and thermal fluctuations outweigh the quantum fluctuations. Due to the thermodynamic analogy, it is then possible to perform studies related to atomic systems through the use of colloidal systems. For instance, colloidal systems provide insight on topics related to the phase behavior of atoms in a monolayer or electrons on helium. Of course, it is also possible to directly investigate atoms e.g. by means of atomic force or scanning tunneling microscopy. However, colloidal

systems are non-invasive, simpler and more flexible. They can be investigated through a larger variety of experiments and allow resolution of particle dynamics. In addition, colloidal pair interactions and the interaction of colloids with external potentials can be customized allowing one to address a large variety of basic physical questions related to statistical mechanics.

2.3. CHARACTERIZATION OF COLLOIDAL PHYSICS

This section provides an overall motivation for colloidal physics. Subsequently, the pair interaction of colloidal particles and the interaction of colloidal particles with external light-fields will be discussed in more detail.

First of all, colloidal particles can be observed under an optical microscope due to their mesoscopic size. It is even possible to investigate the dynamics of colloids by means of a microscope. This can be demonstrated by considering the so-called self-diffusion time τ_s derived from the mean-square displacement

$$\langle \mathbf{r}^2(\tau) \rangle = 6D\tau \quad (2.3)$$

by inserting the particle diameter σ squared for the mean-square displacement,

$$\tau_s = \frac{\sigma^2}{6D}. \quad (2.4)$$

D is the diffusion constant given by the Stokes-Einstein relation

$$D = \frac{k_B T}{6\pi\eta\sigma}. \quad (2.5)$$

η denotes the viscosity of the solvent, in which the colloids are dispersed. To provide an estimate for τ_s , the parameters are set to $\sigma \approx 1\mu m$, $T \approx 300K$ and $\eta = 0.8mPa \cdot s$ (viscosity of water) which yields $\tau_s \approx 1s$. As a consequence, the dynamics of a colloidal system can be time resolved through means of video microscopy, a technique using a microscope, a charge-coupled device camera and particle detection software to record particle trajectories. Due to the relatively large self-diffusion time, it is even possible to investigate the kinetics of crystallization. In contrast, atomic systems do not allow for such studies because their self-diffusion time $\tau \approx 1ps$ is too short for time-resolved experiments with atomic resolution.

A major advantage of colloidal physics are customizable pair interactions; there are plenty of interaction types and the interaction strength can be mostly varied continuously. For instance, colloids can interact via a screened Coulomb potential, a dipole-dipole potential or a hard-core potential. In the case of the electrostatic interaction, the

strength can be varied with the salt concentration. Magnetic interactions can be modified with an external magnetic field which induces magnetic dipoles within the paramagnetic colloids, with a strength proportional to the external magnetic field. Both interactions are short-ranged. The electrostatic interaction is Yukawa-like, $\propto \exp(-r/r_0)$ (r_0 =screening length), while the magnetic interaction decays algebraically, $\propto r^{-3}$.

Adjustment of interactions is not restricted to pair interactions; it also applies to the interaction of colloids with external potentials. Colloids can be externally influenced by a large variety of potentials including electric or magnetic fields provided that the colloids are electrically charged or magnetic, respectively. Next, colloids can be subject to external potentials created by topographic patterns [17]. Finally, dielectric colloids can interact with strong external light fields. These can be generated by a single laser beam or by extended light intensity patterns, the latter created via static or dynamic methods. In general, it is possible to realize a huge variety of potential shapes such as one-dimensional periodic potentials induced by means of topographic patterns or laser light [8, 9].

2.4. PAIR INTERACTION IN COLLOIDAL SYSTEMS

Before we discuss the electrostatic interaction, it must be mentioned that colloids in general interact via attractive van-der-Waals forces because colloidal particles consist of dielectric and therefore polarizable materials. In the case of two spherical particles an analytical expression can be given for the van-der-Waals potential [21],

$$V_{vdW}(r) = -\frac{A}{6} \left[\frac{2a^2}{r^2 - 4a^2} + \frac{2a^2}{r^2} + \ln \left(1 + \frac{4a^2}{r^2} \right) \right] \quad (2.6)$$

with $a = \sigma/2$ the radius and r the center-to-center distance of the particles. For instance, the Hamaker constant is $A = 1.4 \cdot 10^{-20} J$ for polystyrene in water [22]. The van-der-Waals interaction is strongly attractive and therefore causes the colloidal particles to irreversibly stick together which is termed coagulation. In our experiments we typically use colloids of radius $a \approx 1\mu m$. These colloids coagulate if they come closer than approximately $100nm$. As a consequence, it is necessary to stabilize colloidal suspensions by means of a repulsive interaction. We now describe how the repulsive pair interaction arises in charged colloidal suspensions.

The surface of colloids is covered by sulfate molecules which are electrically neutral. When a colloid is dispersed in water, the positively charged counter ions of the sulfate ions are dissolved because the gain of energy is approximately $100k_B T$ per ion due to water molecule polarization. As a consequence, the surface of the colloids is negatively charged. The entropy tends to spread the ions homogeneously over the entire available phase space volume. Despite the electric attraction, the ions do therefore not condense back onto the surface. At equilibrium, the interplay between energy and entropy creates

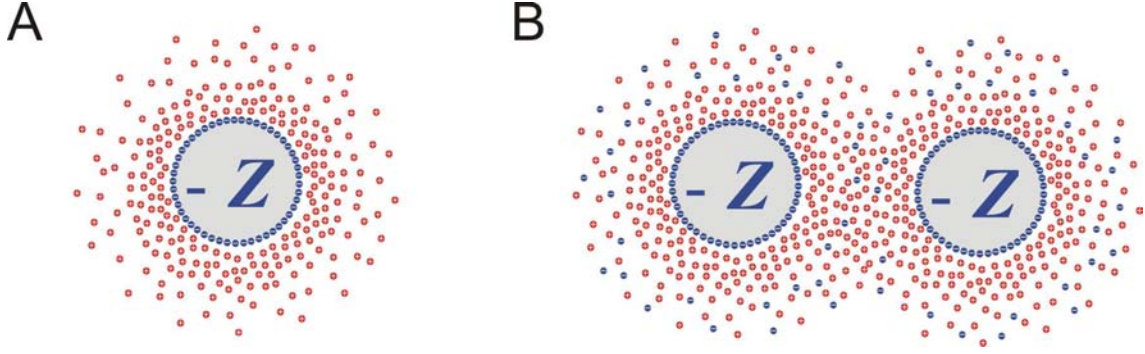


FIGURE 2.1. A) Non-scaled illustration of the electric double layer. It consists of the negative surface charge of the colloid and the positively charged ionic cloud around the colloid. Z denotes the surface charge in units of the elementary charge $e = 1.6 \cdot 10^{-19}C$. B) Schematic of the repulsive pair interaction which results from the overlap of the charge clouds. The blue spots in the outer range of the charge clouds represent negatively charged salt ions diluted in the water. Those ions screen the ion clouds around the colloids and thus lower the interaction strength.

the so-called electric double layer consisting of the negatively charged surface of the colloids and the positively charged spherical cloud of counter ions around the colloids. Figure 2.1A illustrates such a double layer.

The Poisson-Boltzmann equation describes the electric potential around a colloidal particle,

$$\epsilon_0 \epsilon_W \Delta \Phi = -e \sum_i z_i c_{i0} \exp\left(-\frac{z_i e \Phi}{k_B T}\right) \quad (2.7)$$

with $\epsilon_0 = 8.85 \cdot 10^{-12} As/Vm$ the vacuum permittivity, $\epsilon_W = 81$ the permittivity of water, $e = 1.6 \cdot 10^{-19}C$ the elementary charge, z_i the valency of the ion type i and c_{i0} the bulk concentration of the ion type i . The negative surface charge is taken into account through boundary conditions. It will be discussed later why not only the counter ions but several ion types appear in (2.7). The Poisson-Boltzmann equation can be viewed as the well-known Poisson equation with the charge density ρ proportional to the Boltzmann distribution of ions in a potential Φ . Linearization of the Poisson-Boltzmann equation yields an approximate solution which is valid for small potentials, i.e. $e\Phi \ll k_B T$,

$$\Phi(r) = \frac{Ze}{4\pi\epsilon_0\epsilon_W} \frac{\exp(\kappa\sigma/2) \exp(-\kappa r)}{1 + \kappa\sigma/2} \frac{1}{r} \quad (2.8)$$

with r the distance from the center of the colloidal particle. The potential (2.8) constitutes the well known Debye-Hückel potential. Note that the finite geometry of the colloid is taken into account by the second factor which matches unity for point-like

particles ($a = 0$). The inverse screening length κ is

$$\kappa = \sqrt{\frac{\epsilon_0 \epsilon_W k_B T}{\sum_i (e z_i^2) c_{i0}}}. \quad (2.9)$$

The pair interaction between colloids is obtained by linearly superimposing (2.8) yielding

$$u(r) = \frac{(Ze)^2}{4\pi\epsilon_0\epsilon_W} \left(\frac{\exp(k\sigma/2)}{1 + \kappa\sigma/2} \right)^2 \frac{\exp(-\kappa r)}{r} \quad (2.10)$$

with r now the center-to-center distance between colloidal particles. The pair interaction is proportional to the number of surface charges Z squared and is decreased by a factor of ϵ_W^{-1} due to the polarization of the water molecules. The last factor reflects the fast decay of the pair interaction with respect to the distance r originating from screening effects as follows: according to (2.9), the screening length is diminished by all ions present in the solvent. It is already known that the cloud of positive counter ions screens the negative surface charge of the colloids which will be screened even stronger in the presence of further positively charged ions. Also, if the solvent contains negative ions the clouds of counter ions will be themselves screened as sketched in Figure 2.1B.

The pair interaction $u(\mathbf{r})$ is not directly accessible in experiments but can be extracted from the directly accessible pair distribution function $g(\mathbf{r})$. In general, the pair distribution function is defined as

$$g(\mathbf{r}_1, \mathbf{r}_2) = \frac{\rho^{(2)}(\mathbf{r}_1, \mathbf{r}_2)}{\rho^{(1)}(\mathbf{r}_1)\rho^{(1)}(\mathbf{r}_2)} \quad (2.11)$$

with $\rho^{(n)}(\mathbf{r}_1, \dots, \mathbf{r}_n)$ the n -particle density. Moreover, $g(\mathbf{r}_1, \mathbf{r}_2)$ is related to the pair correlation function $h(\mathbf{r}_1, \mathbf{r}_2)$ via

$$h(\mathbf{r}_1, \mathbf{r}_2) = g(\mathbf{r}_1, \mathbf{r}_2) - 1. \quad (2.12)$$

$h(\mathbf{r}_1, \mathbf{r}_2)$ can be interpreted as the probability of finding a pair of colloids at the positions \mathbf{r}_1 and \mathbf{r}_2 . In the case of homogeneous and isotropic systems, the pair distribution function and the pair correlation function simplify to the radial distribution and the radial correlation function,

$$h(r) = g(r) - 1, \quad r = |\mathbf{r}_1 - \mathbf{r}_2|. \quad (2.13)$$

The pair interaction is obtained by inverting the Ornstein-Zernike equation,

$$h(\mathbf{r}_1, \mathbf{r}_2) = c(\mathbf{r}_1, \mathbf{r}_2) + \int d\mathbf{r}_3 \rho(\mathbf{r}_3) c(\mathbf{r}_1, \mathbf{r}_3) h(\mathbf{r}_3, \mathbf{r}_2) \quad (2.14)$$

with $c(\mathbf{r}_1, \mathbf{r}_2)$ the direct correlation function. Intuitively, the Ornstein-Zernike equation can be interpreted as follows: the correlation between two particles arises from a direct contribution and the correlations mediated by all possible third particles at positions

\mathbf{r}_3 . In the case of homogeneous and isotropic systems, the Ornstein-Zernike equation is written as

$$h(r) = c(r) + \rho \int d\mathbf{r}' c(|\mathbf{r} - \mathbf{r}'|) h(r'). \quad (2.15)$$

If $c(r)$ is known, (2.15) constitutes a closed integral equation for $h(r)$. $c(r)$ is, however, not known in general, and an additional closure relation is therefore required to solve (2.15). Such a closure relation can be constructed on the basis of the limiting cases which are known,

$$\lim_{\rho \rightarrow 0} c(r) = \exp\left(-\frac{u(r)}{k_B T}\right) \quad \text{and} \quad \lim_{r \rightarrow \infty} c(r) = -\frac{u(r)}{k_B T}. \quad (2.16)$$

Two closure relations have turned out to be particularly suitable for describing the structure of systems with short- and long-range interactions, namely the Percus-Yevick (PY) and the hypernetted chain (HNC) equations,

$$c(r) = g(r) \left[1 - \exp\left(\frac{u(r)}{k_B T}\right) \right] \quad (\text{PY}) \quad (2.17)$$

$$c(r) = g(r) - 1 - \frac{u(r)}{k_B T} - \ln g(r) \quad (\text{HNC}). \quad (2.18)$$

For a more detailed description, see [23] and [24] and the references therein¹.

2.5. INTERACTION OF COLLOIDAL PARTICLES WITH STRONG EXTERNAL LIGHT-FIELDS

In the following, we provide an introduction to the basic interactions between colloidal particles and external substrate potentials generated by laser light [25–28]. First, we explain the origin of the gradient force and then turn to the radiation pressure. The two forces are illustrated in Figure 2.2.

An intuitive explanation of the gradient force can be summarized as follows: colloidal particles are dielectric and therefore experience a force in an inhomogeneous light field towards the maximum intensity value. However, this requires that

$$\epsilon_K(\lambda) > \epsilon_W(\lambda) \quad (2.19)$$

with $\epsilon_K(\lambda)$ and $\epsilon_W(\lambda)$ the dielectric constants of the colloidal particles and water, respectively, and λ the wavelength of the light. To prove (2.19), let E_K and E_W denote the electric field strengths which are induced by a light beam in a colloidal particle and water. According to [29], those two field strengths are related to each other via

$$E_K = \frac{3\epsilon_W(\lambda)}{\epsilon_K(\lambda) + 2\epsilon_W(\lambda)} E_W. \quad (2.20)$$

¹The brief summary that has been given here is based on sections 2.3.1 and 2.3.2 in [23].

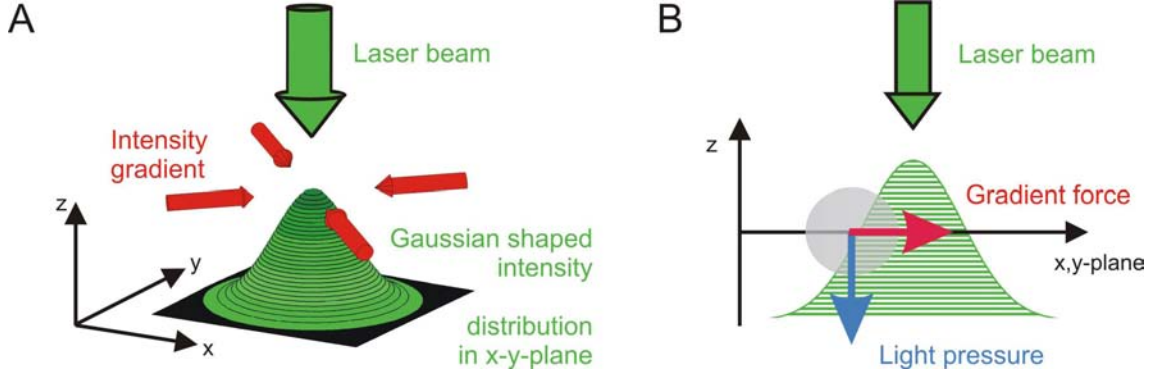


FIGURE 2.2. A) Gaussian-shaped intensity profile in x - y -plane created by a laser beam which propagates in the z -direction. As indicated by the red arrows, the intensity gradient radially points to the center of the beam where the intensity is the greatest. B) Cross section of the intensity profile. The colloidal particle is sketched as a grey sphere. The two forces acting on the particle are indicated by the blue (light pressure) and the red arrows (gradient force).

If $\epsilon_K(\lambda) \neq \epsilon_W(\lambda)$, the colloidal particle appears as a dipole,

$$d = (\epsilon_K(\lambda) - \epsilon_W(\lambda))V_K E_K \quad (2.21)$$

with $V_K = 4/3\pi r_K^3$ the volume and r_K the radius of the colloidal particle. Since the dipole moment interacts with the light electric field, the interaction energy becomes

$$U_{grad} = -\frac{1}{2}d \cdot E_K = -2\pi\epsilon_W\epsilon_K r_K^3 \left(\frac{\epsilon_K(\lambda) - \epsilon_W(\lambda)}{\epsilon_K(\lambda) + 2\epsilon_W(\lambda)} \right) E_W^2. \quad (2.22)$$

To trap the colloidal particle in the center of a laser beam, $U_{grad} < 0$ is required, a condition fulfilled if (2.19) is valid.

The polystyrene and silica particles used in our experiments satisfy the condition (2.19) for a wide range of wavelengths λ , in particular for the laser wavelengths $\lambda = 488nm$, $\lambda = 514nm$ and $\lambda = 532nm$ which we performed our studies with.

The light pressure of a laser beam exerts a second force on a colloidal particle; because of scattering, momentum is transferred from the laser beam to the particle. According to [30], the momentum density of an electromagnetic wave is given by

$$\mathbf{g} = \frac{\mathbf{S}}{c^2} = \epsilon_0(\mathbf{E} \times \mathbf{B}) \quad (2.23)$$

with \mathbf{S} the Poynting vector and \mathbf{B} the magnetic field. The momentum transferred to the colloidal particle points in the direction of \mathbf{g} provided that the laser beam acts on the particle symmetrically. The light pressure is then given by the momentum transferred per unit area and time,

$$p = c|\mathbf{g}| = c\epsilon_0\epsilon_W(\lambda)E_0B_0 = \frac{\epsilon_W(\lambda)}{c}I_{scat}. \quad (2.24)$$

Here, E_0 and B_0 denote the amplitudes of the electric and the magnetic field and I_{scat} refers to the intensity scattered at the surface of the colloidal particle. In the case of a small sphere in an oscillating electromagnetic field, the scattering is mostly caused by dipole scattering. According to Rayleigh, an analytical expression can be derived [31],

$$I_{scat} = \frac{8\pi}{3} \frac{\sigma^6}{\lambda^4} \left(\frac{\epsilon_K(\lambda) - \epsilon_W(\lambda)}{\epsilon_K(\lambda) + 2\epsilon_W(\lambda)} \right) I_{Laser} \quad (2.25)$$

with σ the diameter of the sphere and I_{Laser} the intensity of the incident laser beam. The light pressure is then obtained by dividing the scattered intensity by the speed of light in water $c/\epsilon_W(\lambda)$,

$$p_{scat} = \frac{8\pi}{3c} \frac{\sigma^6}{\lambda^4} \epsilon_W(\lambda) \left(\frac{\epsilon_K(\lambda) - \epsilon_W(\lambda)}{\epsilon_K(\lambda) + 2\epsilon_W(\lambda)} \right) I_{Laser}. \quad (2.26)$$

In our experiments, we make use of light pressure to push colloidal particles towards a glass plate and thus to prepare colloidal systems confined to 2D.

3

Experimental setup

ABSTRACT

In this chapter, we provide a general description and discussion of the experimental setup used in our studies. First, it is shown how to generate a one-dimensional (1D) periodic substrate potential through the use of two overlapping laser beams. In addition, the realization of more complex potential patterns is discussed briefly. Second, we focus on the video microscopical setup and particle detection. The third part of this chapter is dedicated to the preparation of colloidal systems confined to 2D and on the technique allowing adjustment of the particle density. We finally show how the strength of the colloidal pair interaction can be manipulated.

3.1. CREATION OF 1D PERIODIC POTENTIALS

3.1.1. Basics

A 1D periodic light potential is created through the use of two overlapping expanded laser beams having the same intensity (see Figure 3.1A). Figure 3.1B shows an intensity cross section along the x -axis to visualize the intensity distribution in the x - y -plane. The wave vectors \mathbf{K}_1 and \mathbf{K}_2 have the same modulus, i.e. $|\mathbf{K}_1| = |\mathbf{K}_2| = 2\pi/\lambda$, and the same angle φ in the x -direction with respect to the x - y -plane. λ denotes the wavelength of the laser light. The wave vectors projected to the x - y -plane are

$$\begin{aligned} K_{1,x} &= |\mathbf{K}_1| \cos \varphi = \frac{2\pi}{\lambda} \sin\left(\frac{\theta}{2}\right), \\ K_{2,x} &= -K_{1,x} = -\frac{2\pi}{\lambda} \sin\left(\frac{\theta}{2}\right). \end{aligned} \quad (3.1)$$

Describing the two laser beams as planar waves in the x -direction, i.e. $E_1(x) = A \exp(iK_{1,x}x)$ and $E_2(x) = A \exp(iK_{2,x}x)$, the total amplitude can be written as

$$E(x) = E_1(x) + E_2(x) = 2A \cos(K_{1,x}x). \quad (3.2)$$

According to (2.22), the gradient potential U_{grad} is proportional to E^2 and the 1D periodic potential U_{el} therefore becomes

$$U_{el} = -U_0 \left[1 + \cos(2K_{1,x}x) \right] = -U_0 \left[1 + \cos\left(\frac{2\pi}{d}x\right) \right] \quad (3.3)$$

with d the period of the potential,

$$d = \frac{\pi}{K_{1,x}} = \frac{\lambda}{2 \cos \varphi} = \frac{\lambda}{2 \sin(\theta/2)}. \quad (3.4)$$

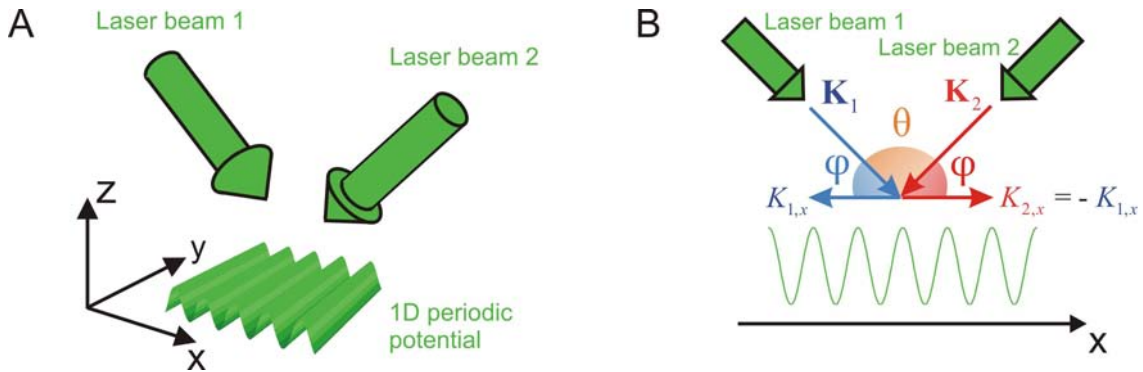


FIGURE 3.1. 1D periodic light potential created with two interfering laser beams. A) three-dimensional illustration. B) Cross section along the x -axis. \mathbf{K}_α and $K_{\alpha,x}$ ($\alpha = 1, 2$) are the laser beam wave vectors and the projections into the x - y -plane, respectively. φ denotes the incidental angle and θ the angle between the two beams.

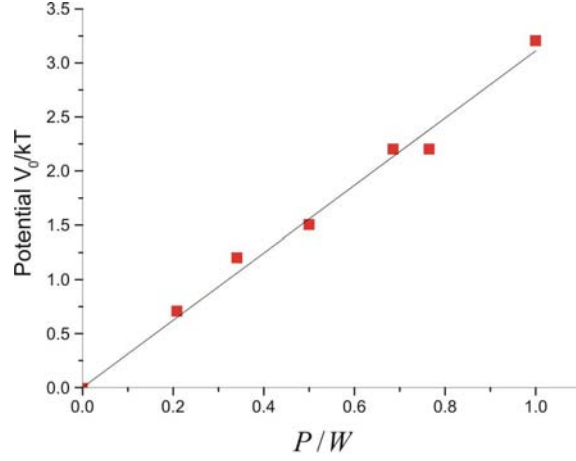


FIGURE 3.2. Potential strength U_0 versus laser power P [10,33]. The symbols represent experimental data obtained as described in section 3.1.3. The solid line is a linear fit to the data.

θ denotes the angle between the two laser beams. Loudiyi et al. [32] have evaluated the potential strength U_0 through integration over the spherical particle volume,

$$U_0 = \underbrace{2\epsilon_W(\lambda)\sigma^3}_{=:A} \left(\frac{\epsilon_K(\lambda) - \epsilon_W(\lambda)}{\epsilon_K(\lambda) + 2\epsilon_W(\lambda)} \right) \underbrace{\frac{4P}{cr_0^2}}_{=:B} \underbrace{\frac{j_1(\pi\sigma/d)}{2\pi\sigma/d}}_{=:C}. \quad (3.5)$$

The factor A is known from the gradient potential (2.22). The factor B depends on the laser power P and on the beam radius r_0 in the x - y -plane. $c = 3 \cdot 10^8 \text{ m/s}$ denotes the speed of light. The factor C incorporates the finite particle size with j_1 the first order spherical Bessel function. Since $C \rightarrow 0$ for $\sigma \rightarrow \infty$, large colloids less feel light potentials than small ones. The linear dependence of U_0 on the laser power P has been verified experimentally in [10,33] (see Figure 3.2).

The angle θ can be varied with a lens and depends on the distance s between the two beams in front of the lens (see Figure 3.3). An exact relation between θ and s can be

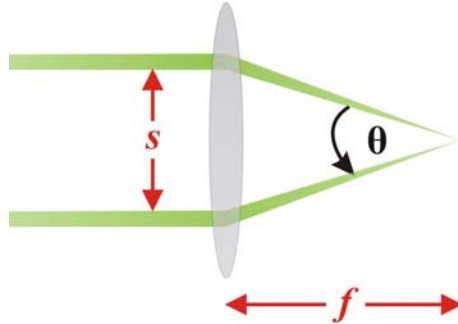


FIGURE 3.3. Variation of the angle θ between the two green laser beams. In front of the gray lens, the distance s between the two beams can be increased (decreased) leading to an increase (decrease) of θ .

provided,

$$\tan\left(\frac{\theta}{2}\right) = \frac{s}{2f} \quad (3.6)$$

with f the focal length of the lens. In our setup, the parameters are typically chosen as $f = 10\text{cm}$ and $s \approx 1\text{cm}$ and the angle accordingly is $\theta \approx 5^\circ$. Hence, we can set $\tan(\theta/2) \approx \sin(\theta/2)$ and (3.6) simplifies to

$$d \approx \lambda \frac{f}{s}. \quad (3.7)$$

Both this expression and $U_0 \propto P$ demonstrate the flexibility of 1D periodic light potentials because the periodicity (via s) and the potential strength (via P) can be varied continuously over a wide range. Our setup allows variation of periodicity between $2\mu\text{m}$ and $6\mu\text{m}$ and of potential strength between 0 and $20k_B T$ (see Section 3.1.3).

3.1.2. Optical setup

In our experiments, we use a Nd:YVO₄-solid state laser (Coherent Verdi V5) emitting monochromatic light with a wavelength of $\lambda = 532\text{nm}$ and a power between 0 and 5.5W . The optical setup generating the light potential is shown in Figure 3.4. First, the beam expander consisting of lens 1 and lens 2 expands the laser beam by a factor of two. A 50:50-beam splitter then splits the beam into two beams having the same intensity. The prisms 1 and 2 and mirror 1 finally deflect the two beams and make them propagating parallel to the x -axis. The prisms are mounted on translation stages and can be therefore displaced continuously in the y -direction. This allows variation of the distance s between the two beams. Figure 3.5 shows the part of the setup which is located in the red cube in Figure 3.4. The two beams are superimposed by lens 3 and deflected towards the sample cell by mirror 2. Note that the sum of the two

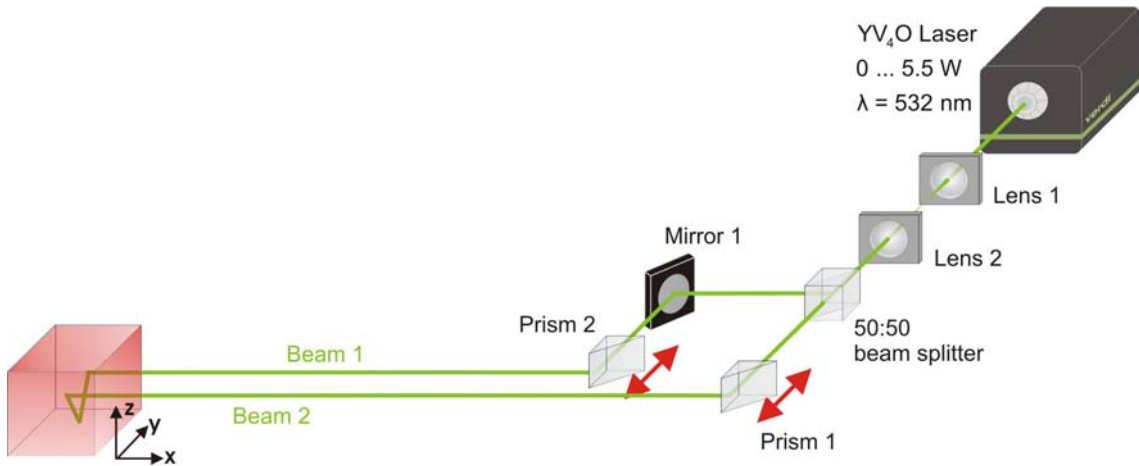


FIGURE 3.4. Optical setup creating a 1D periodic light potential. The setup within the red cube is shown in Figure 3.5. The red arrows indicate that the prisms can be displaced continuously in the y -direction.

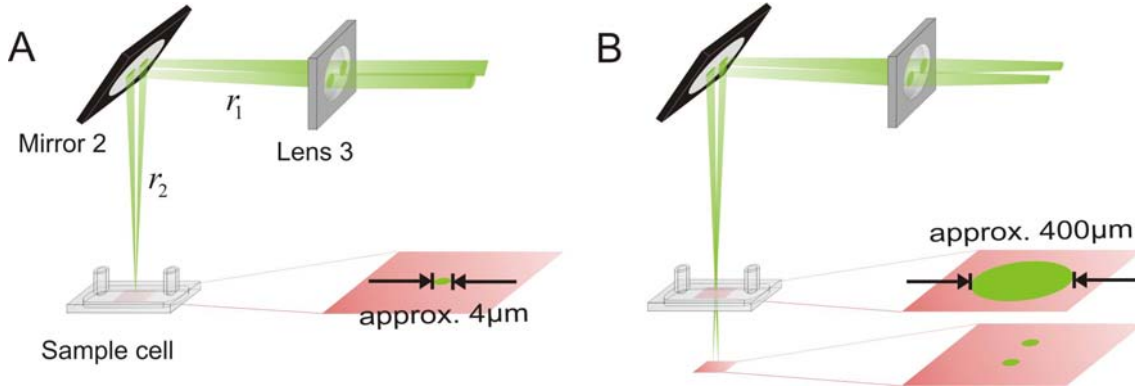


FIGURE 3.5. Creation of an expanded light potential in the sample cell. The two laser beams are superimposed by lens 3 and deflected towards the sample cell by mirror 2. The sum of the two distances r_1 and r_2 equals the focal length of lens 3. A) The two laser beams are collimated light bundles and are therefore focussed into the sample plane. In this, the lateral extension of the created light potential is limited to about $4\mu m$. B) The two laser beams are divergent light bundles and the beams are therefore focussed below the sample. Here, the light potential laterally extends up to $400\mu m$.

distances r_1 (between lens 3 and mirror 2) and r_2 (between mirror 2 and the sample cell) equals the focal length of lens 3 (see Figure 3.5A). Accordingly, the two laser beams are focussed into the sample cell if collimated in front of lens 3; for this, the distance between lens 1 and lens 2 (see Figure 3.4) must match the sum of the respective focal lengths. The foci have a typical size of approximately $4\mu m$ and therefore, no laterally extended light potential can be created. However, the small foci can be observed online with video microscopy and can be therefore overlapped with a high spatial accuracy. To increase the lateral extension, the distance between lens 1 and lens 2 is increased by a few millimeters. The two beams then still propagate parallel to the x -direction but are not collimated anymore; the beams are convergent behind lens 2, focussed close to the prisms and are finally divergent light bundles focussed below the sample cell (see Figure 3.5B). Since the beams are still overlapping in the sample plane, the lateral extension of the light potential is increased up to $400\mu m$ depending on the distance between lens 1 and lens 2.

3.1.3. Calibration of the substrate potential

In principle, the potential strength U_0 can be calculated according to (3.5). The laser power P is rather easily and accurately accessible using a power meter (Coherent field master, for instance), and the lateral extension r_0 of the laser beams can be estimated from intensity cross-sections measured with video microscopy. However, an accurate determination of U_0 requires the calibration measurement described in the following.

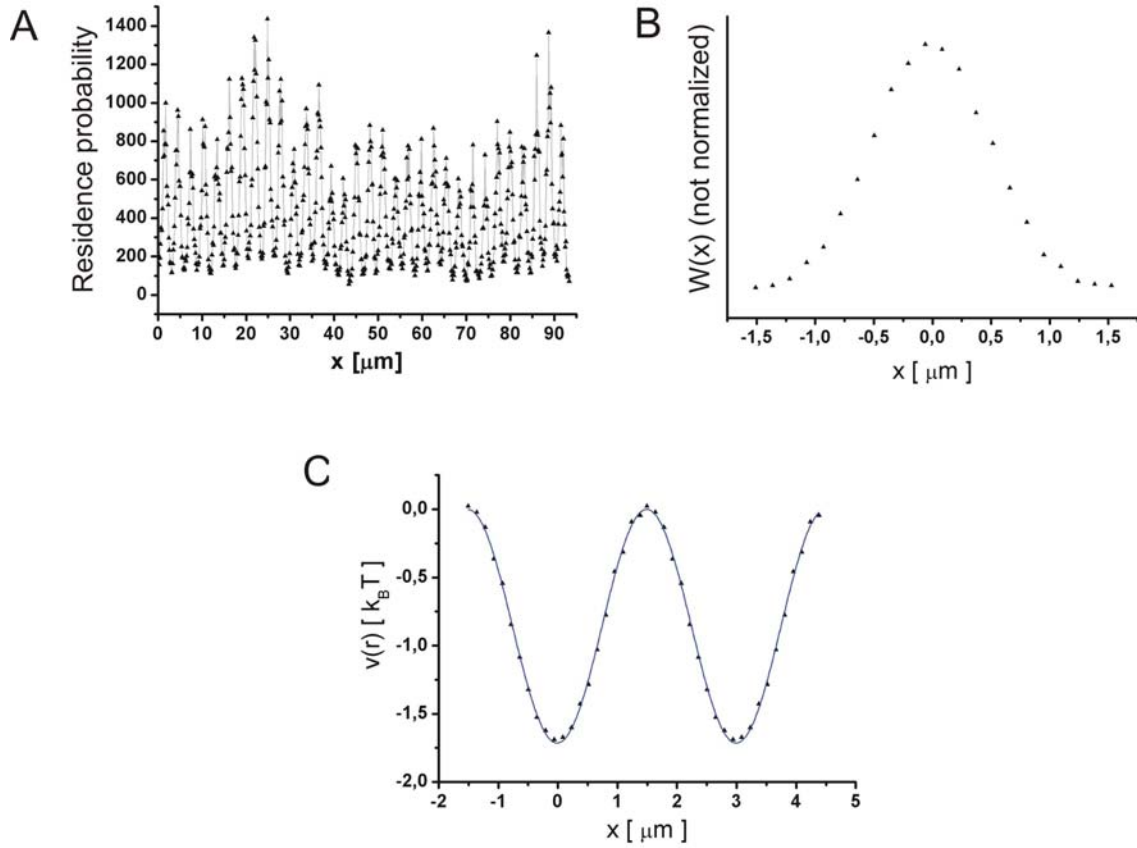


FIGURE 3.6. Calibration of a 1D periodic light potential. A) Residence histogram of a dilute system of colloids perpendicular to the potential troughs. B) Residence probability with respect to a single trough $w(x)$ determined from the histogram shown in Figure A. C) Potential $U(x)$ determined by inverting the Boltzmann factor. The black triangles represent the experimental data and the blue line corresponds to a fit according to (3.3).

First, we measure the residence histogram of a dilute colloidal system perpendicularly to the potential troughs, i.e. in the x -direction. Figure 3.6A shows such a measured histogram. The histogram is then cut into sections corresponding to single potential troughs. The sections are summed up yielding the periodicity d and the residence probability $w(x)$ with respect to a single potential trough (see Figure 3.6B). Next, we plot two troughs next to each other as shown in Figure 3.6C and invert the Boltzmann factor

$$w(x) \propto \exp\left(-\frac{U(x)}{k_B T}\right) \implies \frac{U(x)}{k_B T} \propto -\ln[w(x)]. \quad (3.8)$$

The resulting potential $U(x)$ is shown in Figure 3.6C. We finally determine the strength U_0 by fitting a curve to the experimental data according to (3.3).

3.1.4. Creation of more complex substrate potentials

To describe the creation of light potentials analytically, we introduce a coordinate system in the symmetry plane of lens 3 (see Figure 3.5) with the origin located at the center of lens 3. The basic vectors are denoted as \hat{e}_1 and \hat{e}_2 (see Figure 3.7A). Using this coordinate system, the two laser beams creating the 1D periodic light potential according to (3.3) are arranged at the positions

$$\mathbf{X}_1 = -\frac{s}{2}\hat{e}_1 \quad \text{and} \quad \mathbf{X}_2 = \frac{s}{2}\hat{e}_2. \quad (3.9)$$

In the following, we will use this formalism to describe the creation of more complex substrate potentials.

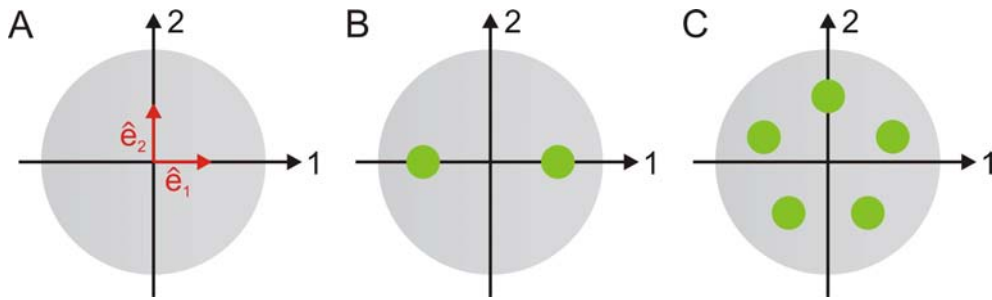


FIGURE 3.7. A) lens 3 (indicated by the filled gray circle) in the y - z -plane (see Figure 3.4 and 3.5). A new coordinate system with the origin at the center of lens 3 is introduced to describe the laser beam arrangement analytically. The basic vectors are denoted by \hat{e}_1 and \hat{e}_2 . B) Two-laser-beam arrangement to create a 1D periodic potential. C) Five-laser-beam arrangement to create a pentagonal quasicrystalline potential.

3.2. DIGITAL VIDEO MICROSCOPY

We now turn to the second important component of our experimental setup. First, we discuss the video microscopical setup and then focus on particle detection.

3.2.1. Video microscopical setup

To demonstrate the location of the video microscopical components in the total experimental setup, Figure 3.8 also shows the optical setup creating the 1D periodic light potential (see Figure 3.5). The two laser beams are indicated by the large green arrow. Colloids in the sample cell are illuminated with a cold light lamp and imaged onto the chip of a charge-coupled device (CCD) camera using an objective, a mirror and a tubus lens. In the case of high resolution measurements of pair interactions (see Chapter 7), we typically used objectives of magnification $63\times$ or $100\times$ and of numerical aperture 0.75 or 1.25, respectively. A large field of view is required for studies on many particle systems (Chapter 4); we therefore use objectives of magnification $20\times$ and numerical aperture 0.4. The green filter absorbs the laser light and therefore protects the CCD

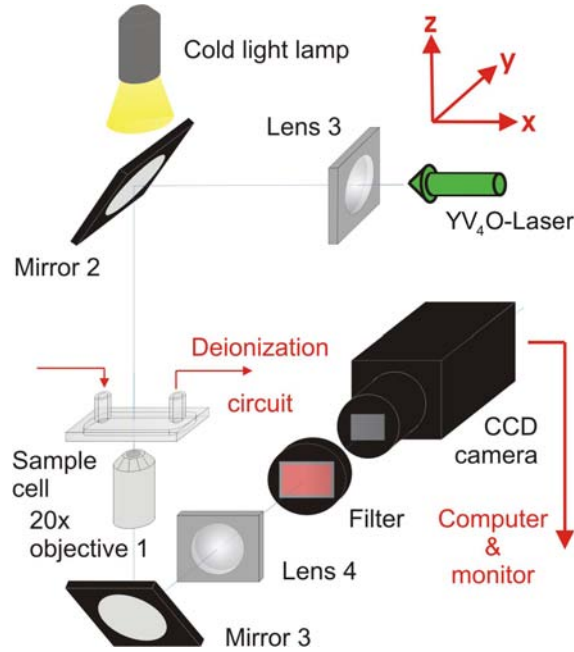


FIGURE 3.8. Video microscopical setup. To indicate the location of the video microscopical components in the total setup, the components displayed in Figure 3.5 are shown as well.

camera. To observe colloidal systems online, the CCD camera is connected to a monitor. Figure 3.9A and B display typical snapshots of a 2D system of approximately 1500 colloidal particles and of a 1D periodic light potential, respectively. Note that the green filter must be removed to observe light potentials. The red circle in Figure 3.9A indicates an additional 1D potential employed to prepare 2D colloidal systems of defined densities. This is discussed later in Section 3.4.

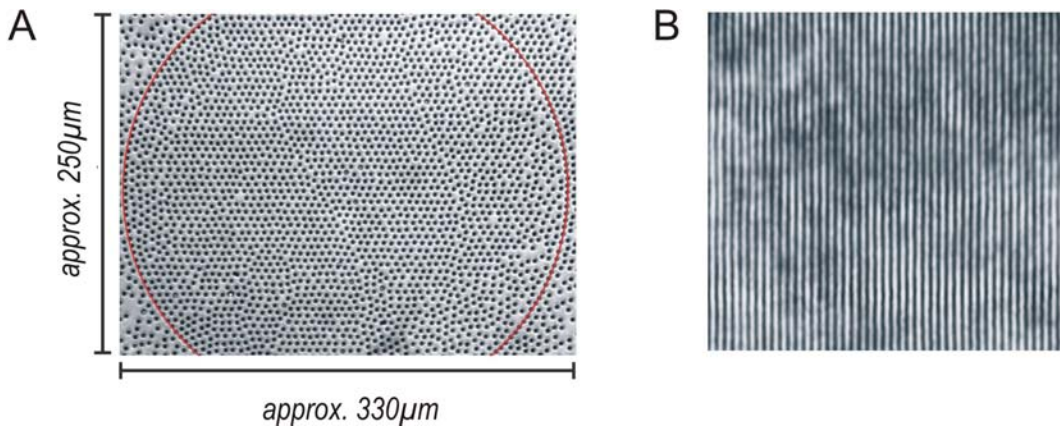


FIGURE 3.9. A) Typical snapshots of a system consisting of approximately 1500 colloidal particles. The red circle indicates a 1D potential which allows preparation of defined boundary conditions (see Section 3.4). B) Snapshot of a 1D periodic light potential created by means of two interfering laser beams.

The CCD camera is connected to a computer via a frame grabber card. We use an image processing software (Visiometrics IPS) detecting particle coordinates and saving them in a file. From the saved coordinates, we can evaluate a huge variety of physical quantities including particle densities, residence histograms, 2D or radial pair distribution functions, structure functions and mean square displacements.

3.2.2. Particle detection

We used a particle-detection algorithm developed by Nesper and Bubeck [34]. To provide a brief description, we consider a typical recorded video image as shown in Figure 3.10. If associated with particles, pixels are referred to as foreground pixels and as background pixels otherwise. Pixel intensities are considered to distinguish between foreground and background pixels. The intensity values are ideally spread over the whole available range (0 – 255) as demonstrated through the pixel intensity histogram shown in Figure 3.10B. The low values are associated with dark particles and the high values refer to the bright background. We set a threshold (vertical black line in Figure 3.10B) and therefore assign the low and high intensity values to foreground and background pixels, respectively. Figure 3.10C displays an intensity cross section of a two-particle image; it is clearly visible how the intensity drops in regions where particles are present. In addition, we can optionally select a so-called range of interest (see Figure 3.10D). Then, particles are only detected within the selected range of interest.

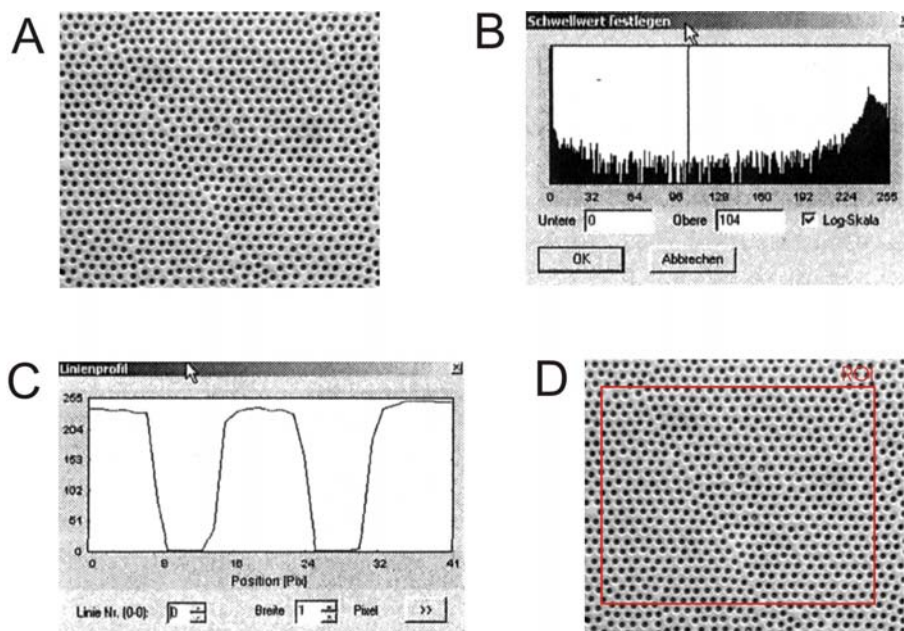


FIGURE 3.10. Essential steps of particle detection. A) Intrinsic video image. B) Histogram of intensity values which occur in the image and fixing of the threshold value (vertical solid line). C) Cross section of two particles' images. D) Selection of a range of interest (ROI = range of interest).

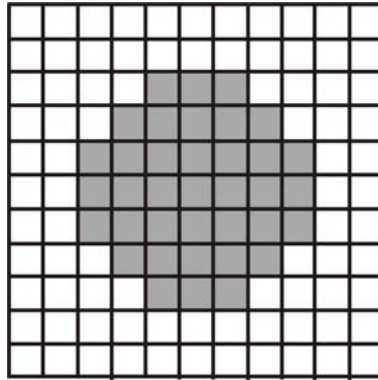


FIGURE 3.11. Measurement of particle coordinates. Pixels are colored in gray if associated with the particle image. The center of mass of the gray area yields the particle coordinate. Note that with this technique allows determination of particle coordinates with subpixel resolution.

Figure 3.11 provides a more detailed demonstration of particle detection. Pixels associated with particles, i.e. the foreground pixels, are colored in gray and the particle coordinate is determined by calculating the gray area's center of mass termed the intensity weighted centroid. The accuracy of this method depends on the number of foreground pixels associated with single-particle images. Since a single-particle image is typically covered by several tenths of foreground pixels, particle coordinates can be measured with subpixel resolution. Depending on the objective and the tubus lens, one pixel corresponds to a length between 50 and 400nm and the respective resolution is between 15 and 50nm.

To evaluate dynamical quantities such as diffusion constants, detailed information about the time evolution of particle motion is required [35]. Particle trajectories can be determined from particle coordinates if the time step dt between two subsequently recorded images is small compared to the average diffusive particle motion (see Section 2.3 and table I in [11]). Figure 3.12A shows the situation where dt is small enough to uniquely assign trajectories to coordinates. In contrast, dt is too large in Figure 3.12B and trajectories cannot be determined.



FIGURE 3.12. Temporal assignment of particle coordinates to particle trajectories. The open circles indicate particle positions at time t . One time step later ($t + dt$) the coordinates are represented by filled circles. A) Coordinates can be assigned to trajectories. B) Here, an unique assignment is impossible.

3.3. PREPARATION OF TWO-DIMENSIONAL SYSTEMS

We now focus on the boundary conditions of our measurements. It is shown how we confine colloidal systems to 2D and how we control the density.

In the absence of light potentials, two forces are exerted on colloidal particles in the sample cell. The particles sediment to the bottom plate of the cell due to gravity and are repelled by the bottom plate. The gravitational force is given by

$$F_G = \frac{4}{3}\pi\sigma^3g(\rho_K - \rho_W) \quad (3.10)$$

with ρ_K and ρ_W the respective densities of the colloids and water. For instance, the polystyrene colloids used in our experiments ($\rho_K = 1.05g/cm^3$, $\sigma = 2.4\mu m$) experience a force of approximately $F_G \approx 5fN$. The repulsive electrostatic particle-wall interaction arises from overlapping double layers as in the case of two colloidal particles (see Section 2.4). The Poisson-Boltzmann equation (2.7) for a particle in front of an infinitely extended wall can be solved approximatively in the framework of the Gouy-Chapman theory [36] yielding the analytical expression

$$\Phi(z) = 4 \ln \left(\frac{1 + \tanh(\Phi(0)/4) \exp(-\kappa z)}{1 - \tanh(\Phi(0)/4) \exp(-\kappa z)} \right), \quad \sinh \left(\frac{\Phi(0)}{2} \right) = \frac{\sigma_S}{2\kappa\epsilon_0\epsilon_W k_B T} \quad (3.11)$$

with σ_S the surface charge density of the bottom plate. Similar to the colloidal pair interaction (2.10) the inverse screening length κ grows with the concentration of salt and counter ions.

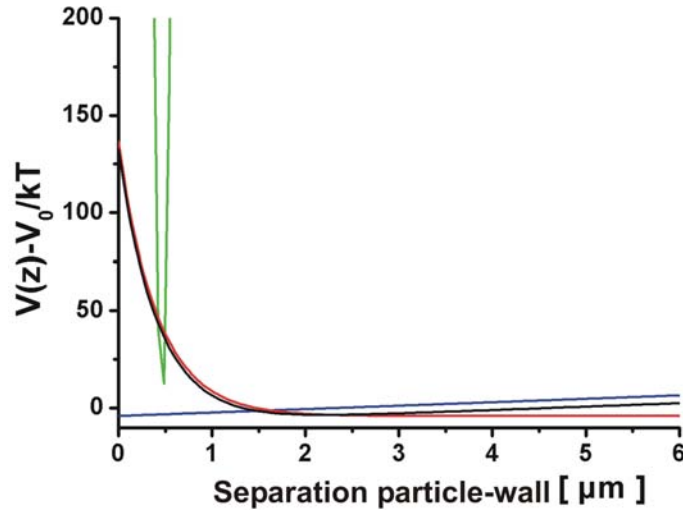


FIGURE 3.13. Potential of a colloidal particle perpendicular to the bottom plate of the sample cell. The red potential arises from the repulsive particle-wall interaction. The black potential additionally accounts for gravity which is represented by the blue curve. If the particle is pushed towards the wall by means of a laser beam the resulting potential is given by the green curve.

According to [37, 38] the average distance of colloidal particles from the bottom plate approximately is $2\mu m$ for a typical value of $\kappa \approx 2\mu m^{-1}$. The particles fluctuate around this average distance with an amplitude of approximately $\pm 1.5\mu m$ [38]. Colloidal systems are therefore not confined to 2D by gravity. To visualize this, we plotted the gravitational potential $F_G z$ and the electrostatic potential (3.11) as blue and red curves in Figure 3.13, respectively. The black curve represents the sum of the two potentials. For distances smaller than $1.5\mu m$ the electrostatic interaction dominates. In contrast, the gravitational potential exceeds the electrostatic interaction for distances larger than $2.5\mu m$.

The light pressure (2.26) exerted on a colloidal particle by a laser beam exceeds the gravitational force by a factor of approximately 15000. As a consequence, the particle fluctuations perpendicular to the bottom plate are tremendously reduced to a range of approximately $100nm$. This corresponds to approximately 3% of the particle diameter σ . The tremendous reduction of the fluctuations is reflected in the green potential (see Figure 3.13) which is the superposition of the repulsive electrostatic potential and the potentials arising from gravitation and light pressure. It is therefore possible to prepare 2D colloidal systems through the use of a laser beam pushing the colloidal particles towards the bottom plate of the sample cell.

Two-dimensional confinement of colloidal systems can also be achieved geometrically; for this, one uses two glass plates which have a distance slightly larger than the particle diameter σ [39–41]. As discussed below, this approach is suitable for colloidal systems where high densities or strong pair interactions are not required.

3.4. ADJUSTING THE DENSITY OF COLLOIDAL SYSTEMS

In numerical calculations, infinite systems can be studied using finite systems and periodic boundary conditions. In contrast, experimental systems are inevitably finite-sized. In principle, our sample cells allow preparation of large systems with a lateral extension of approximately $2cm^2$; however, the video microscopical setup and the available lateral extensions of light potentials restrict the system size to approximately $300 \times 200\mu m^2$.

To establish well-defined boundary conditions in our measurements we must isolate the colloidal system within the field of view; colloids must neither leave the system nor enter it from outside due to diffusive motion. We achieve this using a 1D boundary potential indicated in Figure 3.9 as red solid line.

We create 1D boundary potentials as follows: the light source is an argon-ion laser (Coherent Innova) operating in single-line mode ($\lambda = 488nm$). The emitted power can be varied continuously between 0 and $2.5W$. Figure 3.14 shows the optical setup which allows creation of 1D boundary potentials. To integrate this setup into the complete experimental setup, we also show the optical components creating the 1D periodic light

potential (see Figure 3.4). First, we clean the laser mode with a spatial filter consisting of lens 5, lens 6 and a pinhole in the focal plane. Next, the laser beam is deflected by two galvanostatically driven mirrors. A driving software allows creation of linearly, rectangularly or circularly shaped patterns with a scanning frequency of approximately 200Hz . Colloidal particles experience such scanned patterns as quasistatic light potentials due to the self diffusion time of approximately 1s . The lenses 7 and 9, the $20\times$ -objective 2 and a dichroitic mirror finally image the created light pattern into the sample plane (see Figure 3.15). The setup to create boundary potentials is termed scanned optical tweezers.

In addition, we incorporated a single focused laser beam into the scanned-tweezers setup. The single beam allows us to precisely address single colloidal particles. This is of particular advantage because colloidal suspensions are always contaminated with coagulated particles due to the attractive van-der-Waals interaction (2.6). The beam is coupled out with a microscope slide (see Figure 3.14) and is then transmitted through prism 3, mirror 5, mirror 6, lens 8 and the beam splitter into objective 2 (Figure 3.15). Similar to the scanned beam, objective 2 focuses and the dichroitic mirror deflects the single static beam into the sample plane. The setscrews of mirror 5 allow precise positioning of the single optical tweezers in the whole field of view.

The driving software of the galvanostatically driven mirrors provides a special feature which allows continuous variation of the boundary potential's size. Since colloids inside the boundary are confined by colloids trapped on the boundary potential, we can precisely adjust the density by varying the boundary potential's extension. If the extension grows the density becomes smaller and vice versa.

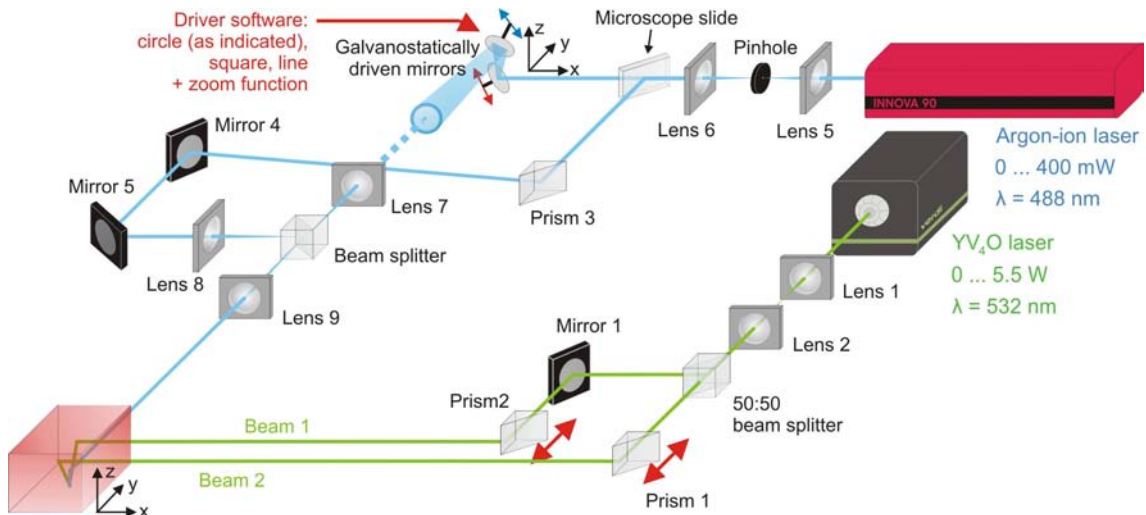


FIGURE 3.14. Scanned optical tweezers. To integrate the scanned optical tweezers into the complete setup the optical components which generate the interference pattern (see Figure 3.4) are shown as well.

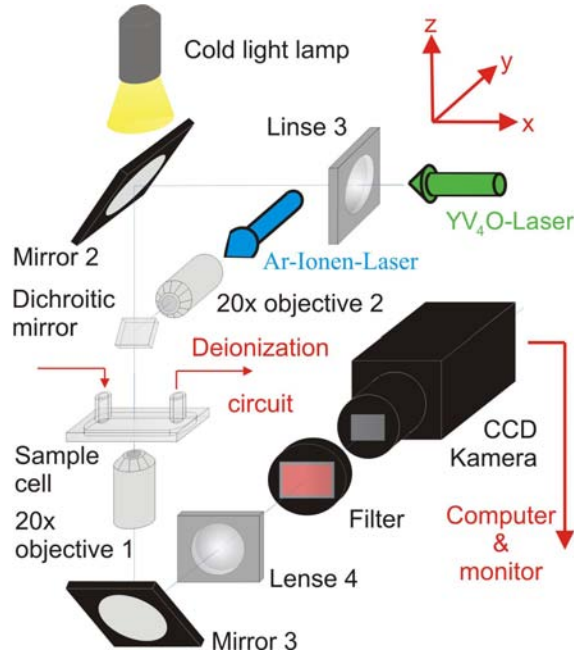


FIGURE 3.15. Experimental setup around the sample cell. In comparison to Figure 3.7, the $20\times$ objective 2 and the dichroitic mirror are shown additionally. Those two optical components focus and deflect the scanned argon-ion beam (large blue arrow) into the sample plane.

3.5. SAMPLE CELLS

We use thick sample cells to prepare highly deionized dense colloidal systems. The cells are commercially available (Hellma) and have a spacing of $200\mu\text{m}$ between bottom and top glass plate. The flow resistance is therefore low, and the samples can be connected to deionization circuits (see Section 3.6). In the following, we refer to this sample as *sample type I*. Figure 3.15 displays an illustration of sample type I.

The studies presented in Chapter 7 required thin sample cells with the spacing between the bottom and top plate slightly larger than the particle diameter. The narrow spacing is achieved through the use of spacer particles, and the sample preparation goes as follows [41]: first, a suspension of small particles is mixed with a suspension of slightly larger particles, the latter serving as spacers. We used spheres of diameters $\sigma = 1.5\mu\text{m}$ and $\sigma = 1.96\mu\text{m}$, respectively. Next, the mixture is centrifuged. The water above the sedimented particles is removed and replaced by highly deionized water. This procedure is repeated several times in order to desalt the suspension at the best. A small amount of suspension (typically $10\mu\text{l}$) is then confined between a microscope slide and a cover slip which are uniformly pressed against each other until the distance between the plates is determined by the larger particles. In contrast to the larger particles the small ones remain mobile. The system is finally sealed with epoxy resin yielding

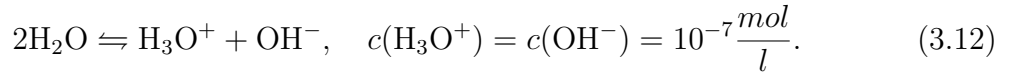
stable conditions for several weeks. In the following, we refer to this sample cell as *sample type II*.

So far, we did not manage to prepare highly deionized dense colloidal systems in samples of type II; because of the small sample volume, the confined colloidal suspension is governed by the counter ions released from the confining glass plates. As a consequence, the pair interaction is almost hard core like. In addition, sample type II is incompatible with deionization circuits (see Section 3.6); the cross sectional area is small which causes a high hydrodynamic resistance.

3.6. ADJUSTING THE PAIR INTERACTION OF COLLOIDAL SYSTEMS

We now address the question how the electrostatic pair interaction in colloidal suspensions can be manipulated experimentally.

According to (3.9) the screening length κ^{-1} inversely depends on the concentration c_{i0} of ion type i . The colloidal suspension must be therefore deionized if strong pair interaction is required. The dominant ionic contamination in experiments arises from CO_2^- -ions diffusing from the atmosphere into the sample cell. It must be mentioned that it is impossible to completely deionize colloidal suspensions due to aqueous self dissociation,



This concentration of ions is inevitably present in aqueous colloidal suspensions. The electrical conductivity σ which serves us as a measure for ionic concentrations therefore has a lower limit,

$$\sigma \geq \sigma_{\text{H}_2\text{O}} = 0.55 \frac{\mu\text{S}}{\text{cm}}. \quad (3.13)$$

To prepare strongly interacting colloidal systems, we apply a two-step deionization method. The deionization of colloidal suspensions has been described above and the additional step refers to the sample cell (type I). We do not inject colloids directly into the sample cell but instead via a continuous deionization circuit as shown in Figure 3.16. The circuit consists of a peristaltic pump and plexiglass vessels connected via tygon and teflon hoses. If necessary, we refill water via the reservoir vessel before each measurement. To deionize the circuit, the water is pumped through the vessel filled with ion-exchange resin for approximately 15min. A conductivity meter allows control of the deionization process. We typically achieve values of approximately $\sigma = 0.07 \mu\text{S}/\text{cm}$. It is not possible to reach the lower limit (3.13) due to atmospheric CO_2^- -ions diffusing into the circuit via the reservoir vessel. Colloids are injected into the circuit via the reservoir vessel and then pumped into the sample. The sample cell is finally sealed with clamps. With this, we efficiently avoid liquid flow and contamination of the sample cell with CO_2^- -ions from the reservoir vessel. The change in the screening length κ^{-1} is less

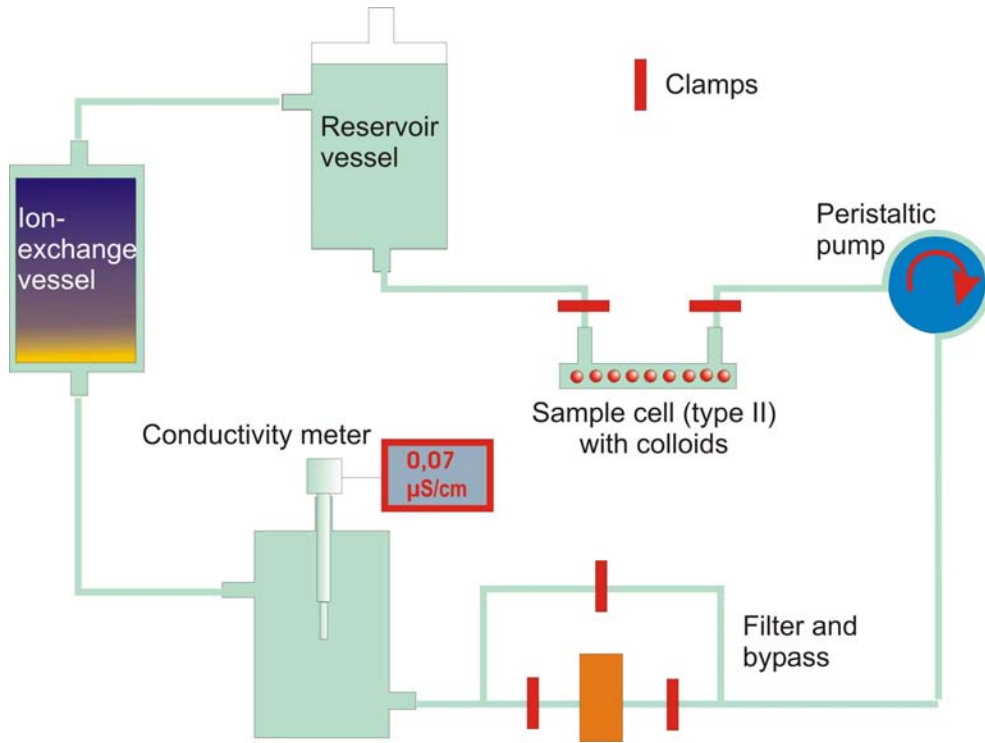


FIGURE 3.16. Continuous deionization circuit. To deionize the circuit the water is pumped through a vessel filled with ion-exchange resin. The conductivity σ can be checked by a conductivity meter which allows to control the status of deionization.

than 3% per hour. After a measurement colloids are pumped out of the sample cell and adsorbed by the filter.

To measure the screening length κ^{-1} , we determine the pair distribution function $g(r)$ of a dilute colloidal system and evaluate the pair interaction $u(r)$ using a closure relation [42] (see Section 2.4). However, the procedure has turned out to very sensitively depend on density inhomogeneities. We therefore developed a new density independent method evaluating pair interactions directly from two-particle distance distributions (see Chapter 7). In addition, we have recently found that pair interactions can be determined from the phononic band structure of a 2D crystal. A detailed discussion of this idea is provided in [43].

The experimental setup presented in this chapter has not been used in the experimental studies on structural crossover in binary mixtures (see Chapter 5). Both a commercial confocal microscope and a different sample type were employed. This is discussed separately in Chapter 5 to avoid confusion.

4

Phonon-dispersion-relation of two-dimensional crystals on substrate potentials

ABSTRACT

By exposing 2D colloidal crystals to tunable substrate potentials one can selectively manipulate the corresponding phonon band-structure. We explore this idea theoretically and experimentally by studying the lattice dynamics of 2D colloidal crystals in the presence of 1D and 2D periodic substrate potentials created by interfering laser beams. The phonon spectrum is obtained experimentally from particle dynamics observed with video microscopy and the theoretical analysis is based on calculations of 2D crystal elastic energies using the harmonic approximation. Depending on the substrate geometry and strength, the phonon spectra can be substantially changed which is in agreement with our theoretical calculations.

4.1. INTRODUCTION

It is common knowledge that crystal lattice vibrations are well described in the framework of the so-called harmonic approximation [44]; here, springs serve as an approximate model for the pair interaction between crystal atoms. As a result, the collective lattice vibrations separate into a set of independent harmonic oscillators referred to as phonons with the phonon dispersion relation assigning phonon frequencies to phonon wave vectors. The phonon dispersion relation is an important feature of condensed matter; besides sound properties, the phonon dispersion relation governs the thermal properties of isolators such as specific heat, heat conductivity or thermal expansion [45].

The harmonic approximation allows determination of phonon-dispersion relations in one, two and three dimensions. However, the study of 1D and 2D systems is somewhat artificial since such systems are rare in nature. Specifically, 2D systems are more likely to occur in the presence of a substrate. A good example for such combined systems are monolayers of particles adsorbed onto substrates such as films [46,47]. The phonon dispersion relation of noble-gas adsorbates on metal surfaces has already been investigated both theoretically and experimentally [48–52]; however, it has not yet been studied whether phonon dispersion relations can be systematically modified through continuously variable substrate-adsorbate interactions. If yes, a substrate would allow systematic modification of the adsorbed monolayer’s sound and thermal properties.

To explore the idea of systematic modification, we extended the theoretical framework of 2D lattice dynamics to systems where a 2D hexagonal crystal is subjected to a commensurate 1D periodic substrate potential. Similar to the pair interaction, the substrate is approximated by a set of springs, each pinning a particle to its lattice site. We computed phonon dispersion relations for various combinations and strengths of commensurate 1D periodic substrates.

To date, phonons in colloidal systems have been studied in several experiments employing Brillouin light scattering [53–57] or dynamic light scattering [58, 59]. In a recent publication by Keim et al., it has been demonstrated that phonon-dispersion relations of free 2D crystals are also directly accessible in experiments through particle trajectories recorded with video microscopy [60]. As a result, both the calculated and measured phonon dispersion relations showed excellent agreement. To verify our theoretical results, we measured, similar to Keim et al., the phonon-dispersion relation of a 2D colloidal crystal in the presence of commensurate 1D periodic light potentials (see Section 3.1).

The modification of phonon-dispersion relations through the use of external potentials is also relevant for three-dimensional (3D) solids; here, an additional anisotropic pair interaction might be the counterpart of a substrate in 2D. Besides manipulation of

sound and thermal properties, the systematic modification of phonon dispersion relations might allow creation of so-called phononic crystals which possess a phononic band gap [61–63]. Phononic crystals are also termed deaf materials because sound with a frequency within the band gap is reflected. Similar to photonic crystals which are blind materials [20], there is an ongoing competition to discover materials exhibiting large phononic band gaps. In this context, systematic modification of phononic dispersion relations has been recently reported [64, 65].

This chapter is organized as follows: we first summarize the essentials of the theory of lattice dynamics and briefly describe the experimental approach of Keim et al. [60] in Section 4.2. Next, we discuss our theoretical and experimental approach in Section 4.3 and Section 4.4, respectively. Section 4.5 then provides the presentation of our theoretical and experimental results whose relevance for condensed matter is discussed in Section 4.6. We finally conclude this chapter in Section 4.7. In addition, the Appendices 4.8 and 4.9 provide detailed information on phonon dynamics and on measurement of lattice sites with video microscopy.

4.2. BASIC FORMALISM AND STATE OF THE ART

To provide an introduction to our studies on phonon-dispersion relations we start by briefly recapitulating the essentials of the classical theory of lattice dynamics [44]. We consider a 2D triangular crystal of N Brownian particles as illustrated in Figure 4.1A. Let $\mathbf{r} = (r_x, r_y)$ and $\Phi(\mathbf{r}, \mathbf{r}')$ denote the particle positions and the pair interaction, respectively. The basic lattice vectors are

$$\hat{\mathbf{b}}_1 = a\hat{\mathbf{e}}_y, \quad (4.1)$$

$$\hat{\mathbf{b}}_2 = \frac{\sqrt{3}a}{2}\hat{\mathbf{e}}_x - \frac{a}{2}\hat{\mathbf{e}}_y \quad (4.2)$$

with $\hat{\mathbf{e}}_x = (1, 0)$ and $\hat{\mathbf{e}}_y = (0, 1)$ the cartesian basis vectors and a the mean particle distance. As a consequence, the positions of the particles \mathbf{r} can be written as

$$\mathbf{r}_n = \mathbf{R}_n + \mathbf{u}_n, \quad (4.3)$$

where the

$$\mathbf{R}_n = n_1\hat{\mathbf{b}}_1 + n_2\hat{\mathbf{b}}_2, \quad \mathbf{n} = (n_1, n_2), \quad (4.4)$$

denote the lattice sites. \mathbf{u}_n refers to the displacement from the site \mathbf{R}_n and n_1, n_2 are integer numbers. To treat a infinitely large system discretely, we consider a finite

system of hexagonal symmetry, i.e.,

$$\begin{aligned}
\mathbf{n} = & (i, 0), (i, 1), \dots, (i, i-1), \\
& (i, i), (i-1, i), \dots, (1, i), \\
& (0, i), (-1, i-1), \dots, (-i+1, 1), \\
& (-i, 0), (-i, 1), \dots, (-i, -i+1), \\
& (-i, -i), (-i+1, -i), \dots, (-1, -i), \\
& (0, -i), (1, -i+1), \dots, (i-1, -1), \\
& \text{for } i = 0, \dots, N',
\end{aligned} \tag{4.5}$$

with N' a positive even integer. This scheme is interpreted as follows: we obtain the central particle $\mathbf{n} = (0, 0)$ for $i = 0$ and then construct the hexagonal crystal through the use of hexagonal shells with the corners located at a distance $i \cdot a$ from the central particle; for instance, the first shell $i = 1$ consists of the nearest neighbors $\mathbf{n} = (1, 0), (1, 1), (0, 1), (-1, 0), (-1, -1), (0, -1)$ and the second shell $i = 2$ contains the twelve particles $\mathbf{n} = (2, 0), (2, 1), (2, 2), (1, 2), (0, 2), (-1, 1), (-2, 0), (-2, -1), (-2, -2), (-1, -2), (0, -2), (1, -1)$. The total number of particles equals

$$N = 1 + \sum_{i=1}^{N'} 6i. \tag{4.6}$$

If we apply periodic boundary conditions, the finite system (4.5) represents the infinite one.

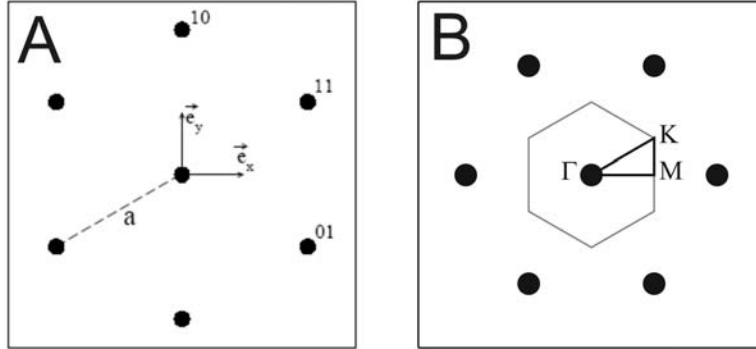


FIGURE 4.1. A) Sketch of a 2D triangular crystal. The central particle $\mathbf{n} = (0, 0)$ and its nearest neighbors $\mathbf{n} = (1, 0), (1, 1), (0, 1), (-1, 0), (-1, -1), (0, -1)$ are shown as black spots and a denotes the mean particle distance. B) Inverse lattice. The grey solid line indicates the first Brillouin zone and the black solid line its irreducible part. Γ , M and K represent points of high symmetry according to the terminology of group-theory.

Summing up all the particle pair interactions yields the total energy

$$V = \sum_{\substack{\mathbf{n}, \mathbf{n}' \\ \mathbf{n} \neq \mathbf{n}'}} \Phi(\mathbf{r}_{\mathbf{n}}, \mathbf{r}_{\mathbf{n}'}). \quad (4.7)$$

We perform a Taylor-series in $\mathbf{u}_{\mathbf{n}} - \mathbf{u}_{\mathbf{n}'}$ around the equilibrium configuration $\mathbf{r}_{\mathbf{n}} = \mathbf{R}_{\mathbf{n}}$ leading to the harmonic approximation provided that $|\mathbf{u}_{\mathbf{n}}| \ll a$,

$$V = V_0 + \frac{1}{2} \sum_{\substack{\mathbf{n}, \mathbf{n}', \alpha, \beta \\ \mathbf{n} \neq \mathbf{n}'}} u_{\mathbf{n}\alpha} \Phi_{\mathbf{nn}'\alpha\beta} u_{\mathbf{n}'\beta}, \quad (4.8)$$

where

$$\Phi_{\mathbf{nn}'\alpha\beta} = \left. \frac{\partial^2 \Phi(\mathbf{r}, \mathbf{r}')}{\partial r_{\alpha} \partial r_{\beta}} \right|_{\mathbf{r}=\mathbf{R}_{\mathbf{n}}, \mathbf{r}'=\mathbf{R}_{\mathbf{n}'}} \quad (4.9)$$

is the second derivative of the pair-interaction and $\alpha, \beta = x, y$. V_0 is a constant term which is unimportant for the following considerations therefore set to zero. The linear term in the Taylor-expansion vanishes because V is minimized for the equilibrium configuration. In the harmonic approximation, the 2D crystal is described as a system of N particles that are connected via springs. The spring constant associated with two particles at positions $\mathbf{r}_{\mathbf{n}}$ and $\mathbf{r}_{\mathbf{n}'}$ is given by $\Phi_{\mathbf{nn}'\alpha\beta}$. We introduce the dynamical matrix

$$D_{\mathbf{n}-\mathbf{n}', \alpha\beta} = \delta_{\mathbf{nn}'} \sum_{\mathbf{n}''} \Phi_{\mathbf{nn}''\alpha\beta} - \Phi_{\mathbf{nn}'\alpha\beta} \quad (4.10)$$

to write (4.8) as

$$V = \frac{1}{2} \sum_{\mathbf{n}, \mathbf{n}', \alpha, \beta} u_{\mathbf{n}\alpha} D_{\mathbf{n}-\mathbf{n}', \alpha\beta} u_{\mathbf{n}'\beta}. \quad (4.11)$$

The dynamical matrix depends on $\mathbf{R}_{\mathbf{n}} - \mathbf{R}_{\mathbf{n}'}$ because the crystal is invariant when subjected to a rigid body translation.

Before we apply a Fourier-transformation to (4.11) we must discuss the allowed \mathbf{q} -vectors of phonons. The basic vectors of the inverse lattice of (4.1) and (4.2) are (see Figure 4.1B)

$$\hat{\mathbf{G}}_1 = \frac{2\pi}{\sqrt{3}a} \hat{\mathbf{e}}_x + \frac{2\pi}{a} \hat{\mathbf{e}}_y, \quad (4.12)$$

$$\hat{\mathbf{G}}_2 = \frac{4\pi}{\sqrt{3}a} \hat{\mathbf{e}}_x. \quad (4.13)$$

Hence, the first Brillouin zone (BZ) is spanned by the following basic vectors,

$$\hat{\mathbf{B}}_1 = \frac{4\pi}{3aN'} \hat{\mathbf{e}}_y, \quad (4.14)$$

$$\hat{\mathbf{B}}_2 = \frac{2\pi}{\sqrt{3}aN'} \hat{\mathbf{e}}_x - \frac{2\pi}{3aN'} \hat{\mathbf{e}}_y, \quad (4.15)$$

and the set of allowed \mathbf{q} -vectors reads

$$\mathbf{q}_m = m_1 \hat{\mathbf{B}}_1 + m_2 \hat{\mathbf{B}}_2, \quad (4.16)$$

with \mathbf{m} an element of the set (4.5). With this, we are now able to formulate the Fourier-transforms of the displacements,

$$\tilde{u}_{\mathbf{m}\alpha} = \frac{1}{\sqrt{N}} \sum_{\mathbf{n}} u_{\mathbf{n}\alpha} \exp(-i\mathbf{q}_{\mathbf{m}}\mathbf{R}_{\mathbf{n}}), \quad (4.17)$$

$$u_{\mathbf{n}\alpha} = \frac{1}{\sqrt{N}} \sum_{\mathbf{m}} \tilde{u}_{\mathbf{m}\alpha} \exp(i\mathbf{q}_{\mathbf{m}}\mathbf{R}_{\mathbf{n}}), \quad (4.18)$$

and of the dynamical matrices,

$$\begin{aligned} \tilde{D}_{\mathbf{m}\alpha\beta} &= \frac{1}{N} \sum_{\mathbf{n}, \mathbf{n}'} D_{\mathbf{n}-\mathbf{n}', \alpha\beta} \exp\left(-i(\mathbf{q}_{\mathbf{m}}\mathbf{R}_{\mathbf{n}} + \mathbf{q}_{\mathbf{m}'}\mathbf{R}_{\mathbf{n}'})\right) \\ &= \sum_{\mathbf{n}} D_{\mathbf{n}\alpha\beta} \exp(-i\mathbf{q}_{\mathbf{m}}\mathbf{R}_{\mathbf{n}}). \end{aligned} \quad (4.19)$$

The latter follows from the invariance under rigid-body translations where we have used $1 = \exp(i(\mathbf{q}_{\mathbf{m}}\mathbf{R}_{\mathbf{n}'} - \mathbf{q}_{\mathbf{m}'}\mathbf{R}_{\mathbf{n}'}))$ and the first of the two equalities

$$\delta_{\mathbf{m}\mathbf{m}'} = \frac{1}{N} \sum_{\mathbf{n}} \exp\left(-i(\mathbf{q}_{\mathbf{m}} - \mathbf{q}_{\mathbf{m}'})\mathbf{R}_{\mathbf{n}}\right), \quad (4.20)$$

$$\delta_{\mathbf{n}\mathbf{n}'} = \frac{1}{N} \sum_{\mathbf{m}} \exp\left(-i\mathbf{q}_{\mathbf{m}}(\mathbf{R}_{\mathbf{n}} - \mathbf{R}_{\mathbf{n}'})\right). \quad (4.21)$$

Employing (4.20) and (4.21) again yields the expression for the potential energy V in Fourier-space,

$$V = \frac{1}{2} \sum_{\mathbf{m}, \alpha, \beta} \tilde{u}_{\mathbf{m}\alpha}^* \tilde{D}_{\mathbf{m}\alpha\beta} \tilde{u}_{\mathbf{m}\beta}. \quad (4.22)$$

Finally, the dynamical matrix can be diagonalized by solving the eigenvalue equation

$$\sum_{\beta} \tilde{D}_{\mathbf{m}\alpha\beta} e_{\mathbf{m}j\beta} = \lambda_{\mathbf{m}j} e_{\mathbf{m}j\alpha} \quad (4.23)$$

with $\lambda_{\mathbf{m}j}$ and $\mathbf{e}_{\mathbf{m}j}$ the j th eigenvalue and eigenvector, respectively. We can now switch to symmetry-adapted coordinates,

$$\mathbf{Q}_{\mathbf{m}j} = \left(\mathbf{e}_{\mathbf{m}j}^* \tilde{\mathbf{u}}_{\mathbf{m}}\right) \mathbf{e}_{\mathbf{m}j}, \quad (4.24)$$

which finally allows us to write (4.22) as

$$V = \frac{1}{2} \sum_{\mathbf{m}, j} \lambda_{\mathbf{m}j} |\mathbf{Q}_{\mathbf{m}j}|^2 = \frac{M}{2} \sum_{\mathbf{m}, j} \omega_{\mathbf{m}j}^2 |\mathbf{Q}_{\mathbf{m}j}|^2, \quad (4.25)$$

with M the mass of a particle and $\omega_{\mathbf{m}j}$ the phonon-dispersion relation

$$\omega_{\mathbf{m}j} = \sqrt{\frac{\lambda_{\mathbf{m}j}}{M}}. \quad (4.26)$$

Thus, the lattice-vibrations of a crystal consisting of N particles is described by a set of N non-interacting harmonic oscillators called phonons. These are characterized by the direction, polarization, amplitude, and frequency of their oscillation given by $\mathbf{q}_{\mathbf{m}}$, $\mathbf{Q}_{\mathbf{m}j}$, $|\mathbf{Q}_{\mathbf{m}j}|$ and $\omega_{\mathbf{m}j}$, respectively. In general, the polarizations $\mathbf{Q}_{\mathbf{m}j}$ are neither parallel

nor perpendicular to \mathbf{q}_m ; however, at least in directions of high symmetry ($\Gamma \rightarrow M$ or $\Gamma \rightarrow K$, see Figure 4.1B), this is the case and ω_{mj} is termed the longitudinal and transversal branch of the phonon-dispersion relation for $\mathbf{Q}_{mj} \parallel \mathbf{q}_m$ and $\mathbf{Q}_{mj} \perp \mathbf{q}_m$, respectively.

Atomic and colloidal crystals

To avoid confusion, we must provide a brief discussion on similarities and differences of atomic and colloidal crystals. The phonon band structure λ_{mj} only depends on the crystal structure and the spring constant; if we restrict ourselves to phonon band structures, our results are therefore valid for both atomic and colloidal crystals. However, great care has to be taken when the phonon dispersion relation $\omega_{mj} = \sqrt{\lambda_{mj}/M}$ is considered. It is not defined in the case of colloidal crystals due to the overdamped particle dynamics [66]. As a consequence, phonons do not propagate in colloidal crystals but are exponentially damped; here, the phonon dispersion relation correlates wave vectors \mathbf{q}_m with decay times T_{mj} , $T_{mj} = \gamma/\lambda_{mj}$ with γ the coefficient of friction; a detailed discussion is provided in Section 4.8.

In the following, we will sketch how to evaluate the phonon band structure λ_{mj} both analytically and experimentally. The theoretical approach first evaluates (4.9) for a known pair-interaction. In the case of central forces, (4.9) takes the form (equation 29.3 in [44]),

$$\Phi_{\mathbf{n}\mathbf{0}\alpha\beta} = \left[-p_1(|\mathbf{R}|)\delta_{\alpha\beta} - p_2(|\mathbf{R}|)\frac{R_\alpha R_\beta}{|\mathbf{R}|^2} \right]_{\mathbf{R}=\mathbf{R}_n}, \quad (4.27)$$

with

$$p_1(r) = \frac{1}{r} \frac{d\Phi(r)}{dr}, \quad p_2(r) = \frac{d^2\Phi(r)}{dr^2} - \frac{1}{r} \frac{d\Phi(r)}{dr}. \quad (4.28)$$

Evaluating (4.10) and (4.19) yields the dynamical matrix

$$\begin{aligned} \tilde{D}_{\mathbf{m}\alpha\beta} &= - \sum_{\mathbf{n}>\mathbf{0}} \Phi_{\mathbf{n}\mathbf{0}\alpha\beta} c_{\mathbf{n}\mathbf{m}} \\ &= p_1(|\mathbf{R}_n|)\delta_{\alpha\beta} \sum_{\mathbf{n}>\mathbf{0}} c_{\mathbf{n}\mathbf{m}} + p_2(|\mathbf{R}_n|) \sum_{\mathbf{n}>\mathbf{0}} \frac{R_{n\alpha} R_{n\beta}}{|\mathbf{R}_n|^2} c_{\mathbf{n}\mathbf{m}}, \end{aligned} \quad (4.29)$$

where we used $\Phi_{\mathbf{n}\mathbf{0}\alpha\beta} = \Phi_{-\mathbf{n}\mathbf{0}\alpha\beta}$ and the abbreviation

$$c_{\mathbf{n}\mathbf{m}} = 2(1 - \cos(\mathbf{q}_m \mathbf{R}_n)). \quad (4.30)$$

Depending on the range of the pair interaction $\Phi(r)$, (4.29) is evaluated for a sufficient number of nearest-neighbor-shells. It is common use to plot λ_{mj} or ω_{mj} along a path around the irreducible part of the first BZ (see black solid lines in Figure 4.1B). The irreducible part contains all the information about λ_{mj} or ω_{mj} and is repeated in the

rest of the first BZ. In [60], (4.29) has been evaluated for 17 shells for the case of a magnetic dipole-dipole-interaction

$$\Phi(r) = \frac{\Gamma}{(\sqrt{\pi}\rho r)^3}, \quad (4.31)$$

with Γ the plasma parameter representing the interaction strength and ρ the particle density. The result is shown in Figure 4.2 as a black solid line.

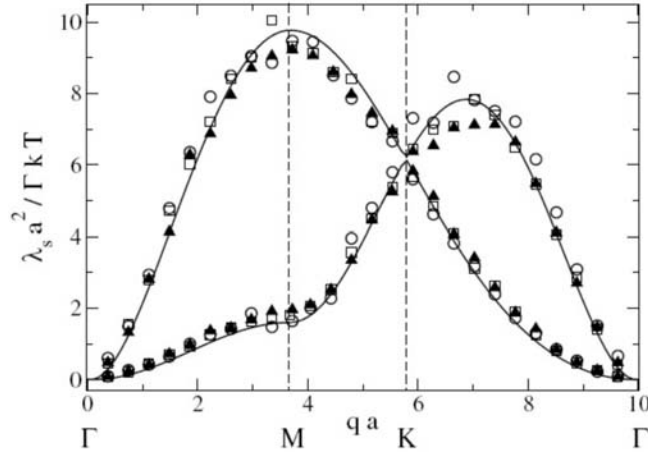


FIGURE 4.2. Band structure λ_s (corresponding to $\lambda_{\mathbf{m}_j}$ used in the text) of a 2D triangular crystal plotted along the irreducible path of the first BZ (see Figure 4.1B). The solid line represents the band structure evaluated according to (4.29). 17 nearest-neighbor shells were taken into account. The symbols correspond to experimental data evaluated according to (4.32) ($\Gamma = 75, 175, 250$ for circles, rectangles, triangles).

The experimental approach is based on the potential energy (4.22). In thermal equilibrium, the equipartition theorem demands that every term in the sum of (4.22) has an average energy of $k_B T/2$ with k_B Boltzmann's constant and T the temperature,

$$\tilde{D}_{\mathbf{m}\alpha\beta} = \frac{k_B T}{\langle \tilde{u}_{\mathbf{m}\alpha}^*(t) \tilde{u}_{\mathbf{m}\beta}(t) \rangle_t}. \quad (4.32)$$

$\langle \dots \rangle_t$ refers to the temporal average which is equal to the configurational average. The Fourier transforms $\tilde{u}_{\mathbf{m}\alpha}(t)$ are evaluated from the trajectories $\mathbf{r}(t)$ recorded by means of video microscopy. The procedure will be discussed in detail in the experimental Section 4.4. Diagonalizing the dynamical matrix $\tilde{D}_{\mathbf{m}\alpha\beta}$ finally yields the eigenvalues $\lambda_{\mathbf{m}_j}$. On top of the theoretical evaluation, the $\lambda_{\mathbf{m}_j}$ were also determined experimentally in [60]. The authors used paramagnetic particles interacting via the dipole-dipole-interaction (4.31). In Figure 4.2, the experimental data $\lambda_{\mathbf{m}_j}$ are depicted as symbols for different strengths Γ of the pair-interaction. As can be seen, the experimental data agree very well with the calculated curve.

4.3. THEORETICAL APPROACH

In our studies, we consider 1D periodic substrate potentials of the form

$$U(\mathbf{r}) = U_0(1 - \cos(\mathbf{K}\mathbf{r})). \quad (4.33)$$

Here, we concentrate on commensurate substrates, where the wave vector \mathbf{K} equals a reciprocal lattice vector $\mathbf{G}_l = l_1\hat{\mathbf{G}}_1 + l_2\hat{\mathbf{G}}_2$ with $\hat{\mathbf{G}}_1, \hat{\mathbf{G}}_2$ from (4.12) and (4.13) and with integers l_1, l_2 . In this case, every particle of the crystal is located in a trough of the 1D periodic substrate; however, not every trough is necessarily occupied by particles. In the following, we use the following \mathbf{K} -vectors,

$$\begin{aligned} \mathbf{K}_A &= \mathbf{0} \quad (U_0 = 0), \\ \mathbf{K}_B &= \hat{\mathbf{G}}_2 = \frac{4\pi}{\sqrt{3}a}\hat{\mathbf{e}}_x, \\ \mathbf{K}_C &= \hat{\mathbf{G}}_1 + \hat{\mathbf{G}}_2 = \frac{2\sqrt{3}\pi}{a}\hat{\mathbf{e}}_x + \frac{2\pi}{a}\hat{\mathbf{e}}_y, \\ \mathbf{K}_D &= \hat{\mathbf{G}}_1 = \frac{2\pi}{\sqrt{3}a}\hat{\mathbf{e}}_x + \frac{2\pi}{a}\hat{\mathbf{e}}_y, \\ \mathbf{K}_E &= 2\hat{\mathbf{G}}_1 - \hat{\mathbf{G}}_2 = \frac{4\pi}{a}\hat{\mathbf{e}}_y \end{aligned} \quad (4.34)$$

and study the corresponding substrates for six combinations of $\mathbf{K}_1 = |\mathbf{K}_1|\hat{\mathbf{K}}_1$ and $\mathbf{K}_2 = |\mathbf{K}_2|\hat{\mathbf{K}}_2$,

$$\begin{aligned} \text{case a:} & \quad \mathbf{K}_1 = \mathbf{K}_B \text{ and } \mathbf{K}_2 = \mathbf{K}_A, \\ \text{case b:} & \quad \mathbf{K}_1 = \mathbf{K}_A \text{ and } \mathbf{K}_2 = \mathbf{K}_C, \\ \text{case c:} & \quad \mathbf{K}_1 = \mathbf{K}_B \text{ and } \mathbf{K}_2 = \mathbf{K}_C, \\ \text{case d:} & \quad \mathbf{K}_1 = \mathbf{K}_B \text{ and } \mathbf{K}_2 = \mathbf{K}_D, \\ \text{case e:} & \quad \mathbf{K}_1 = \mathbf{K}_B \text{ and } \mathbf{K}_2 = \mathbf{K}_E, \\ \text{case f:} & \quad \mathbf{K}_1 = \mathbf{K}_C \text{ and } \mathbf{K}_2 = \mathbf{K}_E. \end{aligned} \quad (4.35)$$

Note that only a single 1D substrate is present for the cases a and b while two 1D substrates are superimposed in the cases c to f (see illustration in Figure 4.3). The six cases considered here comprise all possibilities if one concentrates on modulations in one or two directions and first and second order Bragg peaks only.

To implement the substrates into the formalism of harmonic lattice dynamics, we expand (4.33) in a Taylor-series around the lattice sites \mathbf{R}_n ,

$$U(\mathbf{u}) = \frac{U_0|\mathbf{K}|^2}{2}(\hat{\mathbf{K}}\mathbf{u})^2 + \mathcal{O}((\hat{\mathbf{K}}\mathbf{u})^3). \quad (4.36)$$

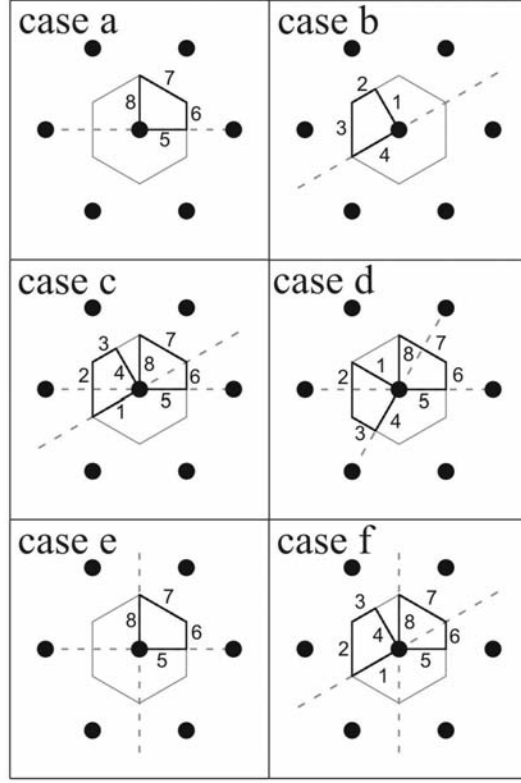


FIGURE 4.3. Reciprocal lattice (black spots) and first BZ (gray solid line) of a 2D hexagonal crystal (see Figure 4.1B). The crystal is subjected to commensurate periodic substrate potentials with modulations in different directions (dashed lines). The path enclosing the irreducible section of the first BZ is plotted as black solid line. The numbers label the sections of this path along which the band structure is determined.

For small displacements $|\mathbf{u}| \ll a$, we can neglect the terms of order higher than two. Hence, the substrate potentials for the six cases (4.35) become

$$\begin{aligned}
 V_{ext} &= \frac{1}{2} \sum_{\mathbf{n}} \left(U_0^1 |\mathbf{K}_1|^2 (\hat{\mathbf{K}}_1 \mathbf{u}_{\mathbf{n}})^2 + U_0^2 |\mathbf{K}_2|^2 (\hat{\mathbf{K}}_2 \mathbf{u}_{\mathbf{n}})^2 \right) \\
 &= \frac{1}{2} \sum_{\mathbf{n}, \mathbf{n}', \alpha, \beta} u_{\mathbf{n}\alpha} \delta_{\mathbf{n}\mathbf{n}'} \left(U_0^1 |\mathbf{K}_1|^2 \hat{K}_{1\alpha} \hat{K}_{1\beta} + U_0^2 |\mathbf{K}_2|^2 \hat{K}_{2\alpha} \hat{K}_{2\beta} \right) u_{\mathbf{n}'\beta}. \quad (4.37)
 \end{aligned}$$

Use of (4.21) allows expression of V_{ext} in Fourier-space,

$$V_{ext} = \frac{1}{2} \sum_{\mathbf{m}, \alpha, \beta} \tilde{u}_{\mathbf{m}\alpha} \tilde{D}_{\mathbf{m}\alpha\beta}^{(ext)} \tilde{u}_{\mathbf{m}\beta}, \quad (4.38)$$

with the dynamical matrix

$$\tilde{D}_{\mathbf{m}\alpha\beta}^{(ext)} = U_0^1 |\mathbf{K}_1|^2 \hat{K}_{1\alpha} \hat{K}_{1\beta} + U_0^2 |\mathbf{K}_2|^2 \hat{K}_{2\alpha} \hat{K}_{2\beta}. \quad (4.39)$$

In conclusion, the substrate leads to an additional dynamical matrix which is added to the dynamical matrix $\tilde{D}_{\mathbf{m}\alpha\beta}$ of the free crystal (4.29). The total dynamical matrix of

the system can now be written as

$$\tilde{D}_{\mathbf{m}\alpha\beta}^{(tot)} = \tilde{D}_{\mathbf{m}\alpha\beta} + \tilde{D}_{\mathbf{m}\alpha\beta}^{(ext)} \quad (4.40)$$

and the eigenvalues $\lambda_{\mathbf{m}j}$ of $\tilde{D}_{\mathbf{m}j}$ yield the phonon band structure.

In our studies, we considered charge-stabilized colloidal particles interacting via a Yukawa-like pair potential (2.10). Here, the parameters (4.28) take the form

$$\begin{aligned} p_1(r) &= -\frac{\Phi(r)}{r^2}(\kappa r + 1), \\ p_2(r) &= \frac{\Phi(r)}{r^2}\left((\kappa r)^2 + 3\kappa r + 3\right). \end{aligned} \quad (4.41)$$

Since $\kappa a \approx 15$ typically, we can neglect p_1 compared to p_2 . In addition, it is sufficient to sum over the first nearest-neighbor shell because of the short-ranged nature of $\Phi(r)$, i.e., $\Phi(r) \approx 0$ for $r > a$. Hence, the total dynamical matrix simplifies to

$$\frac{\tilde{D}_{\mathbf{m}\alpha\beta}^{(tot)}}{k_0} = 2 \sum_{\nu=1}^3 \hat{e}_{\nu\alpha} \hat{e}_{\nu\beta} \left(1 - \cos(a\mathbf{q}_m \hat{e}_\nu)\right) + \frac{k_1}{k_0} K_{1\alpha} K_{1\beta} + \frac{k_2}{k_0} K_{2\alpha} K_{2\beta}, \quad (4.42)$$

where we have introduced the spring constants

$$k_0 = p_2(a), \quad k_1 = U_0^1 |\mathbf{K}_1|^2, \quad k_2 = U_0^2 |\mathbf{K}_2|^2, \quad (4.43)$$

and the three vectors

$$\hat{e}_1 = \hat{e}_y, \quad \hat{e}_2 = \frac{\sqrt{3}}{2} \hat{e}_x + \frac{1}{2} \hat{e}_y, \quad \hat{e}_3 = \frac{\sqrt{3}}{2} \hat{e}_x - \frac{1}{2} \hat{e}_y. \quad (4.44)$$

4.4. EXPERIMENTAL APPROACH

We experimentally generated our substrate potentials by interfering laser beams according to the basic techniques outlined in Section 3.1. Four laser beams were arranged at positions (see (3.9) and Figure 3.7),

$$\begin{aligned} \mathbf{X}_1 &= \frac{s_1}{2} \hat{e}_2, & \mathbf{X}_2 &= -\frac{s_1}{2} \hat{e}_2, \\ \mathbf{X}_3 &= \frac{s_2}{2} \hat{e}_1, & \mathbf{X}_4 &= -\frac{s_2}{2} \hat{e}_1. \end{aligned} \quad (4.45)$$

The corresponding wave vectors in the sample plane are

$$\begin{aligned} \mathbf{K}'_1 &= \frac{\pi s_1}{\lambda f} \hat{e}_x, & \mathbf{K}'_2 &= -\frac{\pi s_1}{\lambda f} \hat{e}_x \\ \mathbf{K}'_3 &= \frac{\pi s_2}{\lambda f} \hat{e}_y, & \mathbf{K}'_4 &= -\frac{\pi s_2}{\lambda f} \hat{e}_y. \end{aligned} \quad (4.46)$$

With this, we created light-induced substrates of the form (4.33) and realized case e in (4.35),

$$U_1(\mathbf{r}) = U_0^1 \left(1 - \cos(\mathbf{K}_1 \mathbf{r})\right), \quad \mathbf{K}_1 = 2\mathbf{K}'_1, \quad (4.47)$$

$$U_2(\mathbf{r}) = U_0^2 \left(1 - \cos(\mathbf{K}_2 \mathbf{r})\right), \quad \mathbf{K}_2 = 2\mathbf{K}'_3. \quad (4.48)$$

By now inserting \mathbf{K}_1 and \mathbf{K}_2 from (4.35) (case e) it follows that

$$U_1(x) = U_0^1 \left(1 - \cos \left(\frac{2\pi}{d_1} x \right) \right), \quad d_1 = \frac{2\pi}{|\mathbf{K}_1|} = \frac{\sqrt{3}}{2} a, \quad (4.49)$$

$$U_2(y) = U_0^2 \left(1 - \cos \left(\frac{2\pi}{d_2} y \right) \right), \quad d_2 = \frac{2\pi}{|\mathbf{K}_4|} = \frac{a}{2}, \quad (4.50)$$

with d_1 and d_2 the corresponding periodicity. Figure 4.4A and B illustrate $U_1(x)$ (case a) and both $U_1(x)$ and $U_2(y)$ (case e). Because $\mathbf{K}_1 = 2\mathbf{K}'_1$ and $\mathbf{K}_2 = 2\mathbf{K}'_3$ we are able to determine the required distances between the laser beams,

$$s_1 = \frac{\lambda f}{d_1} = \frac{2\lambda f}{\sqrt{3}a}, \quad s_2 = \frac{\lambda f}{d_2} = \frac{2\lambda f}{a}. \quad (4.51)$$

To avoid interference between the two light-induced substrates, we generate them by means of two YV₄O-lasers ($\lambda = 532nm$). The lasers creating $U_1(\mathbf{r})$ and $U_2(\mathbf{r})$ emitted powers up to $5.5W$ and $2.2W$, respectively.

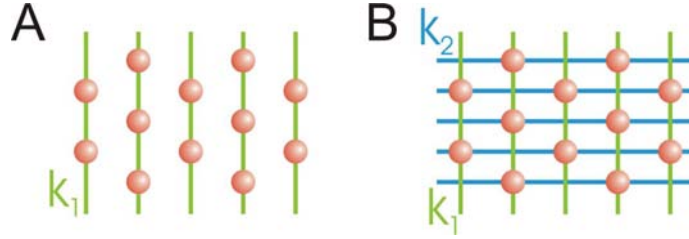


FIGURE 4.4. Sketch of the substrates used in the experimental studies. The colloidal crystal is indicated by red spots. A) Substrate corresponding to case a in Figure 4.3 and (4.35). B) Substrate corresponding to case e in Figure 4.3 and (4.35).

Our colloidal suspension consisted of polystyrene spheres of diameter $\sigma = 2.4\mu m$ suspended in water. The particles were injected into the sample (type I, see Section 3.5) via a deionization circuit (see Section 3.6) and we prepared a spontaneous crystal by means of the scanned optical tweezers (see Section 3.4). We then determined the mean particle distance a and adjusted the distance between the laser beams s_1 and s_2 according to (4.51). Typically, $a \approx 5\mu m$ and hence, $s_1 \approx 1.2cm$ and $s_2 \approx 2cm$.

For a single set of parameters $(k_0, k_1/k_0, k_2/k_0)$ we recorded up to 5.000 images at a frequency of $2Hz$. From these, we took a section of hexagonal shape according to (4.5) and obtained a set of N trajectories $\mathbf{r}_n(t)$ and their corresponding displacements $\mathbf{u}_n(t) = \mathbf{r}_n(t) - \mathbf{R}_n$. Finally, we evaluate the dynamical matrix according to (4.32) and calculate its eigenvalues λ_{m_j} . It must be mentioned that an accurate determination of the lattice sites \mathbf{R}_n is non trivial due to fundamental physical and technical reasons, covered in detail in Section 4.9. Here, we discuss the current state of the art which is to determine \mathbf{R}_n by means of temporal averaging. Let T and $\Delta t < T$ be the total period

of a single measurement and a time-window, respectively. We then define $\mathbf{R}_n(t)$ as

$$\mathbf{R}_n(t) := \frac{1}{\Delta t} \int_{t-\Delta t/2}^{t+\Delta t/2} dt' \mathbf{r}_n(t'), \quad (4.52)$$

and hence,

$$\mathbf{u}_n(t) = \mathbf{r}_n(t) - \mathbf{R}_n(t) \text{ for } t \in [\Delta t/2, T - \Delta t/2]. \quad (4.53)$$

(4.52) is equivalent to a smoothing of the trajectories $\mathbf{r}_n(t)$; typically, we used 60 frames, i.e., $\Delta t = 30s$. To determine Δt we checked if the displacements $\mathbf{u}_n(t)$ are distributed symmetrically around the lattice sites and Δt is increased if the distribution is asymmetric. With this, we intent to account for asymmetric temporal drifts and, at the same time, not to cut phonon frequencies as accurately as possible.

4.5. THEORETICAL AND EXPERIMENTAL RESULTS

First, we chose an arbitrary set of parameters ($k_1/k_0 = k_2/k_0 = 4$) and determined the eigenvalues of the dynamical matrix by evaluating (4.42) for all the six cases in (4.35). For simplicity, we will not explicitly refer to the allowed phonon modes by the index \mathbf{m} in the following. We just use \mathbf{q} , \mathbf{Q} and λ where the latter will be termed the bands. The results of our calculations are shown in Figure 4.5 where λ is plotted along the path around the irreducible section of the first BZ. Those paths are displayed for each case in Figure 4.3 which also provides the numbering of the path sections. First of all, at least one of the two bands is considerably shifted upwards for all the six cases a-f. To highlight this, we also plotted the bands of the free crystal as gray dashed lines. The shift of the bands is expected because bands which have a polarization vector \mathbf{Q} not perpendicular to \mathbf{K}_1 or \mathbf{K}_2 are affected by the corresponding substrate $U_1(\mathbf{r})$ or $U_2(\mathbf{r})$. As an intuitive picture, one can think about the crystal particles moving parallel or perpendicular to the potential troughs. Of course, the motion is not affected in the former case and becomes smaller in the latter. This also explains why the asymmetry in the shift of the two bands decreases from case c to e since the angle between \mathbf{K}_1 and \mathbf{K}_2 becomes larger. The asymmetry is the same for case d and f because the angle between \mathbf{K}_1 and \mathbf{K}_2 is identical. In addition to vertical shifts, the substrate potentials also alter the shape of the bands along certain sections of the irreducible paths. For instance, there are several sections where one of the bands is completely truncated (section 7 in case a and c, sections 2 and 6 in case f). The modification of the band shape cannot be explained intuitively. From a theoretical point of view, band-shape modification occurs if the band polarizations \mathbf{Q} do not point parallel or perpendicular to \mathbf{K}_1 and \mathbf{K}_2 . Consequently, at least one of the substrate potentials manipulates both bands simultaneously. The symmetry of the band-structure in case c with respect to the path sections 4 – 1 and 5 – 8 arises because $k_1 = k_2$. It vanishes if $k_1 \neq k_2$. In this

respect, case e is particularly interesting. Here, the 6-fold symmetry of the free crystal is broken down to a 2-fold one if $k_1 \neq k_2 \neq 0$, but it can be restored if $k_1 = k_2$.

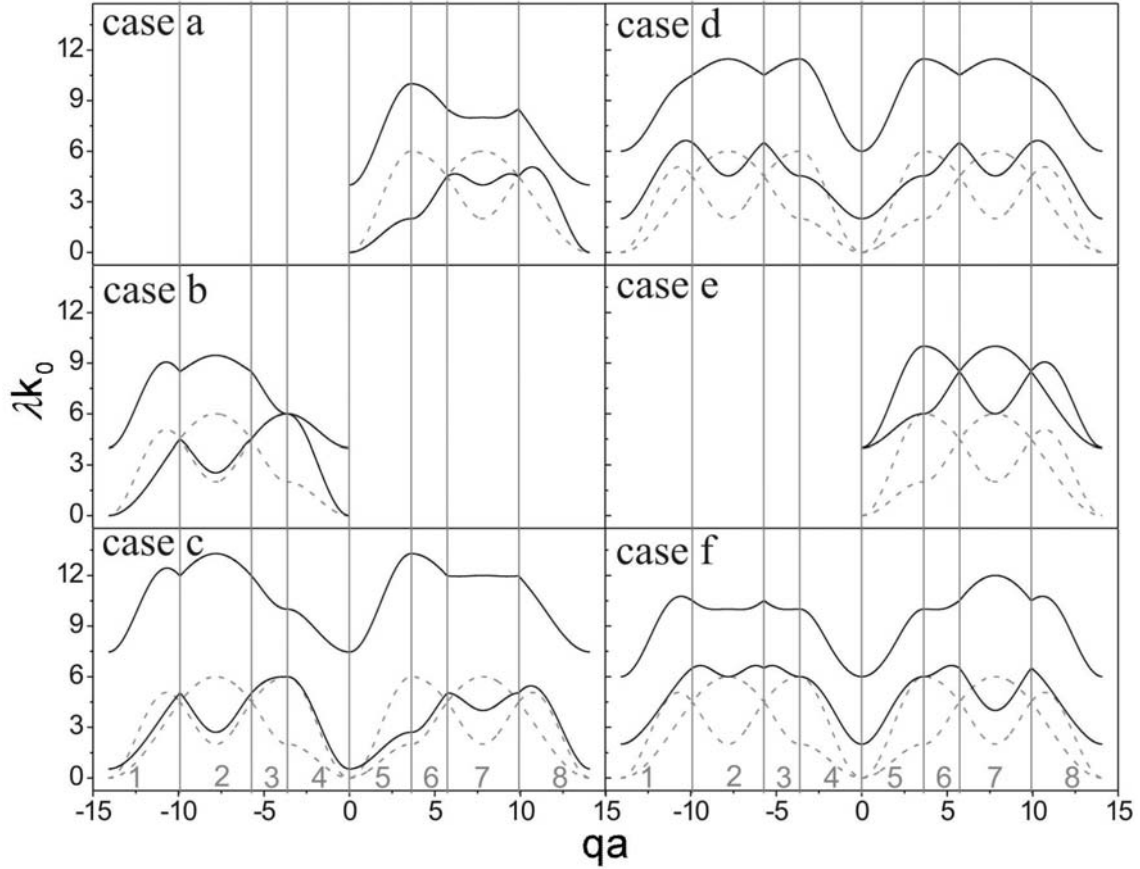


FIGURE 4.5. Band structure (black solid lines) along the the paths around the irreducible sections for the cases a-f. The paths and the numbering of their sections are provided by Figure 4.3. To stress the influence of substrate potentials on the band structure, the band structure of a free crystal is also provided as gray dashed lines. The spring constants of the substrate potentials were chosen as $k_1/k_0 = k_2/k_0 = 4$.

To verify the theoretical results we now focus on the cases a and e which were studied experimentally and, to discuss the behavior of the band structure, introduce the phonon-spectrum defined as

$$G(\lambda) = \frac{1}{2N} \sum_{m,j} \delta(\lambda - \lambda_{mj}), \quad (4.54)$$

where

$$\int_0^\infty d\lambda G(\lambda) = 1. \quad (4.55)$$

According to (4.55), $G(\lambda)$ can be interpreted as the fraction of eigenvalues of the dynamical matrix to be found in the interval $[\lambda, \lambda + d\lambda]$. In Figure 4.6A, the phonon band structure and the phonon spectrum of a free crystal are shown. We observe two

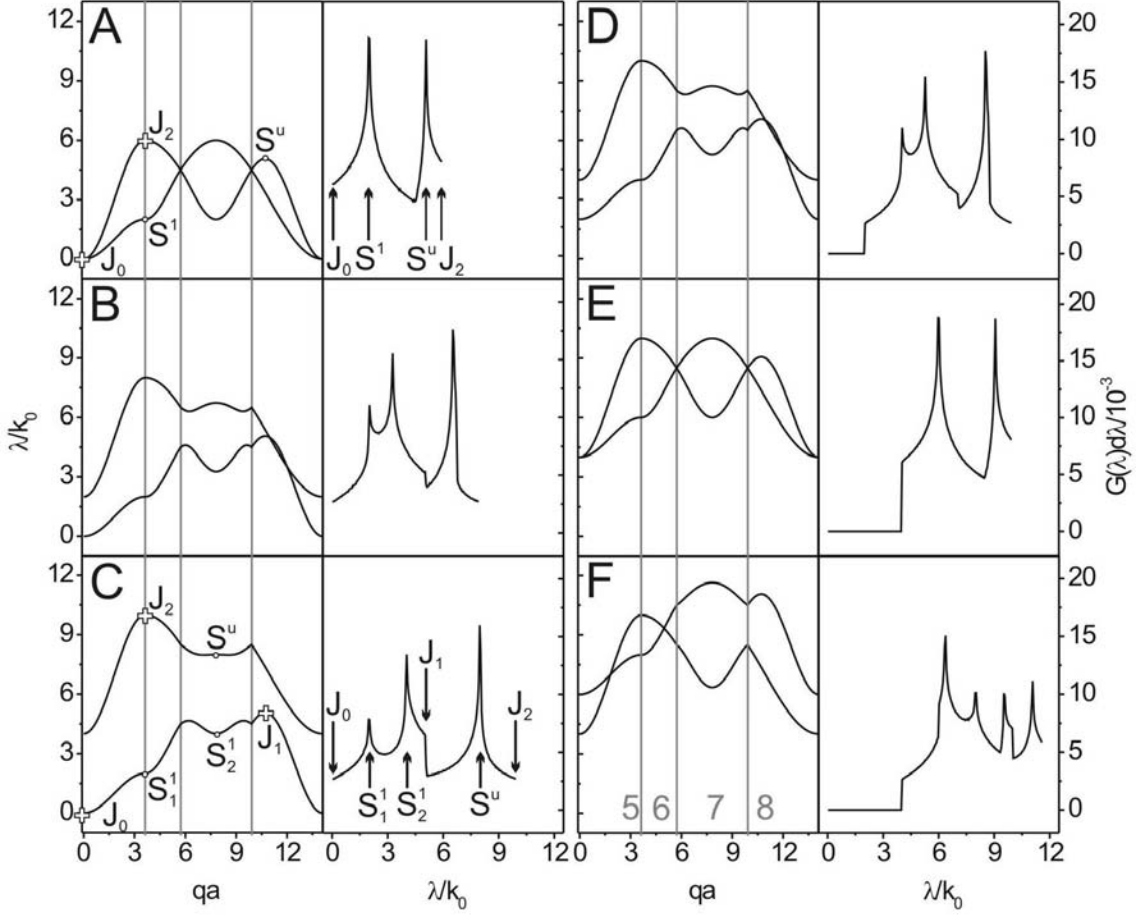


FIGURE 4.6. Case a A)-C) and case e A)-F). Band structures (left graph) and band spectrum (right graph) for different combinations $(k_1/k_0, k_2/k_0)$. A) $(0, 0)$, B) $(2, 0)$, C) $(4, 0)$, D) $(4, 2)$, E) $(4, 4)$ and F) $(4, 6)$. The path around the irreducible section of the first BZ is indicated by the vertical gray lines and the numbers (see Figure 4.3). In A) and C), the singularities are indicated by the arrows and the symbols S and J refer to singularities associated with saddle-points (S), minima (J) and maxima (J).

singularities that can be fitted to a logarithmic expression $\ln |\lambda - \lambda_c|$. These logarithmic singularities correspond to the saddle-points of the band-structure λ and are denoted by S^1 and S^u . In addition, the spectrum exhibits two jump-singularities (J_0 and J_2) which arise from the minima and maxima of the band structure. Upon increasing k_1 (Figure 4.6B and C), we observe one band to be shifted and to flatten as shown in Figure 4.5. Here, we also find a strong modification of the phonon spectrum. The logarithmic singularity S_1 splits into two singularities S_1^1 and S_1^2 (Figure 4.6C); the separation between them increases with k_1 . In addition, the spectrum exhibits a new jump-singularity J_1 . In Figure 4.6D and E, k_2 increases in two steps matching finally k_1 in Figure 4.6E. Here, we observe the free crystal's bands and spectrum to be restored.

The bands and spectrums shown in Figure 4.6D and E are identical with those depicted in Figure B and A, respectively and are just shifted by a constant value with respect to each other. In Figure 4.6F, k_2 is finally larger than k_1 . Here, the bands and the spectrum are considerably deformed again. The modification greatly differs from the case where $k_1 > k_2$.

In our experimental studies, we first focused on case a and created a system according to Figure 4.4A and (4.49). The band structures λ evaluated from the recorded trajectories $\mathbf{r}(t)$ are shown as symbols in Figure 4.7 for the free crystal (Figure A) and two different laser powers $P = 1.2W$ (Figure B) and $P = 2.75W$ (Figure C) corresponding to the spring constants $k_1 = k_0$ and $k_1 = 2.5k_0$, respectively. Note that the spring constant k_1 is proportional to P (see Figure 3.2 and Section 3.1.1). The graphs also contain bands which were calculated numerically; we performed cross-checks of the fitted parameters k_0 and k_1 with the values calculated on the basis of the calibration measurements described in Section 3.1.3 and we observed deviations of approximately 10% [43]. Hence, our experimental results confirm our theoretical observations which means that we can access the entire spectrum of theoretical scenarios in experiments. In principle, P can be further increased through the use of a high-power laser; for instance, there are Nd:YVO₄-lasers available which allow light emission with $P = 18W$. As a second step, we experimentally realized case e (see Figure 4.4B, (4.49) and (4.50)). The measured band structures and spectra are depicted in Figure 4.8A-D for $(k_1, k_2) = (0, 0)$, $(1.4k_0, 0.2k_0)$, $(1.5k_0, 1.5k_0)$ and $(0.5k_0, 1.5k_0)$, respectively. Again, we find the experimental data to agree well with theoretical predictions. Unfortunately, the measured spectra suffer from large statistical noise. Nevertheless, they qualitatively follow the theoretical curves though there is still room for improvement when developing further the determination of the lattice sites (4.52). We will discuss this in Section 4.8. To

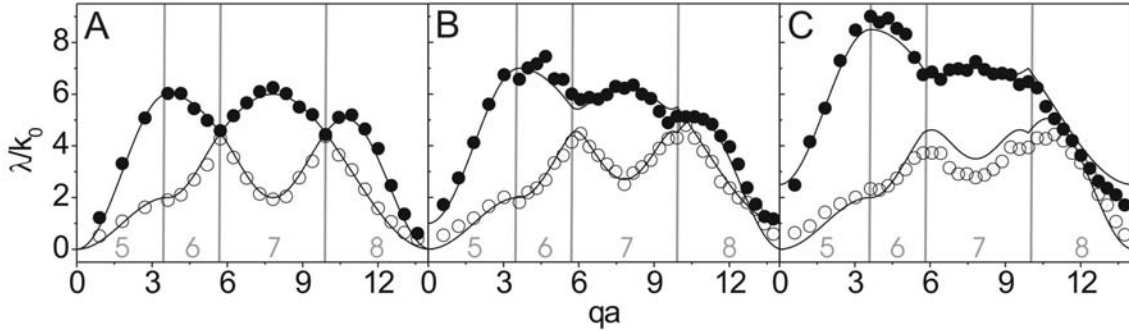


FIGURE 4.7. Case a: band-structure determined experimentally (symbols). For comparison, theoretical curves are displayed as well. The vertical gray lines and the numbers represent the irreducible path (see Figure 4.3). A) Laser power, corresponding spring constant: $P = 0W$, $k_1/k_0 = 0$ (free crystal), B) $P = 1.2W$, $k_1/k_0 = 1$ and C) $P = 2.75W$, $k_1/k_0 = 2.5$.

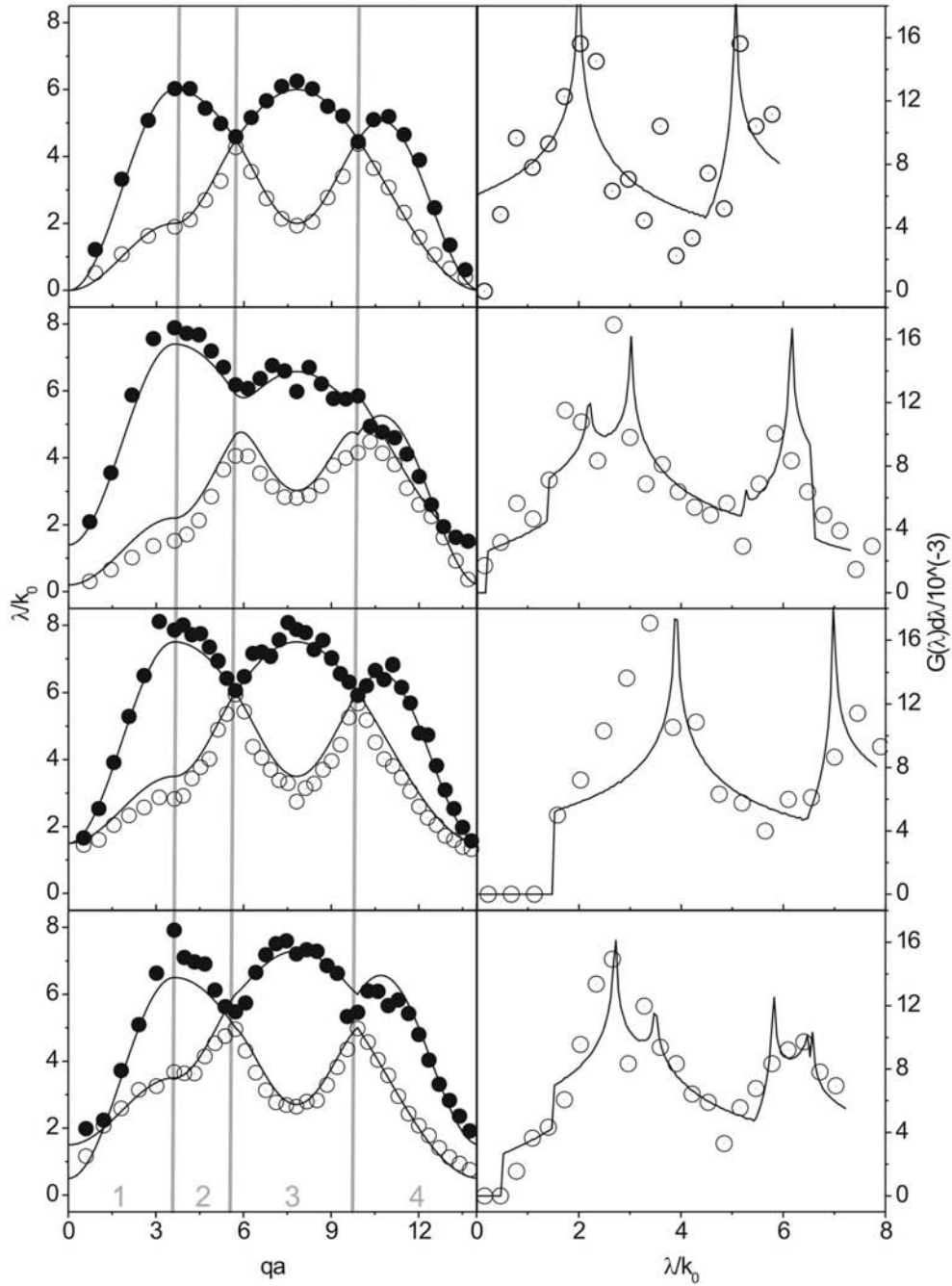


FIGURE 4.8. Case e: band-structure λ (left column) and spectrum $G(\lambda)$ (right column) determined experimentally for different laser powers (symbols). A) $(P_1, P_2) = (0W, 0W)$, B) $(3W, 0.5W)$, C) $(2W, 1.5W)$ and D) $(0.5W, 1.5W)$. The corresponding spring constants are A) $(k_1/k_0, k_2/k_0) = (0, 0)$, B) $(1.4, 0.2)$, C) $(1.5, 1.5)$ and D) $(0.5, 1.5)$. The spring constants are represented by numerical curves plotted as black solid lines.

highlight the symmetry-breaking caused by the substrate, we plotted 2D contour graphs of the band-structure for case e (see Figure 4.9). The upper row depicts the lower (left

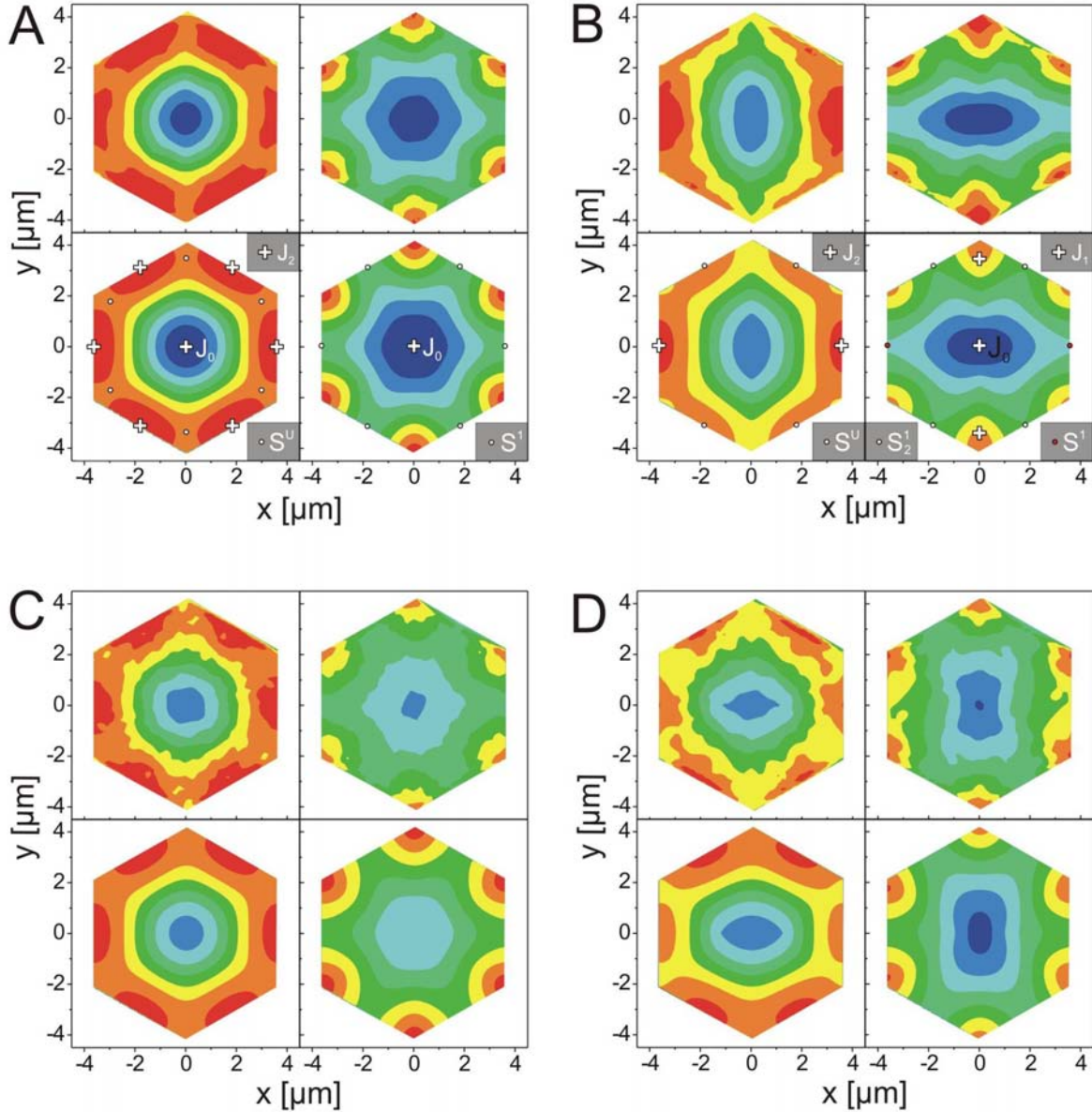


FIGURE 4.9. Case e: Contour plots of the 2D band-structure in the first BZ. In Figure A-D, the left (right) column refers to the lower (upper) band, and the upper (lower) row corresponds to measured (calculated) data. The color code contains 8 steps from zero to the maximum value of λ : dark blue, blue, light-blue, light-green, green, yellow, orange, red. The parameters are A) $(k_1/k_0, k_2/k_0) = (0, 0)$, B) $(1.4, 0.2)$, C) $(1.5, 1.5)$ and D) $(0.5, 1.5)$ (see Figure 4.8). In Figure A and B, the logarithmic and jump singularities are indicated (see Figure 4.6).

plot) and upper band (right plot) determined experimentally and the lower row shows the corresponding theoretical bands. This visualization clearly reveals the reduction of the 6-fold symmetry of the free crystal (Figure A) to a 2-fold one in Figure B where

$k_1 > k_2$. In Figure C where $k_1 = k_2$ the intrinsic 6-fold symmetry is restored and finally broken again in Figure D ($k_1 < k_2$).

4.6. RELEVANCE OF THE RESULTS FOR ATOMIC CRYSTALS

We now discuss the repercussions of our results on atomic crystals. Recall that phonons propagate and oscillate in atomic crystals (see box on page 47); we can therefore discuss in terms of the phonon-dispersion relation $\omega_{\mathbf{m}j} = \sqrt{\lambda_{\mathbf{m}j}/M}$. In the following, we write $\omega_{\mathbf{m}j}$ as $\omega_j(\mathbf{q})$ and, for a single j , $\omega_j(\mathbf{q})$ will be referred to as a branch of the phonon-dispersion relation.

First, we focus on the shift of branches caused by a substrate potential. The shift gives rise to $\omega_j(\mathbf{q}) > 0$ for $\mathbf{q} = \mathbf{0}$. According to the terminology of solid state physics, a substrate can therefore transfer an acoustical branch into an optical one; here all particles are oscillating similarly for $\mathbf{q} = \mathbf{0}$. This collective oscillation leads to a macroscopic oscillating dipole moment provided that the interaction between the crystal and the substrate leads to an electrical polarization of the particles. Consequently, the intrinsically free crystal is enabled by the substrate to absorb electromagnetic radiation.

In addition to a shift of branches, we also verified that branches can be deformed by the substrate. This is reflected in a change of the gradient $\nabla_{\mathbf{q}}\omega_j(\mathbf{q})$ which is the group velocity $\mathbf{v}_j(\mathbf{q})$ of phonons with wave vectors in a range $[\mathbf{q}, \mathbf{q} + d\mathbf{q}]$,

$$\mathbf{v}_j(\mathbf{q}) = \nabla_{\mathbf{q}'}\omega(\mathbf{q}')\Big|_{\mathbf{q}'=\mathbf{q}}. \quad (4.56)$$

In other words, the group velocity can be tuned by the substrate – in flat branch sections the group velocity even vanishes, $\mathbf{v}_j(\mathbf{q}) = \mathbf{0}$. As we have demonstrated, this can be achieved by substrate potentials of certain geometry and orientation (for instance, section 7 (2) of the irreducible path for the cases a and e (f), see Figure 4.5). The possibility of tuning the phonon group velocity influences an important thermal property of condensed matter, namely the heat conductivity. The density of heat flux \mathbf{Q} is defined as

$$\mathbf{Q} = -\lambda\nabla_{\mathbf{r}}T \quad (4.57)$$

with λ the coefficient of heat conductivity. For small temperature gradients $\nabla_{\mathbf{r}}T$, the phononic contribution to (4.57) becomes

$$\mathbf{Q} = \frac{1}{V} \sum_{\mathbf{q},j} \frac{k_B T}{2} \mathbf{v}_j(\mathbf{q}) \quad (4.58)$$

with V the volume of the solid and $k_B T/2$ the energy that is transported by a single phonon in the classical regime. Of course, there is no heat transport in thermal equilibrium because of $\mathbf{v}_j(\mathbf{q}) = -\mathbf{v}_j(-\mathbf{q})$; however, in the presence of small temperature gradients, the heat $k_B T/2$ transported by a single phonon is slightly smaller in the direction of the gradient than in the opposite direction. In conclusion, the heat transport

of a solid can be raised or lowered if the group velocity is increased or decreased by means of a substrate potential.

The heat conductivity \mathbf{Q} is a non-equilibrium quantity. In the following, we explore the idea if equilibrium properties, such as the specific heat, can be influenced by a substrate as well. It is well known that the specific heat $C_V(T)$ is the first derivative of the internal energy $U(T)$ with respect to the temperature,

$$C_V = \frac{\partial}{\partial T} U(T) \quad (4.59)$$

with

$$U(T) = \int_0^\infty d\omega Z(\omega) \epsilon(\omega, T) d\omega. \quad (4.60)$$

$Z(\omega)$ denotes the phonon spectrum in terms of ω and is defined analogously to $G(\lambda)$ (4.54),

$$Z(\omega) := \sum_{\mathbf{q}, j} \delta(\omega - \omega(\mathbf{q})), \quad \int_0^\infty d\omega Z(\omega) = 2N. \quad (4.61)$$

$\epsilon(\omega, T)$ is the energy of a phonon with frequency ω . In the classical regime, each phonon mode has an average thermal energy $\epsilon(\omega, T) = k_B T/2$ according to the equipartition theorem. Hence,

$$U(T) = \int_0^\infty d\omega Z(\omega) \frac{k_B T}{2} \implies C_V = \frac{f}{2} N k_B, \quad (4.62)$$

whereas $f = 2$ refers to the number of degrees of freedom. Clearly, we obtain a result well known for the ideal gas and which depends only on the number of particles times f . Therefore, we cannot vary the specific heat by means of a substrate. Intuitively, we can interpret this result as follows: the oscillation amplitude u of the particles is decreased by a substrate which leads to an increase of the oscillation frequency ω ; the energy $M\omega^2 u^2/2$ is therefore kept constant at $k_B T/2$. As a consequence, the internal energy is not changed.

Of course, the classical description of solids is an approximate one and an accurate discussion can only be given with quantum mechanics. As can be shown, the phonon-dispersion relation $\omega_j(\mathbf{q})$ is not changed when going from the classical to the quantum mechanical regime by means of second quantization [67]. However, phonons are no longer classical harmonic oscillators with each having the average energy $k_B T/2$; instead, phonons now represent non-interacting quantum-mechanical oscillators which have quantized energies $\hbar\omega$. In thermal equilibrium, the number of phonons n with an energy $\hbar\omega$ is governed by Bose statistics

$$n = \frac{1}{\exp\left(\frac{\hbar\omega}{k_B T}\right) - 1}. \quad (4.63)$$

Consequently, the energy $\epsilon(\omega, T)$ of a mode ω is now given by

$$\epsilon(\omega, T) = \hbar\omega \left(\frac{1}{2} + \frac{1}{\exp\left(\frac{\hbar\omega}{k_B T}\right) - 1} \right), \quad (4.64)$$

where we have added the vacuum energy $\hbar\omega/2$ of the harmonic oscillator. Concerning the internal energy and the specific heat (4.60), the situation becomes significantly different compared to the classical regime. $\epsilon(\omega, T)$ now depends on ω and thus, the specific heat can be modified by substrates. In general, a completely new aspect is uncovered in the quantum mechanical regime. A substrate potential allows one to freeze out phonon modes ω because the number of phonons occupying the modes ω can be varied according to (4.63).

As a final remark, we mention that there are additional interesting properties of solids to discuss here, including thermal expansion and elasticity. In both cases the lattice sites are displaced themselves which leads to a mismatch between the crystal and the underlying substrate of fixed geometry; the discussion of thermal expansion or elasticity would therefore go beyond the scope of our studies presented here.

4.7. SUMMARY AND CONCLUSIONS

We numerically and experimentally studied the influence of commensurate substrates on the phonon-band structure of 2D crystals. The numerical studies were based on the harmonic approximation of the total energy from which we determined the phonon-band structure. We considered different substrates with modulations in one and two directions. In our experimental approach, we prepared a 2D crystal which consisted of charge-stabilized colloidal particles subjected to a light-induced substrate potential created by interfering laser-beams. From the recorded particle trajectories we determined the phonon-band structure.

Our theoretical results clearly reveal that, depending on the substrate, at least one branch of the band structure could be shifted and deformed. In addition, the calculated 2D band structures demonstrate how the intrinsic six-fold symmetry of the free crystal dispersion relation is reduced to the two-fold symmetry of the substrate. The measured band structures clearly verify the theoretical results. This shows that phonon-band structures (and thus phonon-dispersion relations) can indeed be tuned by substrate potentials.

In addition, we have discussed the repercussions of our results on atomic crystals. First, the shift of bands transfers acoustical into optical modes; solids are therefore enabled to absorb electromagnetic radiation depending on the nature of the particle-substrate interaction. Second, the deformation of bands leads to a change of the group velocity which affects the heat conductivity. In contrast, the specific heat cannot be

influenced by a substrate classically but instead can be tuned in the quantum mechanical regime.

Future research will focus on 3D calculations to explore whether incorporation of additional springs into bulk solids allows creation of phononic band gaps, i.e. phononic crystals [62]. The experimental challenge is to discover or to design solid materials where an anisotropic particle interaction allows realization of the model substrates considered in our theoretical studies.

A topic left unstudied relates to phonon dynamics, i.e. the temporal evolution of phonons. So far, we have performed theoretical work which is presented and discussed separately in the Appendix 4.8. Our experimental work focuses on an improved determination of lattice sites. This is necessary for the investigation of phonon dynamics and is discussed in the Appendix 4.9.

4.8. APPENDIX: PHONON DYNAMICS

Our studies on phonon-dynamics are based on the Langevin equation

$$M \frac{\partial^2}{\partial t^2} u_{\mathbf{n}\alpha}(t) = -\gamma \frac{\partial}{\partial t} u_{\mathbf{n}\alpha}(t) - \frac{\partial}{\partial u_{\mathbf{n}\alpha}(t)} V(\mathbf{u}(t)) + f_{\mathbf{n}\alpha}(t), \quad (4.65)$$

with M the mass of a particle, γ the coefficient of friction, $\mathbf{n} = (n_1, n_2)$ according to (4.5) and $\alpha \in \{x, y\}^1$. The $f_{\mathbf{n}\alpha}(t)$ are white noise,

$$\langle f_{\mathbf{n}\alpha}(t) \rangle = 0, \quad \langle f_{\mathbf{n}\alpha}(t) f_{\mathbf{n}'\alpha'}(t + \tau) \rangle = \epsilon \delta_{\mathbf{nn}'} \delta_{\alpha\alpha'} \delta(\tau), \quad (4.66)$$

where ϵ denotes a constant determined later and $\langle \dots \rangle$ refers to the ensemble average. In the following, we consider colloidal particles whose motion is overdamped [66]; the inertia term on the left hand side of (4.66) can therefore be neglected. Using (4.8) it follows that

$$\gamma \frac{\partial}{\partial t} u_{\mathbf{n}\alpha}(t) - f_{\mathbf{n}\alpha}(t) + \sum_{\mathbf{n}', \beta} \Phi_{\mathbf{nn}'\alpha\beta} u_{\mathbf{n}'\beta}(t), \quad (4.67)$$

To evaluate the Fourier transform of (4.67), we introduce the counterpart of $u_{\mathbf{n}\alpha}(t)$ (see (4.18) and (4.24)),

$$f_{\mathbf{n}\alpha}(t) = \frac{1}{\sqrt{N}} \sum_{\mathbf{m}, j} F_{\mathbf{m}j}(t) e_{\mathbf{m}j\alpha} \exp(i\mathbf{q}_m \mathbf{R}_n). \quad (4.68)$$

Using the fundamental properties of eigenvectors,

$$\sum_{\alpha} e_{\mathbf{m}j\alpha}^* e_{\mathbf{m}j'\alpha} = \delta_{jj'}, \quad \sum_j e_{\mathbf{m}j\alpha}^* e_{\mathbf{m}j\alpha'} = \delta_{\alpha\alpha'}, \quad (4.69)$$

and (4.21), it can be shown that

$$\langle F_{\mathbf{m}j}(t) \rangle = 0, \quad \langle F_{\mathbf{m}j}(t) F_{\mathbf{m}'j'}(t + \tau) \rangle = \epsilon \delta(\tau) \delta_{\mathbf{mm}'} \delta_{jj'}. \quad (4.70)$$

¹A more simplified dynamical description of colloidal crystals is given in [68].

We can now determine the Fourier transform of (4.67),

$$\sum_{\mathbf{m},j} \left[\left\{ \gamma \frac{\partial}{\partial t} Q_{\mathbf{m}j}(t) - F_{\mathbf{m}j}(t) \right\} e_{\mathbf{m}j\alpha} \exp(i\mathbf{q}_{\mathbf{m}}\mathbf{R}_{\mathbf{n}}) + Q_{\mathbf{m}j}(t) \sum_{\beta} e_{\mathbf{m}j\beta} \sum_{\mathbf{n}'} \Phi_{\mathbf{n}\mathbf{n}'\alpha\beta} \exp(i\mathbf{q}_{\mathbf{m}}\mathbf{R}_{\mathbf{n}'}) \right] = 0. \quad (4.71)$$

Inserting the eigenvalue equation (4.23) and $1 = \exp(i\mathbf{q}_{\mathbf{m}}\mathbf{R}_{\mathbf{n}}) \exp(-i\mathbf{q}_{\mathbf{m}}\mathbf{R}_{\mathbf{n}})$ we find

$$\sum_{\mathbf{m},j} \left\{ \gamma \frac{\partial}{\partial t} Q_{\mathbf{m}j}(t) - F_{\mathbf{m}j}(t) + \lambda_{\mathbf{m}j} Q_{\mathbf{m}j}(t) \right\} e_{\mathbf{m}j\alpha} \exp(i\mathbf{q}_{\mathbf{m}}\mathbf{R}_{\mathbf{n}}) = 0. \quad (4.72)$$

From this relation we conclude that

$$\gamma \frac{\partial}{\partial t} Q_{\mathbf{m}j}(t) - F_{\mathbf{m}j}(t) + \lambda_{\mathbf{m}j} Q_{\mathbf{m}j}(t) = 0 \quad (4.73)$$

because the $e_{\mathbf{m}j}$ and $\exp(i\mathbf{q}_{\mathbf{m}}\mathbf{R}_{\mathbf{n}})$ form a complete set of basic vectors and functions.

The Langevin equation in the $(\mathbf{m}j)$ -representation (4.73) has the formal solution,

$$Q_{\mathbf{m}j}(t) = Q_{\mathbf{m}j}^{(0)} \exp\left(-\frac{\lambda_{\mathbf{m}j}}{\gamma} t\right) + \frac{1}{\gamma} \exp\left(-\frac{\lambda_{\mathbf{m}j}}{\gamma} t\right) \int_0^t dt' \exp\left(\frac{\lambda_{\mathbf{m}j}}{\gamma} t'\right) F_{\mathbf{m}j}(t'). \quad (4.74)$$

Using this solution and (4.70) we can calculate the phonon autocorrelation function,

$$\begin{aligned} \langle Q_{\mathbf{m}j}(t+\tau) Q_{\mathbf{m}j}^*(t) \rangle &= \left\langle \left\{ |Q_{\mathbf{m}j}^{(0)}|^2 - \frac{\epsilon}{2\lambda_{\mathbf{m}j}\gamma} \right\} \exp\left(-\frac{\lambda_{\mathbf{m}j}}{\gamma}(2t+\tau)\right) \right. \\ &\quad \left. + \frac{\epsilon}{2\lambda_{\mathbf{m}j}\gamma} \exp\left(-\frac{\lambda_{\mathbf{m}j}}{\gamma}\tau\right) \right\rangle. \end{aligned} \quad (4.75)$$

Applying the equipartition theorem for $\tau = 0$ and $t \rightarrow \infty$ allows evaluation of ϵ ,

$$\epsilon = 2\gamma k_B T. \quad (4.76)$$

In thermal equilibrium, the ergodic hypothesis states that the ensemble average equals the temporal one, $\langle \dots \rangle \leftrightarrow \lim_{T \rightarrow \infty} T^{-1} \int_0^T dt$. Hence, it follows that

$$\langle Q_{\mathbf{m}j}(t+\tau) Q_{\mathbf{m}j}^*(t) \rangle = \frac{k_B T}{\lambda_{\mathbf{m}j}} \exp\left(-\frac{\tau}{T_{\mathbf{m}j}}\right) \quad (4.77)$$

with $T_{\mathbf{m}j}$ the decay time of the phonon $Q_{\mathbf{m}j}(t)$,

$$T_{\mathbf{m}j} = \frac{\gamma}{\lambda_{\mathbf{m}j}}. \quad (4.78)$$

Accordingly, the phonons $Q_{\mathbf{m}j}(t)$ decay with a characteristic time $T_{\mathbf{m}j}$ inversely proportional to the corresponding eigenvalues $\lambda_{\mathbf{m}j}$. Equation (4.78) constitutes the phonon-dispersion relation in the overdamped limit [68] relating decay times to wave vectors.

In the overdamped limit, the particles do not oscillate and hence, the frequencies $\omega_{\mathbf{m}j}$ are not defined.

The phonon autocorrelation functions (4.77) can be related to the mean-square displacement (MSD),

$$\begin{aligned}\delta_{MSD}(\tau) &= \frac{1}{N} \sum_{\mathbf{n}} \langle |\mathbf{r}_{\mathbf{n}}(t+\tau) - \mathbf{r}_{\mathbf{n}}(t)|^2 \rangle \\ &= \frac{1}{N} \sum_{\mathbf{n}} \langle |\mathbf{u}_{\mathbf{n}}(t+\tau) - \mathbf{u}_{\mathbf{n}}(t)|^2 \rangle \\ &= 2(c(0) - c(\tau))\end{aligned}\tag{4.79}$$

with

$$\begin{aligned}c(\tau) &:= \frac{1}{N} \sum_{\mathbf{n},\alpha} \langle u_{\mathbf{n}\alpha}(t+\tau)u_{\mathbf{n}\alpha}(t) \rangle \\ &= \frac{1}{N} \sum_{\mathbf{m},j} \langle Q_{\mathbf{m}j}(t+\tau)Q_{\mathbf{m}j}(t) \rangle.\end{aligned}\tag{4.80}$$

Using the result (4.77) and the phonon spectrum (4.54) it follows that

$$\begin{aligned}c(\tau) &= \frac{1}{N} \sum_{\mathbf{m},j} \frac{k_B T}{\lambda_{\mathbf{m}j}} \exp\left(-\frac{\lambda_{\mathbf{m}j}}{\gamma}\tau\right) \\ &= 2 \int d\lambda \frac{1}{2N} \sum_{\mathbf{m},j} \delta(\lambda - \lambda_{\mathbf{m}j}) \frac{k_B T}{\lambda} \exp\left(-\frac{\lambda}{\gamma}\tau\right) \\ &= 2 \int d\lambda k_B T \frac{G(\lambda)}{\lambda} \exp\left(-\frac{\lambda}{\gamma}\tau\right).\end{aligned}\tag{4.81}$$

Consequently, $c(\tau)$ can be understood as the Laplace transform of $G(\lambda)/\lambda$. Expressing (4.81) in reduced quantities, $\tau' = \tau k_0/\gamma$ and $\lambda' = \lambda/k_0$, yields

$$\frac{k_0 c(\tau')}{k_B T} = 2 \int d\lambda' \frac{G(\lambda')}{\lambda'} \exp(-\lambda' \tau').\tag{4.82}$$

We evaluated the mean-square displacement $\delta_{MSD}(\tau)$ according to (4.82) for case e (see Figure 4.3). The parameters of the substrate potential ($k_1/k_0, k_2/k_0$) were chosen the same as in Figure 4.6. As shown in Figure 4.10A the MSD increases slower, the stronger the substrate. In addition, we observe a logarithmic divergence for case a to c where only one substrate (k_1) is present; in contrast, the MSD saturates if a 2D substrate is present (case d-f). The spectra shown in Figure 4.6 reveal that $\lim_{\lambda' \rightarrow 0} G(\lambda') > 0$ in the last and $\lim_{\lambda' \rightarrow 0} G(\lambda') = 0$ in the first three cases. According to (4.82) the latter must lead to a logarithmic divergence of the MSD, $\delta_{MSD}(\infty) := \lim_{\tau' \rightarrow \infty} \delta(\tau') = \lim_{\tau' \rightarrow 0} c(\tau') \rightarrow \infty$. In addition, we have studied the dependence of $\delta_{MSD}(\infty)$ on the strength k_1 ($k_2 = 4k_0$ fixed) of the substrate potential for the six cases defined in Figure 4.3. The results are presented in Figure 4.10B. Clearly,

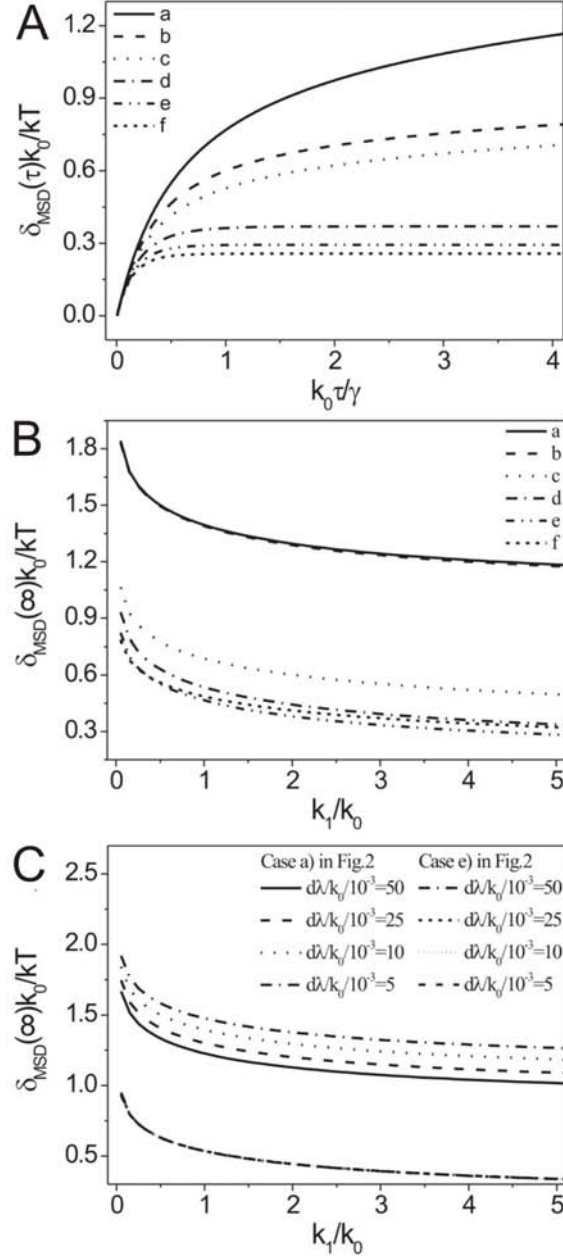


FIGURE 4.10. A) Mean-square displacement (MSD) $\delta_{MSD}(\tau)$ for the six cases considered in Figure 4.6A-F. B) Limit of the MSD $\delta_{MSD}(\tau)$ for $\tau \rightarrow \infty$ versus strength k_1 of the substrate potential. Here, the six cases are specified in Figure 4.3A-F. In the cases c-f, k_2 is set to $4k_0$. Figure C shows for case a and e in Figure 4.3 the dependence of $\delta_{MSD}(\infty)$ on the bin size $d\lambda$ of the phonon spectrum $G(\lambda)$. Four bin sizes were considered for each case (see plot legend for details).

$\delta_{MSD}(\infty)$ decreases with increasing strength k_1 . This simply reflects that particle diffusion is increasingly hindered by the substrate; therefore, $\delta_{MSD}(\infty)$ drops considerably if the second potential is present. For $k_1/k_0 \rightarrow 0$, $\delta_{MSD}(\infty)$ again diverges if only a single

substrate k_1 is present. A second substrate k_2 is required to shift the jump singularity of $G(\lambda')$ away from $\lambda' = 0$.

The logarithmic divergence of $\delta_{MSD}(\tau)$ arises from the well-known effect [69–71] that long-wavelength fluctuations in 2D crystals lead to instability. As a consequence of this, 2D crystals exhibit no true long-range order, but rather a quasi-long range order characterized by an algebraic decay of the translational correlation function [72]. As has already been mentioned, Figure 4.10, in essence, demonstrates that a substrate with modulations in two directions is required to cure the instability because, in this case, only the substrate can shift the jump-singularity of $G(\lambda')$ away from $\lambda' = 0$. It is also important to mention that k_1 and k_2 are not required to exceed a threshold value to achieve $\lim_{\lambda' \rightarrow 0} G(\lambda') = 0$. It is sufficient to demand $k_1 > 0$ and $k_2 > 0$ to keep $\delta_{MSD}(\infty)$ on a finite value.

We close this discussion on phonon dynamics with a remark about the dimensionality. In contrast to their 2D counterpart, 3D crystals do not suffer from instabilities. Our studies are not restricted to 2D and can be extended to 3D straightforwardly. Therefore, it does not become immediately clear where the difference between 2D and 3D arises. We recall the expression (4.81) and take the limit $N \rightarrow \infty$, $N^{-1} \sum_{\mathbf{m}} \rightarrow V/(2\pi)^d \int d\mathbf{q}^d$ with V the volume of the elementary cell of the crystal (for instance, $V = \sqrt{3}/2a^2$ in the case of a 2D hexagonal crystal) and d the dimensionality,

$$c(\tau) = \frac{V}{(2\pi)^d} \sum_j \int_{1.BZ} d\mathbf{q}^3 \frac{k_B T}{\lambda_j(\mathbf{q})} \exp\left(-\frac{\lambda_j(\mathbf{q})}{\gamma} \tau\right). \quad (4.83)$$

It can be shown that in 2D and 3D $\lambda(\mathbf{q}) \propto |\mathbf{q}|^2$ for $\mathbf{q} \rightarrow \mathbf{0}$. In 3D the volume of the reciprocal space, or the number of states \mathbf{q} , grows with q^2 while in 2D the volume only increases linearly with q . Hence, the singularity $\lim_{\mathbf{q} \rightarrow \mathbf{0}} (\lambda(\mathbf{q}))^{-1} \rightarrow \infty$ is integrable in 3D while this is not true in 2D. Intuitively, one might therefore think the singularity at $\mathbf{q} = \mathbf{0}$ to be less pronounced because the central point $\mathbf{q} = \mathbf{0}$ is surrounded by a significantly higher number of finite states in 3D than in 2D. We can translate this idea to configurational space where the lattice sites are not stable in 2D because there is a lack of stabilizing neighboring sites.

4.9. APPENDIX: MEASUREMENT OF LATTICE SITES

So far, we have not been able to study phonon dynamics in experiments because of the determination of the lattice sites \mathbf{R}_n which is currently performed by temporal averaging according to (4.52). This temporal averaging is required due to the instability of 2D crystals (see Figure 4.10, logarithmic divergence of $\delta_{MSD}(\tau)$). In addition, an inhomogeneous temporal motion of the lattice sites is inevitably present in experiments, arising from drift of the translation stages and optical mounts used in the experimental setup. Hence, the measured lattice sites are time-dependent. We can correct for the

drift with a set of sites fluctuating around a constant value, $\mathbf{R}_n(t) = \mathbf{R}_n + \Delta\mathbf{R}(t)$. As such, $\Delta\mathbf{R}(t)$ depends on the time window Δt chosen to perform temporal averaging. $\Delta\mathbf{R}(t)$ is identical for all sites because the drift of the experimental setup similarly affects all the particles. As a consequence, the Fourier transform of the displacement (4.17) exhibits a time dependence in the exponential,

$$\tilde{u}_{m\alpha}(t) = \frac{1}{\sqrt{N}} \exp(i\mathbf{q}_m \Delta\mathbf{R}(t)) \sum_{\mathbf{n}} (u_{n\alpha}(t) - \Delta R_\alpha(t)) \exp(-i\mathbf{q}_m \mathbf{R}_n) \quad (4.84)$$

with $u_{n\alpha}(t)$ the true value of the displacement. Hence, the dynamical matrix determined according to (4.32) becomes

$$\begin{aligned} \tilde{D}_{m\alpha\beta} &= \langle \tilde{u}_{m\alpha}^*(t) \tilde{u}_{m\beta}(t) \rangle_t \\ &\quad - \delta_{m\mathbf{0}} \left\{ \langle \Delta R_\alpha(t) \tilde{u}_{m\beta}(t) + \tilde{u}_{m\alpha}^*(t) \Delta R_\beta(t) + N \Delta R_\alpha(t) \Delta R_\beta(t) \rangle_t \right\}, \end{aligned} \quad (4.85)$$

where we used (4.20). Of course, (4.85) is an approximation because the number of lattice sites N considered in the experiments is finite. However, we see that only in the case of $\mathbf{q} = \mathbf{0}$ is the dynamical matrix considerably affected by the drift $\Delta\mathbf{R}(t)$. Indeed, the dynamical matrices we evaluated from measured trajectories were not sensitive to the choice of the time window Δt and hence $\Delta\mathbf{R}(t)$.

Unfortunately, the studies on phonon dynamics do not behave insensitively. The reason is that the phase factor $\exp(i\mathbf{q}_m \Delta\mathbf{R}(t))$ does not cancel when calculating the phonon autocorrelation function (4.77),

$$\begin{aligned} &\langle Q_{m_j}(t + \tau) Q_{m_j}^*(t) \rangle \\ &\quad \approx \left\langle \exp(i\mathbf{q}_m [\Delta\mathbf{R}(t) - \Delta\mathbf{R}(t + \tau)]) \mathbf{e}_j^* \tilde{u}_{m_j}(t + \tau) \tilde{u}_{m_j}^*(t) \mathbf{e}_j \right\rangle_t. \end{aligned} \quad (4.86)$$

As a result, we must improve the determination of the lattice sites. To do so, we have written a computer program which fits polynomials to the trajectories,

$$\mathbf{P}_n(t) = \sum_{i=0}^p a_i t^i. \quad (4.87)$$

This approach does not depend on a time window Δt . In terms of $\mathbf{P}_n(t)$, we define the constant lattice site and the displacement as

$$\mathbf{R}_n := \mathbf{P}_n(0) \text{ and } \mathbf{u}_n(t) := \mathbf{r}_n(t) - \mathbf{P}_n(t), \quad (4.88)$$

respectively. The degree of the polynomial p is increased until the histogram of the displacements $H_\alpha(u_\alpha)$ ($\alpha = x, y$) becomes symmetric around the lattice sites. We check for the symmetry of H_α by fitting Gaussians,

$$H_\alpha(u_\alpha) = A \exp\left(-\frac{u_\alpha^2}{w^2}\right), \quad A, w = \text{const.} \quad (4.89)$$

Using this procedure, we intent to account for asymmetric, inhomogeneous drifts as accurately as possible and, at the same time, to lose less information about lattice

vibrations. For very asymmetric and inhomogeneous drifts we intend to apply the fitting procedure piecewise, and we cut the trajectories into temporal sections.

5

Structural crossover in binary hard sphere mixtures

ABSTRACT

Using confocal microscopy we investigate the structure of binary mixtures of colloidal hard spheres with size ratio $q = 0.61$. As a function of the packing fraction of the two particle species, we observe a marked change of the dominant wavelength in the pair correlation function. This behavior is in excellent agreement with a recently predicted structural crossover in such mixtures. In addition, the repercussions of structural crossover on the real-space structure of a binary fluid are analyzed. We suggest a relation between crossover and the lateral extension of networks containing only equally-sized particles that are connected by nearest neighbor bonds. This is supported by Monte-Carlo simulations which are performed at different packing fractions and size ratios.

5.1. INTRODUCTION

Most systems in nature and technology are mixtures of differently-sized particles. Each distinct particle size introduces another length scale giving rise to an exceedingly rich phenomenology in comparison with single-component systems. Even the simplest conceivable multi-component system, a binary mixture of hard spheres, exhibits interesting and complex behavior. Just a few examples include entropy-driven formation of binary crystals [73–75], frustrated crystal growth [19], the Brazil nut effect [76], glass-formation [77, 78] and entropic selectivity in external fields [79]. Although interaction potentials in atomic systems are more complex than those of hard spheres, the principle of volume exclusion is ubiquitous and thus always dominates the short-range order in liquids [80]. Accordingly, hard spheres form one of the most important and successful model systems in describing fundamental properties of fluids and solids. It has been demonstrated that many of their features can be directly transferred to atomic systems where fundamental mechanisms are often obstructed by additional material specific effects [81]. Binary hard sphere systems are fully characterized by their size ratio $q = \sigma_s/\sigma_b$ with σ_i the diameters of the small (s) and big (b) spheres and the small and big sphere particle number N_s, N_b , respectively.

A central measure of structure in fluids are the pair correlation functions $h_{ij}(r)$, which describes the probability of finding a particle of size i at a distance r from another particle of size j . It has been shown that all pair-correlation functions in any fluid mixture with short-ranged interactions (not just hard spheres) exhibit the same type of asymptotic decay, which can be either a purely (monotonic) exponential or an exponentially-damped oscillatory - see [82] and references therein. This prediction, which is valid in all dimensions, suggests that all pair-correlation functions decay with a common wavelength and decay length in the asymptotic limit. For binary hard-sphere mixtures where $N_b \gg N_s$ or $N_b \ll N_s$, this is rather obvious since the system is dominated by either big or small particles. The pair-correlation functions will asymptotically oscillate with a wavelength determined either by σ_b ($N_b \gg N_s$) or σ_s ($N_b \ll N_s$). Rather surprising is that the above statement is also valid for all other combinations of N_s and N_b where the system is not dominated by particles of a single size [82, 83]. Accordingly, in the asymptotic limit, the (N_s, N_b) -phase diagram is divided by a sharp crossover line where the decay lengths of the contributions to $h_{ij}(r)$ with the two wavelengths become identical. Below and above this line, however, the pair-correlation function is either determined by the diameter of the small spheres or that of the big spheres¹.

¹For very asymmetric size ratios, i.e., $q < 0.3$, there can be additional regions in which oscillations at intermediate wavelength can be observed.

Despite the generic character of structural crossover and the close relationship between structural and mechanical properties, this effect has not been observed in experiments as the asymptotic limit is difficult to reach in scattering experiments on atomic and molecular liquids. Recent calculations however suggest that structural crossover is already detectable at relatively small distances [83]. Because colloidal particles are directly accessible in real space, such systems provide an opportunity to explore the structure of binary fluids and to investigate structural crossover experimentally.

This chapter is organized as follows: After briefly summarizing the methods and results of theoretical research on structural crossover in Section 5.2 we present our experimental approach, data analysis and results in Section 5.3 and Section 5.4. Subsequently, we introduce a connectivity analysis in Section 5.5 to find out what are the repercussions of structural crossover on the real-space structure of a binary mixture. In Section 5.6 we finally apply the connectivity analysis for different q and total packing fractions η using Monte-Carlo simulation configurational data. Section 5.7 provides the conclusions and an outlook. The Appendix 5.8 is concerned about the limitations of our experimental method.

5.2. THEORETICAL APPROACH

This section provides a brief overview on the theoretical work of Grodon et al. [23, 82, 83] who determined the pair correlation functions of binary hard-sphere mixtures by means of density functional theory (DFT), the Ornstein-Zernike equation and leading-order asymptotics. A detailed description of DFT for a one-component fluid is given in [84]. The extension to a mixture is straightforward and the basic idea is as follows: A classical system of N particles in the grand canonical ensemble is characterized by the temperature T , the chemical potential μ and the volume V . The classical Hamiltonian is

$$H_N = \sum_{i=1}^N \frac{p_i^2}{2m} + U(\mathbf{r}_1, \dots, \mathbf{r}_2) + \sum_{i=1}^N V_{ext}(\mathbf{r}_i), \quad (5.1)$$

where \mathbf{r}_i and \mathbf{p}_i are the position and the momentum of particle i , respectively. U is the potential energy of the interactions between the particles and V_{ext} denotes an external potential. For this system the density functional

$$\Omega[\rho(\mathbf{r})] = \mathcal{F}[\rho(\mathbf{r})] + \int d\mathbf{r} \rho(\mathbf{r}) (V_{ext}(\mathbf{r}) - \mu) \quad (5.2)$$

can be introduced [84, 85] where $\mathcal{F}[\rho(\mathbf{r})]$ denotes the intrinsic Helmholtz free energy which can be split into a part $\mathcal{F}_{id}[\rho(\mathbf{r})]$ describing the ideal gas and a part $\mathcal{F}_{ex}[\rho(\mathbf{r})]$ including particle interactions. The equilibrium density $\rho_0(\mathbf{r})$ minimizes $\Omega[\rho(\mathbf{r})]$ which then equals the system's grand potential Ω . The subtlety of DFT is that $\mathcal{F}_{ex}[\rho(\mathbf{r})]$ is not known in advance and has to be constructed. An example is the Rosenfeld functional for the exact one-dimensional functional of hard-rod mixtures [86, 87]. Finally, the pair

correlation function $h(\mathbf{r}_1, \mathbf{r}_2)$ is determined by solving the Ornstein-Zernike equation (2.14) with the pair direct correlation function $c(\mathbf{r}_1, \mathbf{r}_2)$ derived from $\mathcal{F}_{ex}[\rho(\mathbf{r})]$ [84]:

$$c(\mathbf{r}_1, \mathbf{r}_2) = -\beta \frac{\delta^2 \mathcal{F}_{ex}[\rho(\mathbf{r})]}{\delta \rho(\mathbf{r}_2) \delta \rho(\mathbf{r}_1)} \quad (5.3)$$

In the case of a homogeneous and isotropic binary mixture of big and small particles with respective diameters σ_b and σ_s , the Ornstein-Zernike equation (2.15) generalizes to

$$h_{ij}(r_{12}) = c_{ij}(r_{12}) + \sum_{\lambda=B,S} \rho_\lambda \int d\mathbf{r}_3 c_{i\lambda}(r_{13}) h_{\lambda j}(r_{32}) \quad (5.4)$$

with $r_{ij} = |\mathbf{r}_i - \mathbf{r}_j|$ and ρ_λ being the density of particle species λ . The first of two important statements on the $h_{ij}(r)$ is part of the general theory of asymptotic decay [88]: in the asymptotic limit, $r \rightarrow \infty$, the pair correlation functions are completely determined once the pole structure of their Fourier transforms is known. Second, the Fourier transforms $\tilde{h}_{ij}(k)$ of all $h_{ij}(r)$ share the same denominator $D(k)$; consequently, all $h_{ij}(r)$ exhibit the same pole structure ($D(k) = 0$) and thus have a common asymptotic decay. The Fourier transforms $\tilde{h}_{ij}(k)$ can be evaluated via the residue theorem yielding

$$r h_{ij}(r) = \frac{1}{2\pi} \sum_n R_{ij}^{(n)} \exp(i a_1^{(n)} r) \exp(-a_0^{(n)} r) \quad (5.5)$$

with $p^{(n)} = a_1^{(n)} + i a_0^{(n)}$ being the coordinates of the poles ($D(p^{(n)}) = 0$) and $R_{ij}^{(n)} = \text{Res}(k \tilde{h}_{ij}(k))|_{k=p^{(n)}}$ being the residues. From (5.5) it becomes clear that the pole with the smallest imaginary part $a_0^{(n)}$ determines the behavior of the $h_{ij}(r)$ for $r \rightarrow \infty$ as has been stated above. This pole is termed the leading-order pole. In the following the poles will be denoted as π_n .

In addition to DFT calculations, Grodon et al. have determined the $h_{ij}(r)$ of a 3D binary hard-sphere mixture with $q = 0.5$ by solving the Ornstein-Zernike equation using the Percus-Yevick closure relation (2.17). Instead of the particle number N_i they used the packing fraction $\eta_i = N_i \pi \sigma_i^2 / (4S)$ with S the system volume to characterize the mixtures. The packing fraction of the big particles was fixed at $\eta_B = 0.1$ and the packing fraction of the small particles was increased starting at $\eta_s = 0.01$. The resulting pole trajectories in the (a_0, a_1) -plane are plotted in Figure 5.1A. For the starting value $\eta_s = 0.01$ the imaginary part $a_0^{(1)}$ of pole π_1 is the smallest and thus, π_1 is the leading-order pole with its real part $a_1^{(1)}$ determining the wavelength on which the $h_{ij}(r)$'s oscillate for $r \rightarrow \infty$. Upon increasing η_s the trajectories of π_1 and π_2 move in opposite directions. Consequently there is a transition (at $\eta_s = 0.126$) where the imaginary part $a_0^{(2)}$ becomes smallest and thus π_2 becomes the leading-order pole. This is accompanied by a strong increase of the real part a_1 by a factor of approximately q^{-1} indicated by the arrow in Figure 5.1A. The consequences of the change of the leading-order pole for the $h_{ij}(r)$ are shown in Figure 5.1B where $\ln |h_{bb}(r)|$ is plotted. Note that the wavelength of $h_{bb}(r)$ is doubled in this representation. Below the transition from π_1 to π_2 ($h_{bb} = 1$) the

$h_{bb}(r)$ oscillates on a wavelength slightly larger than the diameter σ_b of the big particles. In contrast, the $h_{bb}(r)$'s wavelength slightly exceeds the small diameter σ_s above the transition from π_1 to π_2 (h_{bb} 3). At the transition (h_{bb} 2), clear interference effects are visible because in this case both wavelengths contribute equally to the asymptotic behavior of the $h_{ij}(r)$. This sharp change in the leader-order pole and in the asymptotic oscillatory behavior of the pair correlation function is termed structural crossover. Note that the crossover behavior is observed for all combinations $(i, j) = (b, b)$, (b, s) , (s, b) and (s, s) since the $h_{ij}(r)$ all share the same decay length as mentioned above.

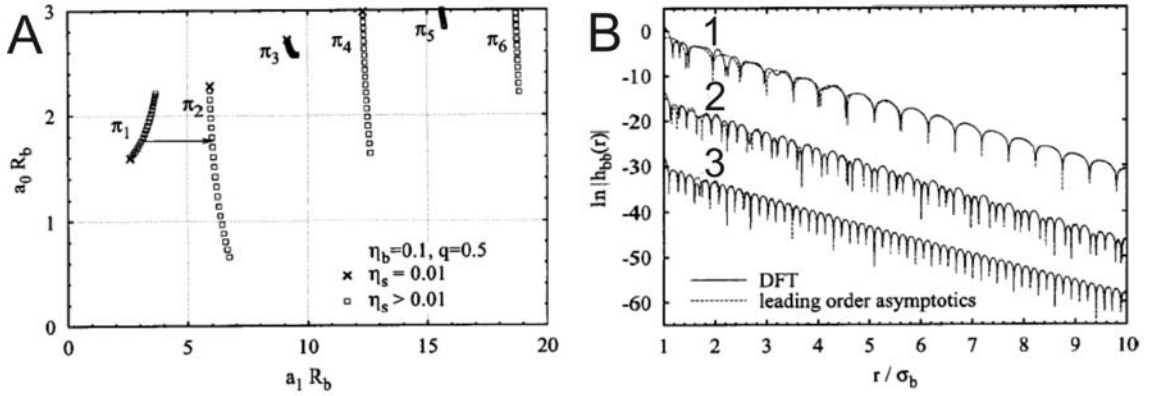


FIGURE 5.1. A) Imaginary (a_0) vs real (a_1) part of the poles π_1, π_2, \dots for a binary hard-sphere mixture with size ratio $q = 0.5$ obtained from Percus-Yevick theory. $R_{b,s}$ denotes the radius of the big and small particles, respectively. The packing fraction of the big particles is kept constant at $\eta_b = 0.1$ while the packing fraction of the small particles is raised (open squares) starting from the value $\eta_s = 0.01$ (crosses). The arrow indicates the crossover $\pi_1 \rightarrow \pi_2$ at $\eta_s = 0.126$. B) Plots of $\ln |h_{bb}(r)|$ for the size ratio $q = 0.3$ and fixed $\eta_b = 0.15$. Solid lines: DFT calculation based on the Rosenfeld functional. Dashed lines: Leading-order asymptotics. 1) $\eta_s = 0.15$, 2) $\eta_s = 0.2028$ (crossover value), 3) $\eta_s = 0.25$. The curves are shifted vertically for clarity. Plots copied from [82].

To find out whether structural crossover can be observed experimentally, Grodon et al. compared the Ornstein-Zernike results with calculations based on leading-order asymptotics (5.5). Figure 5.1B depicts the corresponding $h_{bb}(r)$ in logarithmic representation as solid and dashed lines, respectively. As can be seen the two approaches agree well for distances down to a couple of particle diameters. Additionally, Monte-Carlo (MC) simulations were performed which displayed structural crossover at intermediate distance as well [82, 83]. Structural crossover should be therefore accessible in experiments.

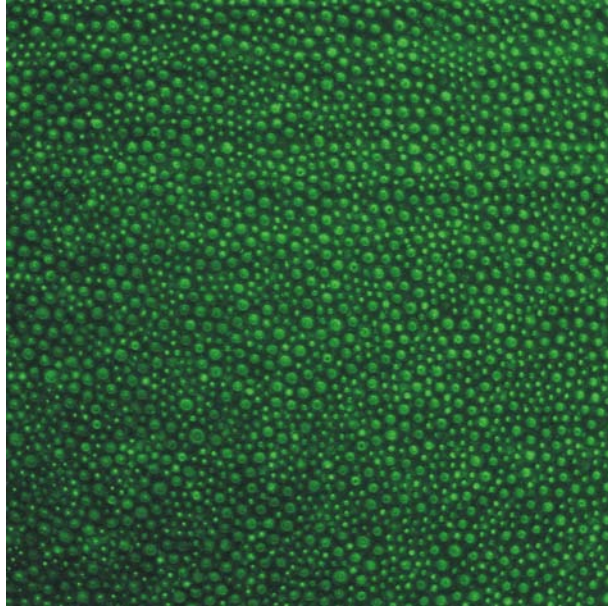


FIGURE 5.2. Image of a colloidal hard-sphere mixture recorded with confocal microscopy in reflection mode. The large (small) green spots correspond to the big (small) particles. The field of view is $187\mu\text{m} \times 187\mu\text{m}$.

5.3. EXPERIMENTAL METHOD AND DATA ANALYSIS

We use an aqueous binary colloidal mixture of large ($\sigma_b = 5.2\mu\text{m}$) polystyrene and small ($\sigma_s = 2.7\mu\text{m}$) melamin particles. It must be mentioned that we verified the

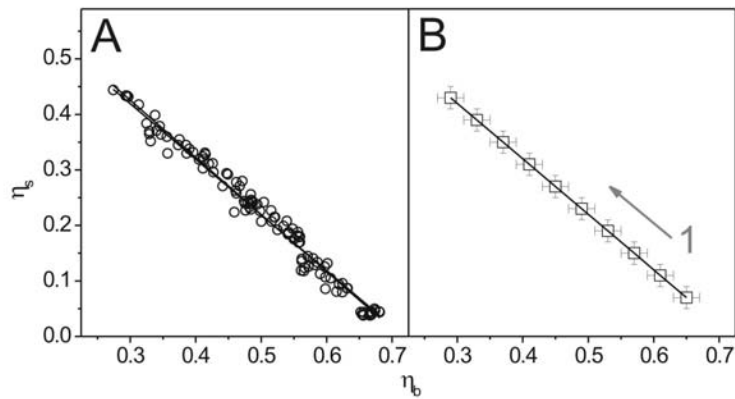


FIGURE 5.3. A) (η_s, η_b) -phase diagram determined from the confocal images. Experimental data are represented by the open symbols. The solid line is a fit to the data and corresponds to a total packing fraction of $\eta = 0.735$. B) Data shown in A) sorted into 10 equidistant bins (open symbols) along the linear fit. The error bars illustrate a bin size of $\Delta n = 0.04$. For convenience bins are labeled with sample numbers increasing in the direction indicated by the arrow.

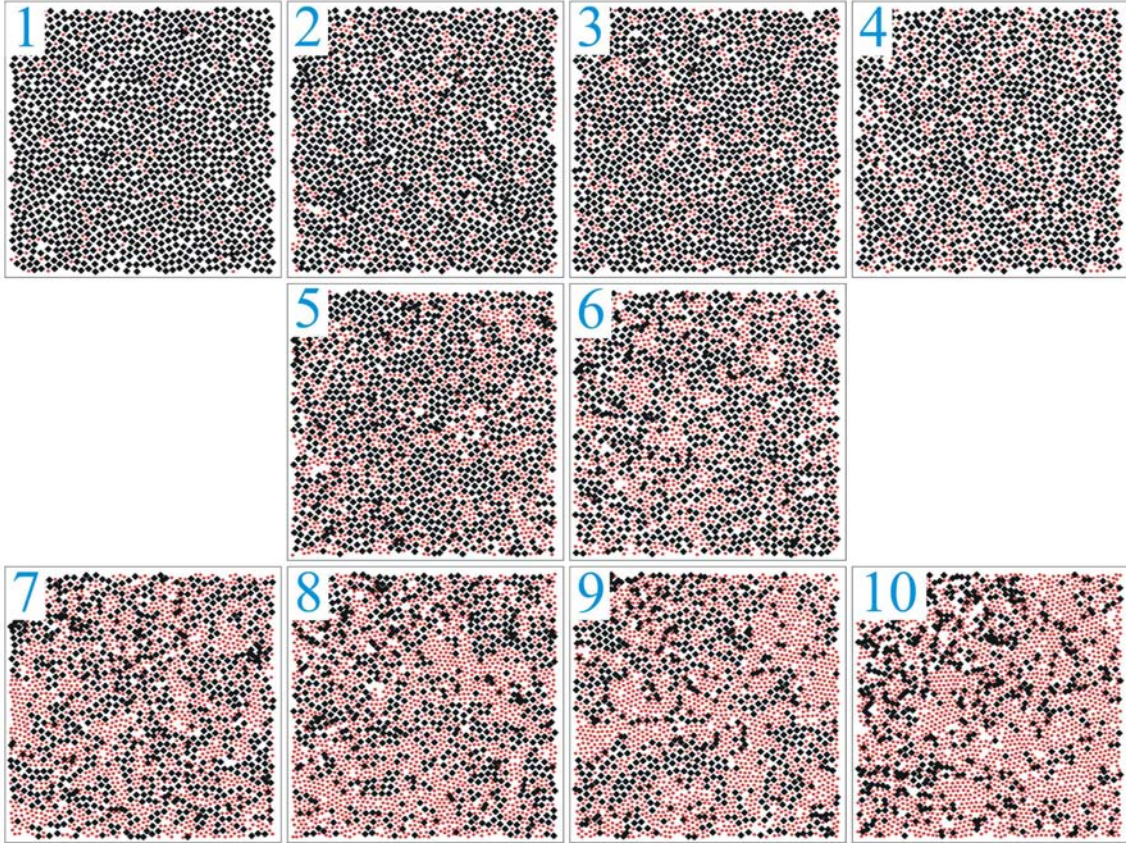


FIGURE 5.4. Snapshot for each sample number (see Figure 5.3B). The big and small particles are depicted as large black and small red spots, respectively.

particle diameters and observed deviations from the values provided by the supplying companies. For our check we prepared a dilute 2D sample of type II (see Section 3.5) for both the big and the small particles. We then confined two big or two small particles in a slightly defocused laser beam and determined the smallest distance between them. Finally we took into account the optical artifact described in Section 7.4 and obtained $\sigma_b = 4.8\mu m$ and $\sigma_s = 2.9\mu m$. The size ratio of our binary mixture thus is $q = 0.61$. As in the experiments presented in the previous chapters the particles interact via the screened Coulomb potential (2.10). To achieve an effective hard-sphere interaction we did not apply the deionization techniques presented in Section 3.5.

The sample cell consisted of a $2ml$ glass bottle from which the bottom plate was cut and subsequently glued onto a microscope slide. The latter allowed for optical imaging with an inverted confocal microscope (Leica TCS SP2, wavelength of laser: $488nm$) in reflection mode. Due to strong layering at the bottom wall we restrict ourselves to image only the first 2D bottom layer of the three-dimensional system. A typical snapshot is shown in Figure 5.2 where the field of view is square shaped and has a length of $L = 187\mu m$. To realize binary mixtures for different combinations of

packing fractions η_b , η_s we started with a sample consisting of big particles only and subsequently added small amounts of the small particle suspension. As a result, we obtain a homogeneous system in the 2D bottom layer where the total packing fraction $\eta = \eta_b + \eta_s$ remains constant. For each sample, we typically recorded 10-15 snapshots of the bottom layer at different lateral positions.

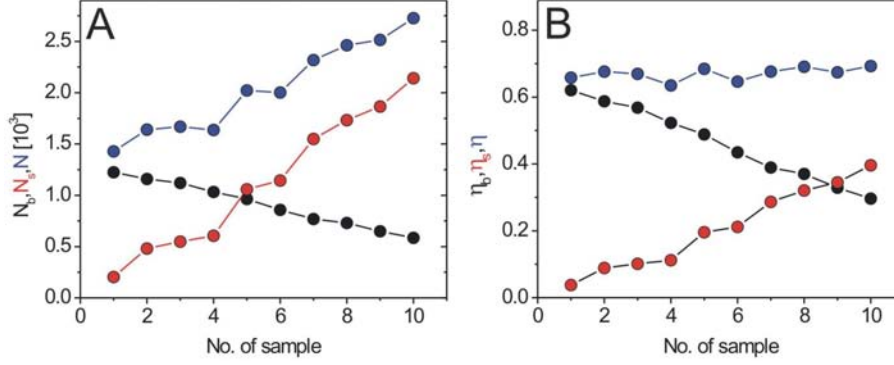


FIGURE 5.5. A) Number of particles N_b (black line and symbols), N_s (red), N (blue) and B) corresponding packing fractions η_b , η_s , η vs. number of snapshot. The single snapshots are representing the corresponding sample numbers.

To characterize the binary mixtures recorded on the images, we identified the number N_b (N_s) of big (small) particles and their coordinates (x_μ, y_μ) ($\mu = 1 \dots N$ where $N = N_b + N_s$). We were able to access these parameters using a standard 2D particle-detection algorithm [89] which determines the size ($\rightarrow N_s, N_b$) and the intensity-weighted centroid ($\rightarrow (x_\mu, y_\mu)$) of each single particle. From N_b and N_s we calculated the respective packing fractions $\eta_b = N_b \pi \sigma_b^2 / (4L^2)$ and $\eta_s = N_s \pi \sigma_s^2 / (4L^2)$ of big and small particles. The corresponding state points are shown in the (η_s, η_b) -phase diagram (Figure 5.3A). The solid line is a linear fit to the data points corresponding to a total packing fraction of $\eta = 0.735$. Our data scatter at approximately $\pm 5\%$ around this value. To improve statistics for the calculation of the pair correlation functions $h_{ij}(r)$ we sorted the data points into 10 equidistant bins along the linear fit (Figure 5.3B). The first bin (indicated by the 1) corresponds to the set $(\eta_b, \eta_s) = (0.66, 0.075)$ and then η_b (η_s) decreases (increases) in steps of $\Delta n = 0.04$ for each bin (indicated by the arrow). Each bin contains between 5 and 10 of the original recorded images. In the following we refer to the bins as sample numbers. Figure 5.4 depicts single snapshots representing the sample numbers. In Figure 5.5A the numbers N_b , N_s and N are plotted versus the snapshot number. As can be seen from Figure 5.5A sample No.5 corresponds to a symmetric binary mixture where $N_b \approx N_s$. Consequently, we expect to observe structural crossover in the vicinity of this sample. The corresponding packing fractions η_b , η_s and η are shown in Figure 5.5B. It is clearly visible that we indeed follow a linear path through the phase diagram with $\eta = const$.

5.4. EXPERIMENTAL RESULTS

According to the theoretical results described above, all pair correlation functions $h_{bb}(r)$, $h_{ss}(r)$, $h_{bs}(r)$, and $h_{sb}(r)$ exhibit similar structural crossover behavior. Since $h_{bs}(r)$ and $h_{sb}(r)$ are difficult to determine experimentally, we focused on $h_{ss}(r)$. The reason is that it benefits from better statistics compared to $h_{bb}(r)$ because for the samples altogether, there are more small particles available than big ones. The evaluated $h_{ss}(r)$ are shown in Figure 5.6A. For each sample $h_{ss}(r)$ displays a peak which is located at a distance r slightly larger than σ_s (indicated by the left gray line) and therefore corresponds to two neighboring small particles. Then $h_{ss}(r)$ for sample No.1 has a second peak located at $r = \sigma_b + \sigma_s$ (right gray line) which can be interpreted as two small particles with a big one in between. It is clear that this is a rather likely configuration in a binary mixture of many big and few small particles appearing as a peak in $h_{ss}(r)$. Of course, the configuration gets less likely the more small particles are added. Accordingly, the peak gradually disappears with increasing sample number. At the same time, the configuration of two small particles with another small one in between gets more likely and thus a peak at $r = 2\sigma_s$ gradually appears (intermediate gray line). In addition to the near field structure, the $h_{ss}(r)$ of samples No.1,2 and 8-10 display a structure of higher-order peaks separated from each other either by σ_b or σ_s , respectively. In contrast, no structure of higher-order peaks can be observed for samples 3-7.

In conclusion, we observe a near field structure of $h_{ss}(r)$ which can be explained well for all samples; we are however not able to resolve the structure of $h_{ss}(r)$ at intermediate distances for a rather large number of five samples corresponding to a range of $\Delta\eta_b = \Delta\eta_s = 0.2$. The logarithmic representation $\ln|h_{ss}(r)|$ plotted in Figure 5.6B does not allow for an identification of crossover behavior as well. We therefore additionally analyzed the Fourier spectrum $\tilde{h}_{ss}(k)$ of $h_{ss}(r)$ with k the wave vector². The asymptotic behavior of $h_{ss}(r)$ should be of the form

$$h_{ss}(r) \propto \exp(-r/r_i) \cos(k_i r + \phi) \quad (5.6)$$

with r_i being the decay length and $k_i = 2\pi/\sigma_i$. $i = b, s$, depending on (η_s, η_b) of the sample³. The Fourier transform of (5.13) is a Lorentzian,

$$\tilde{h}_{ss}(k) \propto \frac{1/r_i}{1/r_i^2 + (k - k_i)^2}; \quad (5.7)$$

we therefore expect that the Fourier spectrum displays a peak of the form (5.7) located at k_i provided that $h_{ss}(r)$ is actually governed by a single mode of the form (5.6). The peak will sharpen and its height increase if the decay length r_i increases. Indeed, the

²In two dimensions for radial symmetric functions the Fourier transform becomes a Bessel transform. However, for the identification of the dominant wavelength the usual Fourier transform, which is numerically easier to handle, predicts equivalent results.

³ ϕ denotes a phase factor which is unimportant in the following.

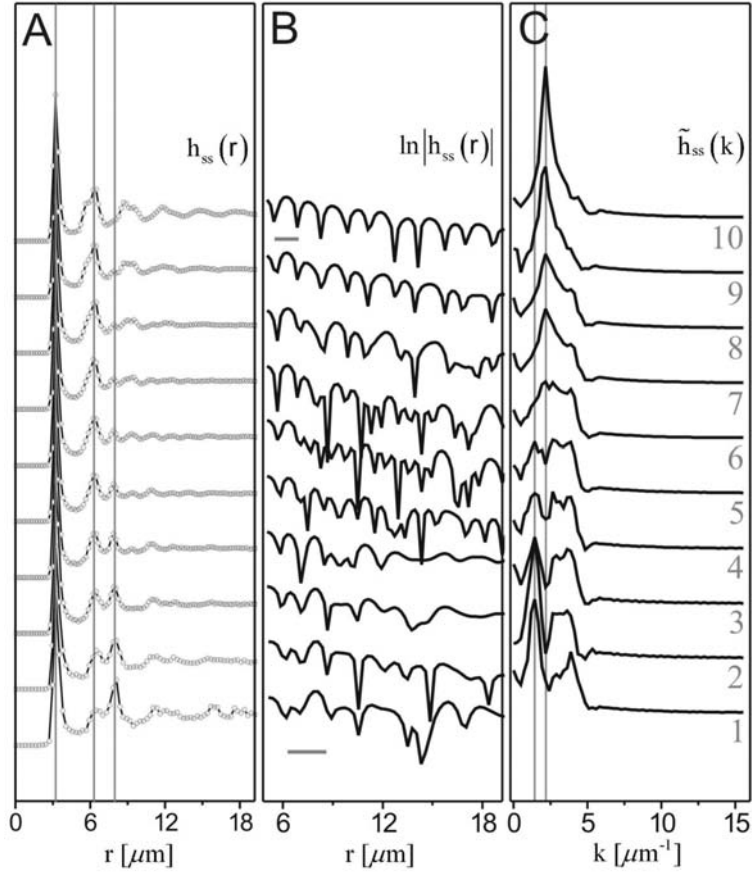


FIGURE 5.6. A) Small-small pair correlation function $h_{ss}(r)$ determined from the experimental data. B) Logarithmic representation $\ln|h_{ss}(r)|$ and C) Fourier transform $\tilde{h}_{ss}(k)$. The curves correspond to the sample numbers introduced in Figure 5.3B starting with sample No.1 at the bottom (indicated by the numbers 1-10 in Figure C). In Figure A the vertical gray lines correspond (beginning from the left) to the distances $r = \sigma_s$, $r = 2\sigma_s$ and $r = \sigma_s + \sigma_b$. The horizontal gray bars in Figure B represent the radii $\sigma_b/2$ (lower bar) and $\sigma_s/2$ (upper bar). The left (right) vertical gray lines in Figure C indicate the big (small) wave numbers $k = 2\pi/\sigma_b$ ($k = 2\pi/\sigma_s$). Curves are shifted vertically for clarity and y -labels are displayed in the upper right corner of the graphs.

Fourier spectra determined from the experimental data (see Figure 5.6C) clearly reveal a leading peak. The one corresponding to sample No.1-5 is located at k_b . It decreases and broadens with increasing sample number and finally disappears for sample No.5. For sample No.6, we again observe a leading peak, now located at k_s . It increases and sharpens from sample No.6 to 10. Hence, this provides experimental evidence of structural crossover in binary hard-sphere mixtures. Additionally, we can derive from the varying shape of the leading peak that highly asymmetric binary mixtures (sample

No.1, $N_b \gg N_s$ and No.10, $N_b \ll N_s$) exhibit a structure of higher-order peaks which gradually weakens for the symmetric mixtures (No.4-6, $N_b \approx N_s$).

The analysis of $h_{ss}(r)$ in Fourier space clearly bears evidence of structural crossover although we do not observe a sharp crossover transition but rather a crossover range. We must restrict our identification of leading peaks to samples where the leading peak is clearly silhouetted against the background. In that sense we confine the crossover range to sample No.4-6. In terms of packing fractions this corresponds to $\eta_b = 0.49 \pm 0.06$ and $\eta_s = 0.23 \pm 0.06$ compared to the DFT value $\eta_s = 0.3$. As shown in Section 5.8, the measured η_s is somewhat smaller due to a particle detection artifact and is therefore considered to agree well with the calculated η_s .

To improve the quality of our results we now turn to the total correlation function $h_{tot}(r)$ which does not suffer from incorrect particle detection. Furthermore it benefits from the full statistics available because the complete set of particle coordinates (x_μ, y_μ) can be used for evaluation. $h_{tot}(r)$ is expected to display crossover behavior because it is a linear superposition of the $h_{ij}(r)$ which are all governed by the same asymptotic decay,

$$h_{tot}(r) = \sum_{i,j=b,s} x_i x_j h_{ij}(r), \quad (5.8)$$

with the mole fraction of component i ,

$$x_i = \frac{\rho_i}{\sum_i \rho_i}. \quad (5.9)$$

ρ_i denotes the density of particle species i . The $h_{tot}(r)$ evaluated from our data are shown in Figure 5.7A. As expected the statistical noise is considerably reduced. The first peak is split into three subpeaks located at $r = \sigma_s$, $r = (\sigma_s + \sigma_b)/2$ and $r = \sigma_b$ (vertical gray lines). The first (latter) peak corresponds to two neighboring small (big) particles and is growing (shrinking) from sample No.1 to 10 just reflecting the increasing (decreasing) number of small (big) particles. The intermediate peak corresponds to a small particle neighboring a big one. This configuration is most likely for symmetric mixtures ($N_b \approx N_s$) and unlikely for highly asymmetric ones ($N_b \gg N_s$ or $N_b \ll N_s$). Therefore, the height of this peak is increasing from sample No.1 to 5 and then decreasing again. As in the case of $h_{ss}(r)$, the $h_{tot}(r)$ corresponding to asymmetric mixtures (No.1,10) exhibit a higher-order peak structure which gradually disappears in symmetric mixtures (No.5,6). In contrast to the $h_{ss}(r)$, however, the crossover behavior is already visible in the higher-order peak structure of the $h_{tot}(r)$ and their logarithmic representations in Figure 5.7B. The $h_{tot}(r)$ corresponding to sample No.1-4 and 7-10 clearly oscillate on σ_b and σ_s , respectively (indicated by the lower and upper horizontal bar in Figure 5.7B). This is supported by the Fourier spectra $\tilde{h}_{tot}(k)$ depicted in Figure 5.7C where the wave numbers k_i corresponding to σ_i are marked by vertical gray lines; here, sample No.5 and 6 can be even assigned to the large and small wavelength σ_b

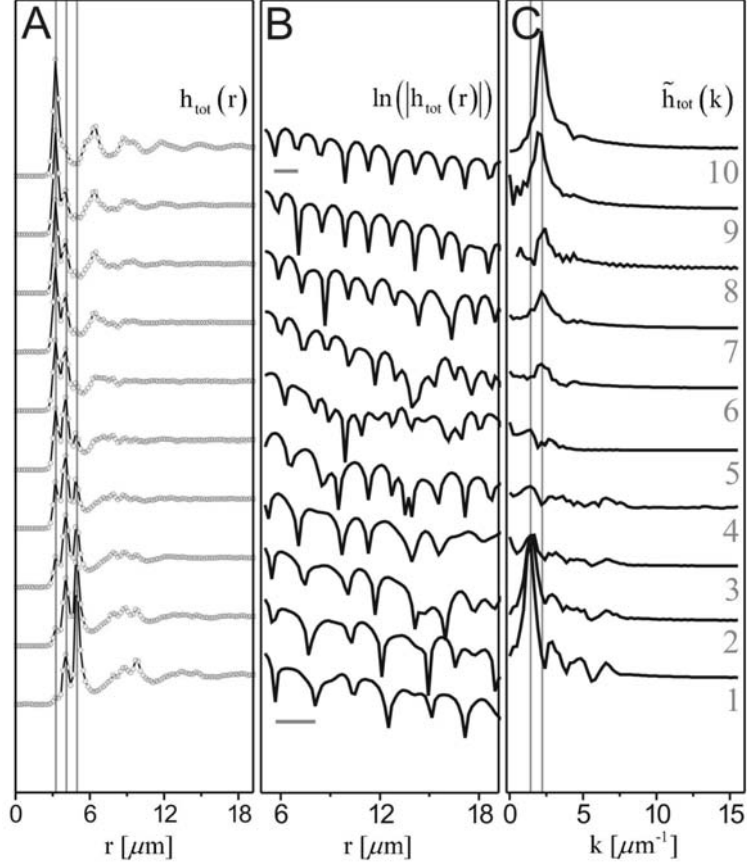


FIGURE 5.7. A) Total pair correlation function $h_{tot}(r)$ determined from the experimental data. B) Logarithmic representation $\ln(|h_{tot}(r)|)$ and C) Fourier transform $\tilde{h}_{tot}(k)$. The curves correspond to the sample numbers introduced in Figure 5.3B starting with sample No.1 at the bottom (indicated by the numbers 1-10 in Figure C). In Figure A the left (right) gray solid line corresponds to the distance between two neighboring small (big) particles, $r = \sigma_s$ ($r = \sigma_b$). The line in-between represents neighboring small and big particles, $r = (\sigma_b + \sigma_s)/2$. The horizontal gray bars in Figure B correspond to $\sigma_b/2$ (bottom bar) and $\sigma_s/2$ (top bar). The left (right) gray line in Figure C belongs to the big (small) wave number, $k = 2\pi/\sigma_b$ ($k = 2\pi/\sigma_s$). Curves are shifted vertically for clarity and y -labels are displayed in the upper right corner of the graphs.

and σ_s , respectively. We can therefore center the range of structural crossover around $\eta_b = 0.47$ and $\eta_s = 0.265$, in good agreement with the calculated value $\eta_s = 0.3$, again mentioning that the measured η_s is expected to be too small due to particle detection limitations (see Section 5.8).

In conclusion, we provide strong experimental evidence for structural crossover in binary hard-sphere mixtures. In addition, we observe good quantitative agreement between experiment and DFT calculations.

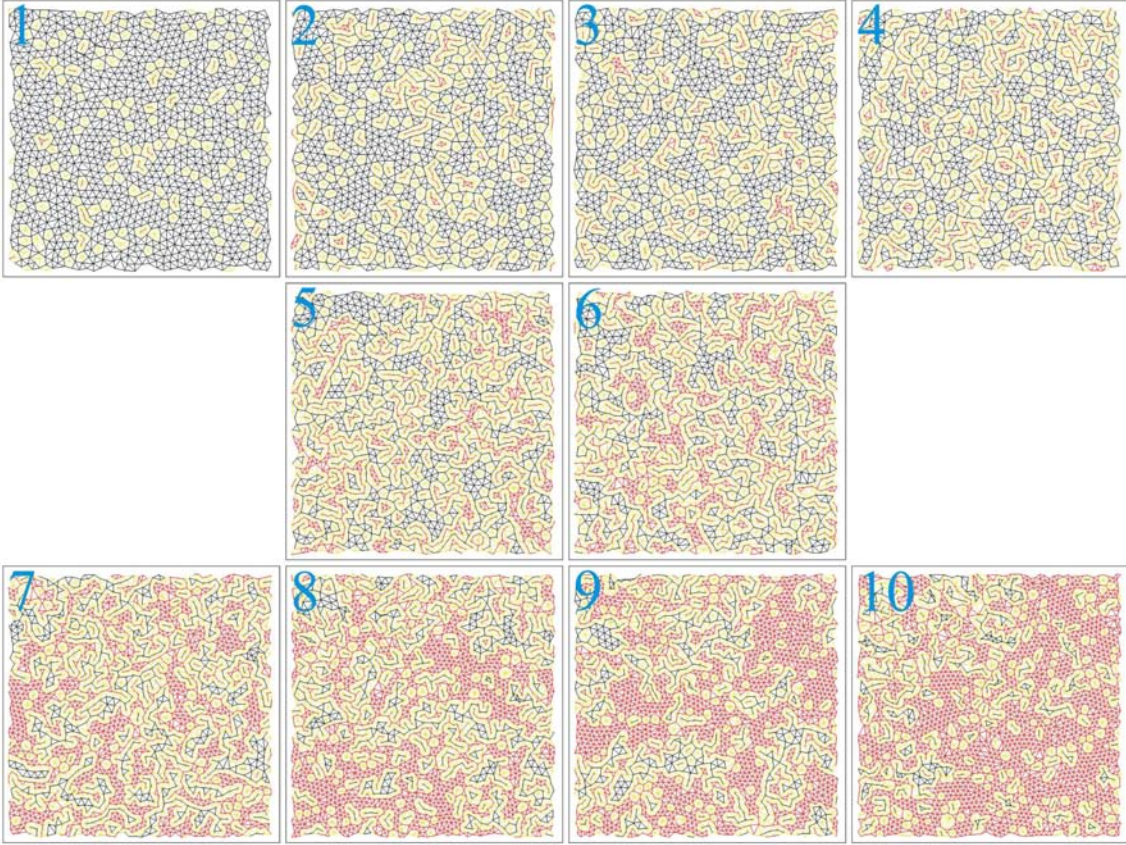


FIGURE 5.8. 2D-bond analysis of sample No.1-10 based on Delaunay triangulation. The bonds between two big (small) particles are colored in black (red). Yellow bonds correspond to a big particle connected to a small one. Sample No.5 and 6 correspond to the range where structural crossover occurs according to the asymptotic behavior of $h_{ss}(r)$ and $h_{tot}(r)$.

5.5. CONNECTIVITY ANALYSIS

So far we discussed structural crossover in terms of pair correlation functions which are spatially averaged quantities. Since our recorded images naturally provide detailed structural information, we investigate in the following what are the repercussions of the structural crossover to the real-space structure.

The basic idea of the real space structural analysis presented in the following is that two particles of species i are correlated if they are connected by a chain of particles of the same species. Note that particles do not necessarily have to be in physical contact to form a chain; they must, however, be connected via a nearest-neighbor bond which, in the case of one-component systems, can be determined by a well known procedure: the first minimum of the pair correlation function $h(r)$ which approximately constitutes 1.3 times the mean particle distance a is defined as a cutoff-length. Then, the nearest neighbors of a reference particle are those which are closer to it than the

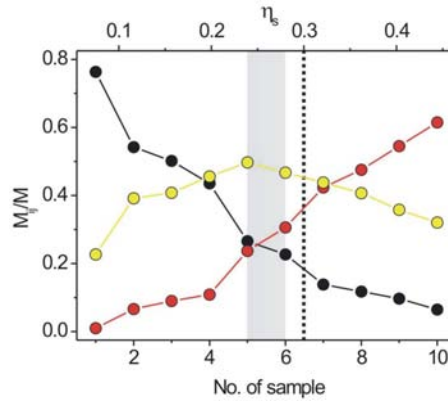


FIGURE 5.9. Number of bonds M_{ij} normalized to the total number of bonds M versus sample number. $i = j = b$ (black symbols and line), $i = j = s$ (red), $i = b$ and $j = s$ (yellow). The gray square represents the range of crossover determined from the evaluation of $h_{ss}(r)$ and $h_{tot}(r)$ and the dashed line the crossover value $\eta_s = 0.3$ evaluated from DFT calculations.

cutoff-length. Unfortunately, this straight-forward procedure is not applicable to binary mixtures considered here because there is no suitable single length scale, such as a mean particle distance, available. Therefore, we instead applied a method called Delaunay triangulation which constructs a network of non-overlapping triangles each connecting three nearest-neighbor particles⁴. Finally, we obtained the bonds between the nearest-neighbor particles and stored them in the 2D plots shown in Figure 5.8 for sample No.1-10. To distinguish between the particle species connected to each other we colored bonds between two big and small particles in black and red, respectively. Additionally, we used yellow color for mixed bonds between big and small particles. As can be seen the number of small-small bonds increases with increasing sample number, leading to fragmentation of the system-spanning big-big network (No.1-4) into smaller, randomly distributed patches (No.5). Beginning with sample No.6, the role of big and small particles is inverted and small-small bonds form a network spanning the entire area (No.10). Figure 5.9 supports this qualitative interpretation depicting the numbers M_{bb} of big-big (black symbols and line), M_{ss} of small-small (red) and M_{bs} of big-small (yellow) bonds normalized to the total number M of bonds. Clearly the big-big (small-small) bonds are dominating for the asymmetric samples No.1-4 (7-10) while the symmetric samples No.5 and 6 are governed by the mixed bonds. Recall that according to the evaluation of $h_{ss}(r)$ and $h_{tot}(r)$ these samples belong to the range where structural crossover is observed.

Clearly, the bond analysis already bears qualitative evidence for the relationship between structural crossover and the size of networks consisting of particle species i . In addition, the radius of gyration R_g allows for a quantitative measure of the

⁴For instance, see http://en.wikipedia.org/wiki/Delaunay_triangulation

network size. For instance, R_g is well known as an estimate for the size of molecules or polymers [90,91]. It is defined as

$$R_g^{(i)} = \sqrt{\frac{1}{n^{(i)}} \sum_{k=1}^{n^{(i)}} (\mathbf{x}_k^{(i)} - \mathbf{R}_0^{(i)})^2}, \quad (5.10)$$

where we have already distinguished between the two particle species indicated by the superscript i . $\mathbf{R}_0^{(i)}$ is the centroid position of the network and $n^{(i)}$ denotes the number of particles of size i located in the network at positions $\mathbf{x}_k^{(i)}$ ($k = 1 \dots n^{(i)}$). Computing this quantity for all, say $N_C^{(i)}$, networks formed by connected particles of size i finally yields a weighted-averaged radius of gyration

$$\langle R_g^{(i)} \rangle = \frac{1}{N^{(i)}} \sum_{m=1}^{N_C^{(i)}} n^{(i)}(m) R_g^{(i)}(m) \quad (5.11)$$

where $N^{(i)}$ denotes the total number of particles i . We calculated $\langle R_g^{(i)} \rangle$ for networks consisting of connected big or small particles and plotted these for our experimental data in Figure 5.10 as a function of sample number. At small and high sample numbers the values saturate while a relatively sharp transition with an intersection point occurs between sample No.6 and 7. On the one hand this intersection point lies outside the range of crossover determined from the pair correlation functions (indicated by the gray square), but on the other hand coincides with the crossover transition evaluated from DFT calculations. This agreement is a consequence of the particle-detection limitations (see Section 5.8) shifting true intersection point between $R_g^{(b)}$ and $R_g^{(s)}$ to higher sample numbers; however, our results clearly suggest that the structural crossover corresponds

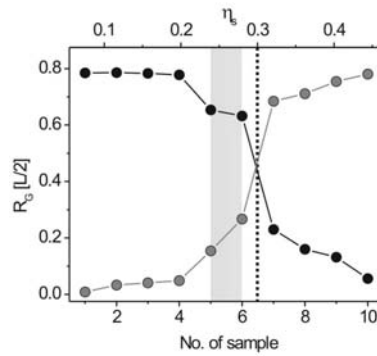


FIGURE 5.10. Averaged radii of gyration $\langle R_g^{(i)} \rangle$ (normalized to $L/2$ with L^2 the size of the field of view) of networks formed by large (black symbols) and small particles (gray symbols) as a function of the sample number. The corresponding packing fraction of small particles η_s is indicated as well. The gray area and the dashed line respectively indicate the crossover as determined from the correlation functions and from DFT.

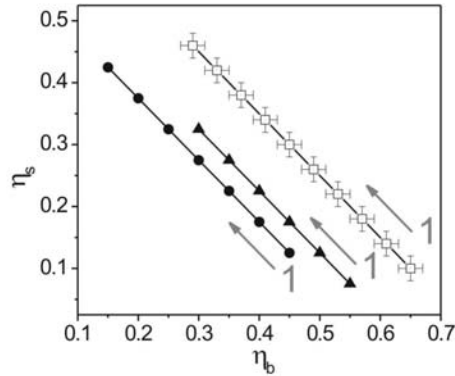


FIGURE 5.11. Different paths with constant total packing fraction η in the (η_s, η_b) -phase diagram. MC simulations (closed circles: $\eta = 0.575$, $q = 0.5$) and (closed triangles: $\eta = 0.625$, $q = 0.4$). For comparison, the experimental data set is also depicted (see Figure 5.3B). The MC state points are labeled with sample numbers increasing in the direction indicated by the arrows.

to a competition between the sizes of networks consisting of connected big or small particles, respectively.

5.6. MC-SIMULATIONS: STRUCTURAL CROSSOVER AT DIFFERENT q AND η

So far we discussed the connectivity analysis on the basis of our experimental data. To check the connectivity analysis for different size ratios and packing fractions as well, we used Monte-Carlo (MC) simulations.

We have performed MC simulations at size ratios $q = 0.5$ and $q = 0.4$. The corresponding paths through the phase diagram (see the closed symbols in Figure 5.11) were obtained from 2D simulations with a fixed number of particles of $0 < N < 3000$ for both species and box areas of approximately $1500\sigma_b^2$ employing periodic boundary conditions. From the configurational snapshots we first determined the range of crossover by analyzing $h_{bb}(r)$, available statistically here because each particle has been sampled using 10^4 MC cycles. We then performed the above mentioned connectivity analysis⁵. The result for the $q = 0.4$ data set is shown in the 2D plots of Figure 5.12 using black, red and yellow color code for big-big, small-small and big-small bonds. As for the experimental data the transition from a system-spanning network of big particles to a system-spanning network of small particles can be located qualitatively (around sample No.2). Subsequently we calculated $\langle R_g^{(i)} \rangle$ for networks of connected big or small particles. The corresponding radii of gyration are plotted in Figure 5.13 and show a similar

⁵We performed the bond analysis not only for single snapshots but for the whole set of configurational data. The results differed marginally from the single snapshot ones.

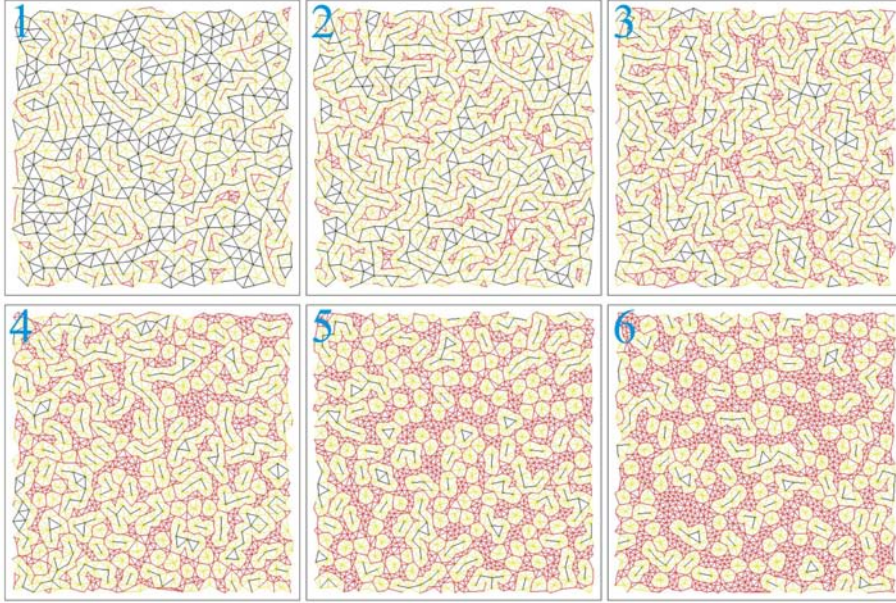


FIGURE 5.12. 2D-bond analysis for MC simulation ($q = 0.4$) based on Delaunay triangulation. The bonds between two big (small) particles are colored in black (red). Yellow bonds correspond to a big particle connected to a small one.

behavior as in the experiment. Again, the intersection points are consistent with the crossover region as determined from the correlation functions and DFT calculations.

However, for both MC simulations the intersection points are shifted to larger η_b and smaller η_s with respect to the crossover region determined from correlation functions and DFT calculations. To explore the origin of this systematic deviation, we first consider the probability p_i of finding a particle of size i in a binary mixture. Due to the finite particle size, p_i is given by the packing fraction η_i and not by the relative number of particles N_i/N as one might think initially. Since the pair correlation function $h(r)$ requires $p_i = \eta_i$, we cannot expect $\langle R_g^{(i)} \rangle$ to allow for an analogous description of structural crossover as it does not account for particle size. Big- and small-particle networks of same size are treated equally by $\langle R_g^{(i)} \rangle$. To restore the analogy between $h(r)$ and $\langle R_g^{(i)} \rangle$ the latter has to be weighted by the probability p_i . The result is shown in Figure 5.13C and D for the MC simulations with $q = 0.5$ and $q = 0.4$, respectively. Now, the intersection points are in excellent agreement even with the crossover transition inferred from DFT. This demonstrates that structural crossover is accompanied by a competition between big and small particles governed by the probabilities of finding a particle of species i and a network of size $\langle R_g^{(i)} \rangle$. Consequently, the change

$$\eta_b \langle R_g^{(b)} \rangle > \eta_s \langle R_g^{(s)} \rangle \quad \leftrightarrow \quad \eta_s \langle R_g^{(s)} \rangle > \eta_b \langle R_g^{(b)} \rangle \quad (5.12)$$

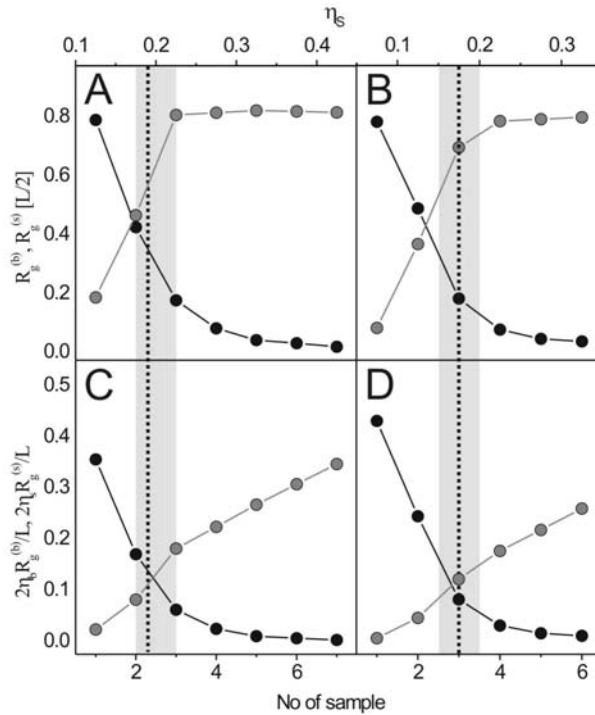


FIGURE 5.13. Averaged radii of gyration $\langle R_g^{(i)} \rangle$ (normalized to $L/2$) of networks formed by large (black symbols) and small particles (gray symbols) as a function of the sample number for MC simulations A) at $\eta = 0.575$ and $q = 0.5$ and B) at $\eta = 0.625$ and $q = 0.4$. The corresponding packing fraction of small particles η_s is indicated as well. The gray area and the dashed line indicate the crossover as determined from correlation functions and from DFT. C)+D) Corresponding $\langle R_g^{(i)} \rangle$ weighted with η_i .

provides a simple real-space argument why the oscillation wavelength of the $h_{ij}(r)$ in the asymptotic limit is either set by σ_b or σ_s ⁶.

5.7. CONCLUSIONS AND OUTLOOK

We have experimentally demonstrated the structural crossover in a binary colloidal hard-sphere system. Furthermore, we show that structural crossover is strongly coupled to the size of networks containing connected equally-sized particles only. Going across the structural crossover, the size ratio of such networks comprised by either connected big or small particles is reversed. We believe this real-space configurational picture of structural crossover is not just applicable to binary hard spheres, as structural crossover is a generic feature of mixtures with competing length scales. Moreover, it shows interesting similarities with force chains in granular matter [92] and glassy systems

⁶Interestingly, the relation (5.12) has a near-field counterpart which is obtained when $\langle R_g^{(i)} \rangle$ is replaced by the number of nearest neighbors $i-i$. But, the near-field relation is only connected to the asymptotic behavior of the $h_{ij}(r)$ implicitly and therefore is not discussed here in detail.

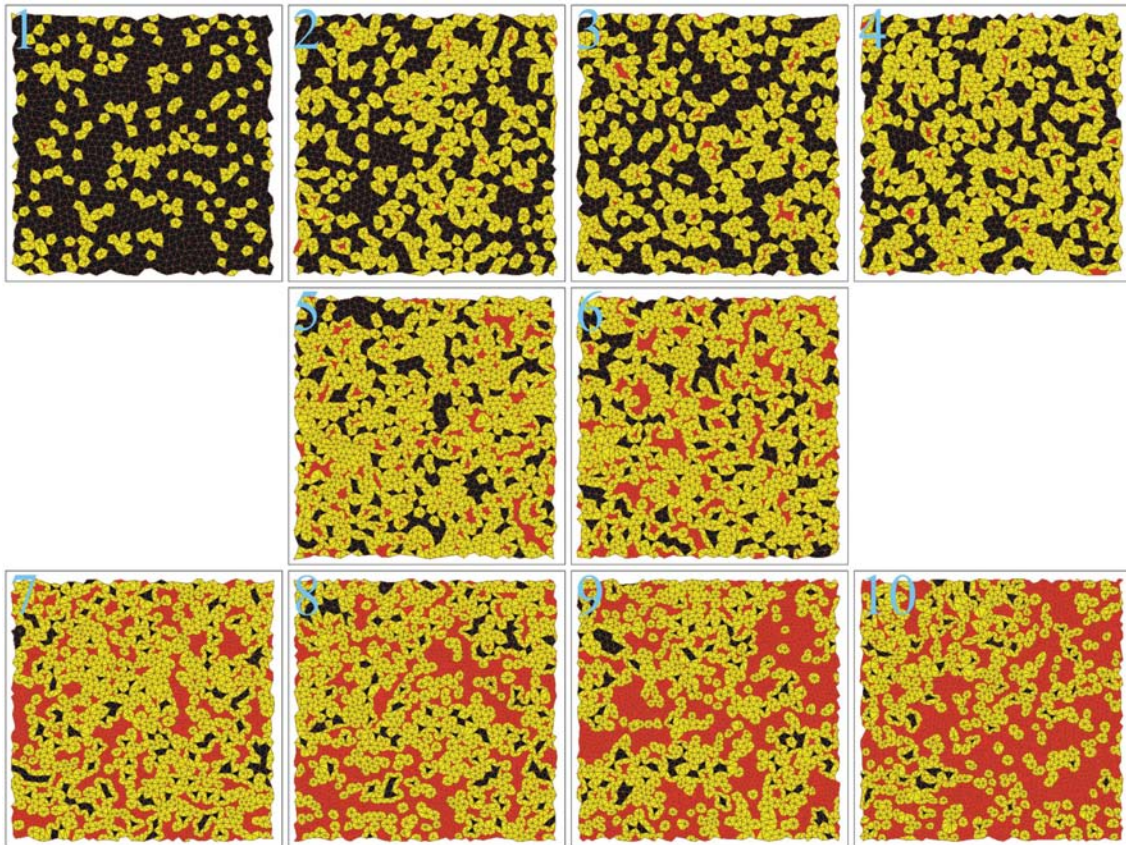


FIGURE 5.14. Surface representation of the bond analysis for the experimental samples No.1-10. The bonds determined by means of Delaunay triangulation are colored in brown irrespective of the particle species they connect. If a triangle refers to three big (small) particles its surface is colored in black (red). Otherwise the color is yellow.

[77, 78, 93] of dissimilar sized particles. Therefore, our finding may help to gain more insight into structure-related properties in binary systems at a universal level.

A remaining question concerning structural crossover is the basic mechanism behind it. Does it depend on the competition between homogeneously mixing and segregation into regions consisting of one particle species i only? Or does structural crossover also occur in a binary mixture where the particles are just distributed randomly? We will investigate the latter in cooperation with Grodon et al. applying both the pole and the connectivity analysis. As far as the first question is concerned we evaluated the bond analysis in a different manner. Instead of applying a color code on the bonds as in Figure 5.8 we colored the triangles depending on which particle species i , j and l they connect. If $i = j = l = b$ ($= s$) we used black (red) color and yellow otherwise. If the binary system tends to mix (segregate) we expect black or red (yellow) as the dominating color. The experimental results are shown as 2D plots in Figure 5.14. As can be seen, yellow is the dominating color except for samples No.1 and 10. In Figure

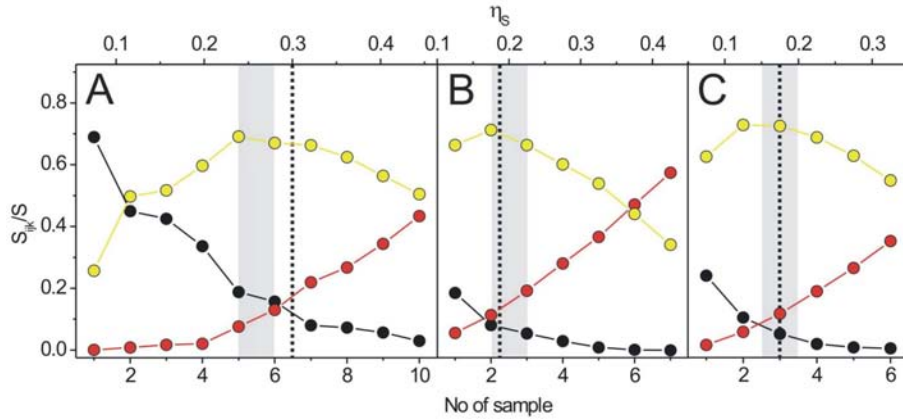


FIGURE 5.15. Degree of surface covering S_{ijl}/S versus sample number: A) Experiment, B) MC simulation for $q = 0.5$ and C) for $q = 0.4$. $S = L^2$ is the area of the field of view and S_{ijl} is the part of S covered by triangles connecting three particles of sizes i , j and l . If $i = j = l = b (= s)$ the color of the line and symbols is black (red) and yellow otherwise. The grey area and the dashed line indicate the crossover as determined from the correlation functions and from DFT. The packing fraction of the small particles η_s corresponding to the sample numbers is plotted as well.

5.15A we plotted the surface S_{ijl} of the triangles $i - j - l$ normalized to the field of view $S = L^2$. In Figure 5.15B and C this is shown for the MC simulation data as well. In all three cases, the triangles connecting particles of different size clearly dominate. Homogenously mixing therefore seems to be the dominating mechanism.

Another open question is related to the connectivity analysis. Can it be applied to mixtures of dimensionality different than 2? In the case of three-dimensional mixtures, it is intuitively clear that the formalism should work well. However, in one dimension the connectivity analysis fails. Of course, there will never be a system-spanning network of particles of one species which turned out to be crucial for our real-space interpretation of structural crossover in 2D.

5.8. APPENDIX: LIMITATIONS OF THE EXPERIMENTAL METHOD

In the following, we point out the limits of our experiment. First of all, we return to the snapshots shown in Figure 5.4 and, upon closer inspection, observe some voids. These are caused by the disordered structure of binary mixtures which does not allow for well-defined particle layers as in ordered one-component systems. Furthermore, the confocal microscope which scans lateral planes will not detect particles that are out of plane larger than approximately $600nm$. However, these voids have not a significant impact on data evaluation because the number of undetected particles is estimated to be less than 3%. Of course, the out-of-plane displacement of particles also leads to

incorrect determination of particle distances due to the projection onto a 2D image. This induces a small effective polydispersity which turned out not to be a problem because Grodon et al. still observed all the features of structural crossover for binary mixtures with polydispersities up to 5%.

While the issues mentioned so far can be neglected the following problem, concerned with the detection of the particle size $i = b, s$, cannot be ruled out as readily. Specifically, the size distributions P_b and P_s of the big- and small-particle images overlap. This is caused by the previously mentioned out-of-plane displacement of particles and by inhomogeneities in the optical imaging (dust, dirt). Unfortunately, one has to set a threshold in between the maxima of P_b and P_s which leads to a number $N_{b \rightarrow s}$ ($N_{s \rightarrow b}$) of big (small) particles that are detected as small (big) ones. If $N_b^{(t)}$ and $N_s^{(t)}$ denote the true values and $\Delta N = N_{b \rightarrow s} - N_{s \rightarrow b}$, the measured values are

$$N_b = N_b^{(t)} - N_{b \rightarrow s} + N_{s \rightarrow b} = N_b^{(t)} - \Delta N \quad (5.13)$$

$$N_s = N_s^{(t)} - N_{s \rightarrow b} + N_{b \rightarrow s} = N_s^{(t)} + \Delta N. \quad (5.14)$$

At first glance the discussion provided here seems unnecessary because the measured values only differ from the true ones if ΔN is non-zero. However for almost all samples N_b is larger than N_s (samples No.1-4) or vice versa (No.6-10). For this reason we expect for sample No.1-4 (6-10) more small (big) particles to be detected as big (small) ones than vice versa, $\Delta N < 0$ ($\Delta N > 0$). Consequently the measured η_b (η_s) will be too small (large) for samples No.1-4 and vice versa for No.6-10. Unfortunately we cannot provide an estimate for ΔN , but, as an example, a $\Delta N = 0.03N$ in sample No.10 already induces a shift in the packing fractions of approximately 0.02 which is half the bin size $\Delta\eta$. Consequently we must expect that the measured η_b and η_s at the crossover will differ quantitatively from the calculated values. The procedure of sorting the confocal images into bins, however, remains valid, because every image with true particle numbers $N_b^{(t)}$ and $N_s^{(t)}$ suffers from the same approximate ΔN and is therefore sorted into the same bin.

To conclude, our experimental results deviate from the theoretical ones quantitatively. Specifically, the intersection point in Figure 5.10 is shifted to higher packing fractions η_s .

6

Subdiffusive Brownian motion of colloidal particles on quasicrystalline substrates

ABSTRACT

We experimentally investigate the diffusive motion of Brownian particles on quasicrystalline pentagonal substrates by means of optical tweezers and video microscopy. With increasing substrate strength the measured mean-square displacements $\langle r^2(t) \rangle$ exhibit a subdiffusive range where $\langle r^2(t) \rangle \propto t^\nu$ with $\nu < 1$. For large time scales, $t \rightarrow \infty$, normal diffusion where $\nu = 1$ is recovered. In addition, we experimentally studied particle diffusion on periodic triangular substrates. Similar to the quasicrystalline substrate we observe a transition from short-time to slower long-time diffusion. However, we do not find subdiffusive particle motion. We compared our experimental data to results obtained in recent numerical and analytical studies and find good qualitative agreement.

6.1. INTRODUCTION

Diffusion processes are well known to be described by the famous Einstein relation [94] signifying that the mean-square displacement increases linearly with time, $\langle r^2 \rangle \propto t^\nu$ with $\nu = 1$. During the last ten years an anomalous diffusion has been reported in several experiments and numerical simulations investigating supercooled liquids and glass formation where $\nu < 1$ [14–16, 78, 95, 96]. This so-called subdiffusion is caused by a nearest-neighbor particle cage which suppresses caged-particle motion. The cage effect is also seen in granular matter under shear [97]. In addition, subdiffusion plays an important role in the kinetics of diffusion-mediated reactions in human cells and has been studied for a huge variety of lipids and proteins in the plasma membranes of cells [98–106]. A further important subdiffusive phenomenon is termed single-file diffusion which plays an important role in biophysics as well. Single-file diffusion is a many-particle effect occurring in narrow channels where the mutual passage of particles is excluded [107–114].

Colloids were used as a model system to perform systematic investigations on single-file diffusion. The channels were modeled by topographical patterns [115] or by scanned laser beams [116] (see Section 3.4). In a recent publication, a model system has been proposed for a more general investigation of subdiffusion [117]; colloids were subjected to a random substrate potential [118, 119] and the particle diffusion was simulated through Langevin dynamics. This model system can be realized experimentally through the use of optical tweezers (see Section 2.5). Possible approaches include the use of speckle-patterns [120] or fast-scanning intensity-controlled laser beams [121]; however, the former requires very high laser power and the latter suffers from the limited lateral expansion of the created pattern. To address this, Schmiedeberg and Stark developed a method going beyond randomly structured potentials and modeled a quasicrystalline pentagonal potential in their simulations. In this case, the substrate potential can be realized experimentally through a static five-beam interference pattern (see Section 3.1); the required laser powers are now available and the lateral extension is sufficiently large.

Most of the theoretical work devoted to subdiffusion to date is rather complex and based on Lévi walks or flights [122, 123]. These do not bear a direct relation to realistic systems because they do not depend on realistic physical parameters which could be varied systematically. The model system based on particle diffusion on random or quasicrystalline substrates is therefore of particular importance; one can investigate quantitatively how subdiffusive motion depends on physical parameters including substrate strength, substrate shape and coefficient of friction.

This chapter is organized as follows. In Section 6.2 we discuss the experimental realization of a quasicrystalline pentagonal potential. Next, the experimental results

are presented in Section 6.3. To provide a detailed discussion of the experimental results, we describe the theoretical studies of Schmiedeberg and Stark in Section 6.4. Finally, Section 6.5 contains conclusions and outlook.

6.2. EXPERIMENTAL METHOD

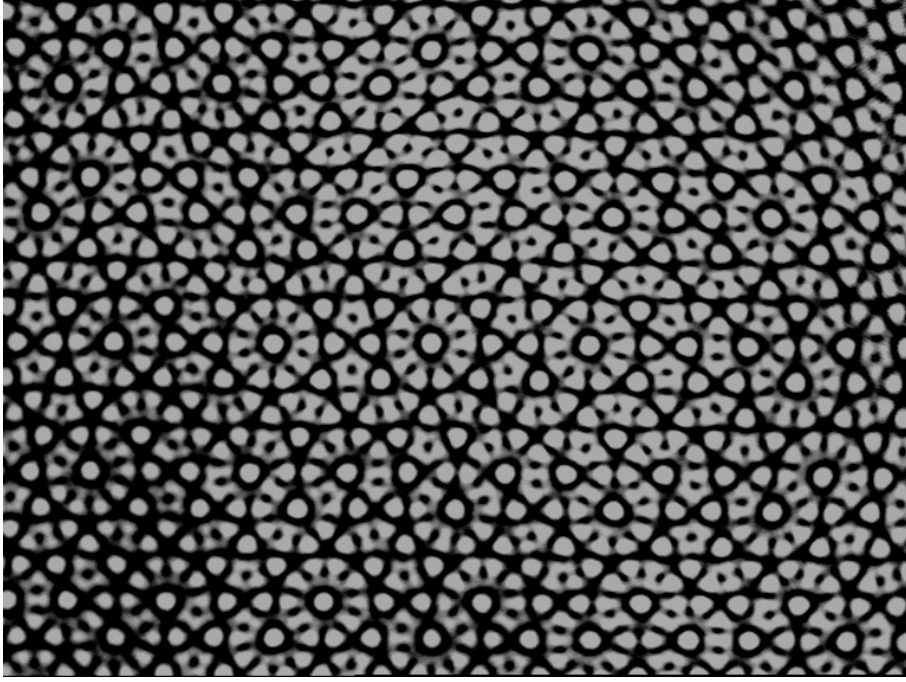


FIGURE 6.1. Snapshot of a quasicrystalline, pentagonal intensity pattern created by five interfering laser beams. The snapshot was recorded by means of videomicroscopy. The size is approximately $150\mu m \times 100\mu m$.

We created the quasicrystalline interference pattern by applying the basic methods and techniques described in Section 3.1. Five beams were arranged at positions (see (3.9) and Figure 3.7)

$$\mathbf{X}_n^{(5)} = \frac{s}{2} \left[\cos(18^\circ + (n-1) \cdot 72^\circ) \hat{e}_1 + \sin(18^\circ + (n-1) \cdot 72^\circ) \hat{e}_2 \right], \quad (6.1)$$

where $n = 1, \dots, 5$. Consequently, the wave vectors in the sample plane are

$$\mathbf{K}_n^{(5)} = \frac{\pi s}{\lambda f} \left[\cos(36^\circ + (n-1) \cdot 72^\circ) \hat{e}_x + \sin(36^\circ + (n-1) \cdot 72^\circ) \hat{e}_y \right]. \quad (6.2)$$

The electric fields of the laser beams can be written as

$$\mathbf{E}_n(\mathbf{r}, t) = (E \hat{e}_x + \Delta E \hat{e}_y) \cos(\mathbf{K}_n^{(5)} \mathbf{r} + \omega t + \phi_n), \quad (6.3)$$

where the beams are polarized in the x -direction. $\Delta E \ll E$ accounts for small deviations in the polarization which are unavoidably present mostly due to reflection and scattering within the sample cell. $\omega = 2\pi c/\lambda$ with $c = 3 \cdot 10^8 m/s$ and $\lambda = 532 nm$ the wavelength

of the laser light (Nd:YVO₄-laser, Coherent Verdi V5). The ϕ_n denote the laser beam phases. With (6.3), we obtain the pentagonal light potential,

$$V(\mathbf{r}) \propto \left\langle \left[\sum_{n=1}^5 (E\hat{\mathbf{e}}_x + \Delta E\hat{\mathbf{e}}_y) \cos(\mathbf{K}_n^{(5)}\mathbf{r} + \omega t + \phi_n) \right]^2 \right\rangle_t. \quad (6.4)$$

The temporal average reflects that colloids experience a quasi-static potential due to the self diffusion time of $\tau_s \approx 1s \gg \lambda/c$ (see Section 2.3). A snapshot of the experimentally realized intensity pattern is shown in Figure 6.1.

In the following, we address a subtlety of quasicrystalline light potentials. In general, substrate potentials are characterized by a length scale l and the potential well depth V_0 . For a periodic potential, the length scale is given by the period d and V_0 is identical for each well. Therefore, both d and V_0 can be measured for a periodic light-induced substrate by applying the calibration procedure described in Section 3.1.3. In contrast, this procedure cannot be applied to quasicrystalline substrates due to the non-periodicity. Here, l and V_0 have to be defined and determined as follows: from (6.2) we see that the characteristic length scale of the experimental potential is given by

$$l = \frac{2\lambda f}{s}. \quad (6.5)$$

Inserting $\lambda = 0.532\mu m$, $f = 10cm$ and $s = 0.8cm$ we obtain $l = 13.3\mu m$. Unfortunately, l has no clear physical meaning. It can however be related to a length scale l' allowing for an ostensive interpretation developed in the following. In each of the five lattice directions \mathbf{K}_n there are two pairs of lattice vectors, each interfering to a one-dimensional periodic modulation of wavelengths λ_1 and λ_2 (for instance, in the y -direction: $\{\mathbf{K}_1, \mathbf{K}_5\}$ and $\{\mathbf{K}_2, \mathbf{K}_4\}$). If one moves along the direction of an arbitrarily chosen \mathbf{K}_n , the potential minima are located at distances λ_1 and λ_2 from each other. λ_1 and λ_2 are related to an intermediate length scale l' via $\lambda_1 = l'\varphi$ and $\lambda_2 = l'/\varphi$ with φ the Golden ratio $\varphi = (1 + \sqrt{5})/2$. Expressing l' in terms of l yields $l' = l/(2\varphi \sin(36^\circ)) = 7\mu m$ which we substitute for l as the characteristic length scale¹. We now turn the second characteristic parameter V_0 which is identified with the depth of the deepest well in case of quasicrystalline substrates. Since we lack information about the laser beam phases ϕ_n we cannot locate the deepest well and therefore must estimate V_0 . For this, we blocked three of the five laser beams. The resulting 1D periodic potential was calibrated as described in Section 3.1.3. We then obtained the intensity of a single laser beam with respect to the measured potential strength. Finally, V_0 was calculated using the calibrated intensity for all five overlapping laser beams.

To compare results obtained for periodic and non periodic substrates, we also generated a periodic light-induced potential of triangular shape. For this, three beams were

¹In [124, 125], the mean particle distance a of a colloidal adsorbat is tuned to $a = l$ in order to check whether a 1D substrate induces a stable quasicrystalline adsorbat of pentagonal symmetry. The substrate is a superposition of two 1D periodic potentials (3.3) with periods $d = \lambda_1$ and $d = \lambda_2$.

arranged at positions (see (3.9) and Figure 3.7)

$$\mathbf{X}_n^{(3)} = \frac{s}{2} \left[\cos(30^\circ + (n-1) \cdot 120^\circ) \hat{\mathbf{e}}_1 + \sin(30^\circ + (n-1) \cdot 120^\circ) \hat{\mathbf{e}}_2 \right] \quad (6.6)$$

where $n = 1, 2, 3$. Accordingly, the wave vectors in the sample plane are

$$\mathbf{K}_n^{(3)} = \frac{\pi s}{\lambda f} \left[\cos(60^\circ + (n-1) \cdot 120^\circ) \hat{\mathbf{e}}_x + \sin(60^\circ + (n-1) \cdot 120^\circ) \hat{\mathbf{e}}_y \right] \quad (6.7)$$

and the light potential becomes

$$V(\mathbf{r}) \propto \left\langle \left[\sum_{n=1}^3 (E \hat{\mathbf{e}}_x + \Delta E \hat{\mathbf{e}}_y) \cos(\mathbf{K}_n^{(3)} \mathbf{r} + \omega t + \phi_n) \right]^2 \right\rangle_t. \quad (6.8)$$

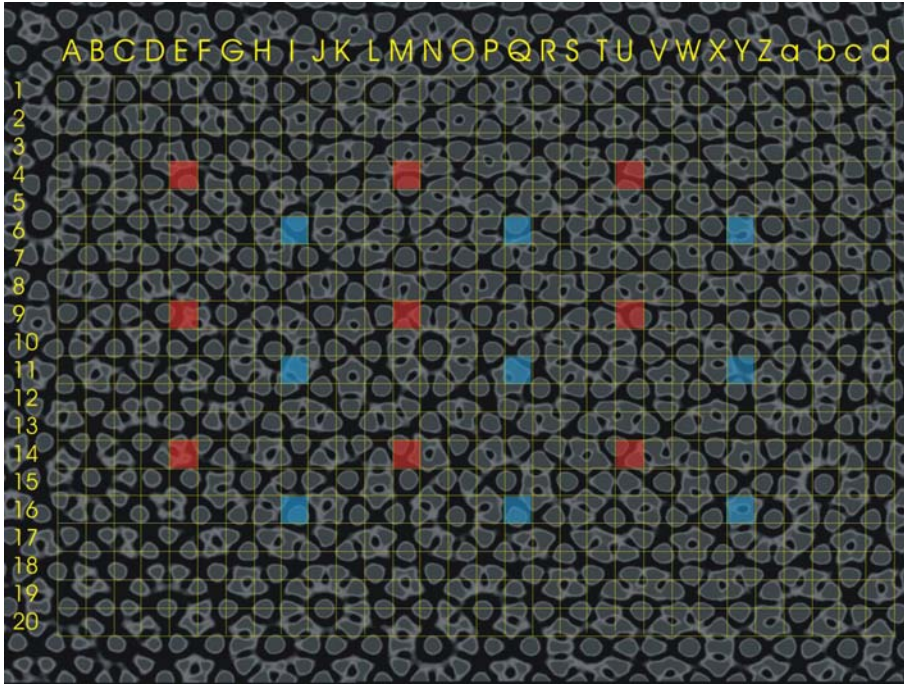


FIGURE 6.2. Preparation of different initial conditions. The quasicrystalline pattern is divided into small regions of approximately $7\mu m \times 7\mu m$. For each measurement 9 – 18 particles were subjected to the substrate using a pattern of initial positions indicated by the red and blue squares (see text for a detailed explanation).

In our experiments, we used a dilute suspension of $\sigma = 1.8\mu m$ polystyrene spheres sealed in a sample cell of type II (see Section 3.5). Since we are interested in single-particle diffusion, we do not require a strong pair interaction (2.10). Therefore, no deionization procedure was applied. For different laser powers, i.e. potential strengths, we recorded 30.000 – 100.000 images with a frequency of $10Hz$ by means of video microscopy. From the images we extracted the particle trajectories $r(t) = (r_x(t), r_y(t))$ and evaluated the mean-square displacements defined as

$$\langle r(t)^2 \rangle = \langle [r_x(t' + t) - r_x(t')]^2 \rangle_{N,t'} + \langle [r_y(t' + t) - r_y(t')]^2 \rangle_{N,t'}, \quad (6.9)$$

with N the number of particles recorded. To average over different initial conditions, the field of view ($\approx 150\mu\text{m} \times 100\mu\text{m}$) is split into $7\mu\text{m} \times 7\mu\text{m}$ patches (see Figure 6.2). By means of a single focused laser beam (see Section 3.4), we arranged the particles according to a configuration shown in Figure 6.2 as red or blue squares. In this case, the initial distances between the particles are large enough for the particles not to meet during the measuring period. For each laser power, $N \approx 100$ different initial conditions were realized.

6.3. EXPERIMENTAL RESULTS AND DISCUSSION

Figure 6.3A shows the trajectories of 72 particles recorded by means of video microscopy. The initial conditions were prepared according to the procedure described in Figure 6.2. It is clearly visible that the particles are trapped in potential wells of different depths. Some of the particles stay in the same well over the entire measuring period while others explore up to six wells. The mean-square displacements $\langle r^2(t) \rangle$ evaluated from the measured trajectories are provided in Figure 6.3B for different values of $V_0/k_B T$ between 0 and 20. Both $\langle r^2(t) \rangle$ and t are plotted logarithmically,

$$\log_{10}(\langle r^2(t) \rangle) = \log_{10}(4D(V_0/k_B T)) + \nu \log_{10}(t). \quad (6.10)$$

This representation is suitable for studying diffusive motion because diffusion (subdiffusion) manifests as a linear increase of $\log_{10}(\langle r^2(t) \rangle)$ with a slope equal to unity (smaller than unity). The cyan curve shown in Figure 6.3B corresponds to the case where no substrate is present, i.e. $V_0/k_B T = 0$. In this regime the diffusion is normal, i.e. $\nu = 1$. We denote the corresponding diffusion constant as D_0 . Upon increasing $V_0/k_B T$ a transition from normal short-time diffusion (diffusion constant D_S) to normal long-time diffusion (diffusion constant $D_L < D_S$) appears. The short-time diffusion only depends on the hydrodynamics of the solvent ($D_S = D_0$) and the long-time diffusion accounts for the substrate which impedes particle diffusion. Interestingly, D_S becomes smaller upon increasing $V_0/k_B T$. This is caused by the light pressure (2.26) which pushes particles towards the bottom plate of the sample cell. It is a well known effect that diffusion becomes smaller when the distance to the bottom plate is decreased [126,127]. As does D_S , D_L decreases with increasing $V_0/k_B T$. The particles more greatly feel the substrate and thus diffuse slower. For values larger than $V_0/k_B T = 7.7$ (green curve in Figure 6.3B), the transition $D_S \rightarrow D_L$ is more precisely governed by an intersecting subdiffusive regime which finally spreads over an order of magnitude in time for $V_0/k_B T = 20$ (black curve in Figure 6.3B). Hence, our results clearly demonstrate that particle diffusion exhibits subdiffusive behavior in the presence of a quasicrystalline pentagonal substrate. In addition, the results suggest the following interpretation. The diffusive motion of particles on a quasicrystalline pentagonal potential can be explained as a relaxation process into thermal equilibrium; to thermalize, particles must scan the

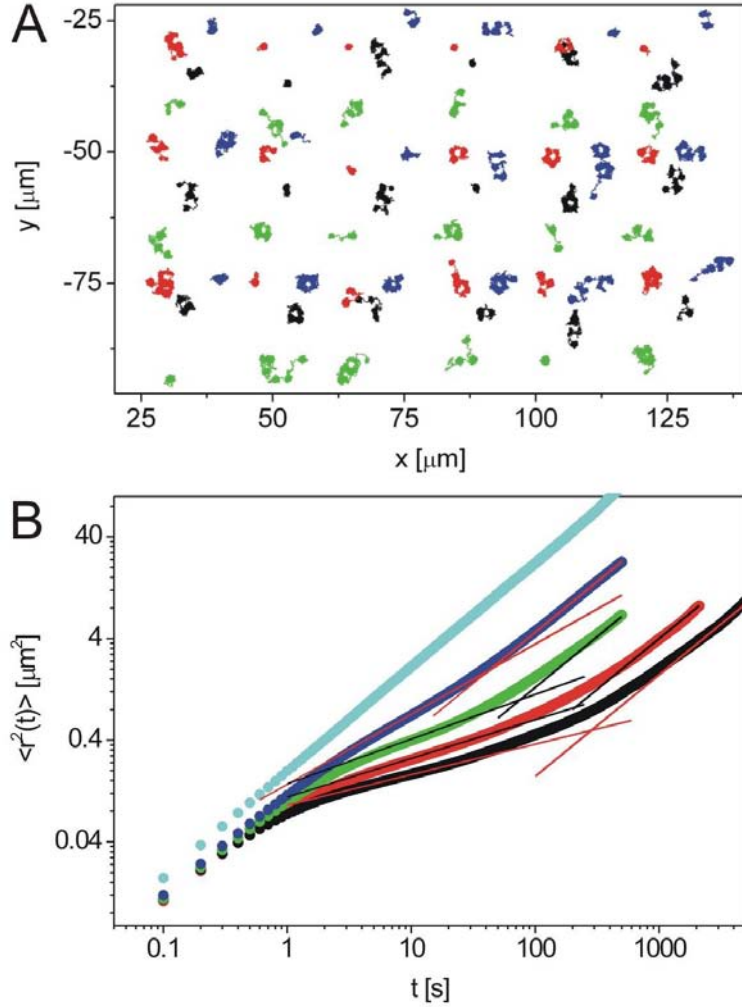


FIGURE 6.3. A) Trajectories $\mathbf{r}(t)$ recorded by means of video microscopy for $V_0/k_B T = 14.4$ and four sets of initial conditions prepared according to Figure 6.2 (distinguished by black, red, green, and blue color). B) Mean-square displacement $\langle r^2(t) \rangle$ versus time t determined from $\mathbf{r}(t)$. The depth of the deepest well was chosen as $V_0/k_B T = 0, 5.5, 7.7, 14.4, 20$ represented by cyan, blue, green, red, and black color, respectively. The solid lines emphasize the subdiffusive and the $t \rightarrow \infty$ diffusive part of $\langle r^2(t) \rangle$ and were obtained by analyzing the first derivative $d\langle r^2(t) \rangle/dt$ (see text for details). The different colors of the lines (black and red) were chosen to improve contrast.

entire distribution of potential well depth. We denote the equilibration time as t_{eq} and define it as the intersecting point of the subdiffusive and the long-time diffusive regime. For this, we numerically evaluated the first derivative of the mean-square displacement. This allowed determination of the point of inflection in the subdiffusive regime and the slope ν associated with the point of inflection. The long-time diffusion regime was identified for large times where ν becomes unity. Figure 6.3B shows the evaluated ν as

solid lines. As a result, we found that t_{eq} becomes larger upon increasing $V_0/k_B T$. This can be easily understood since particles occupy potential wells for longer time periods and accordingly, the equilibration process is prolonged.

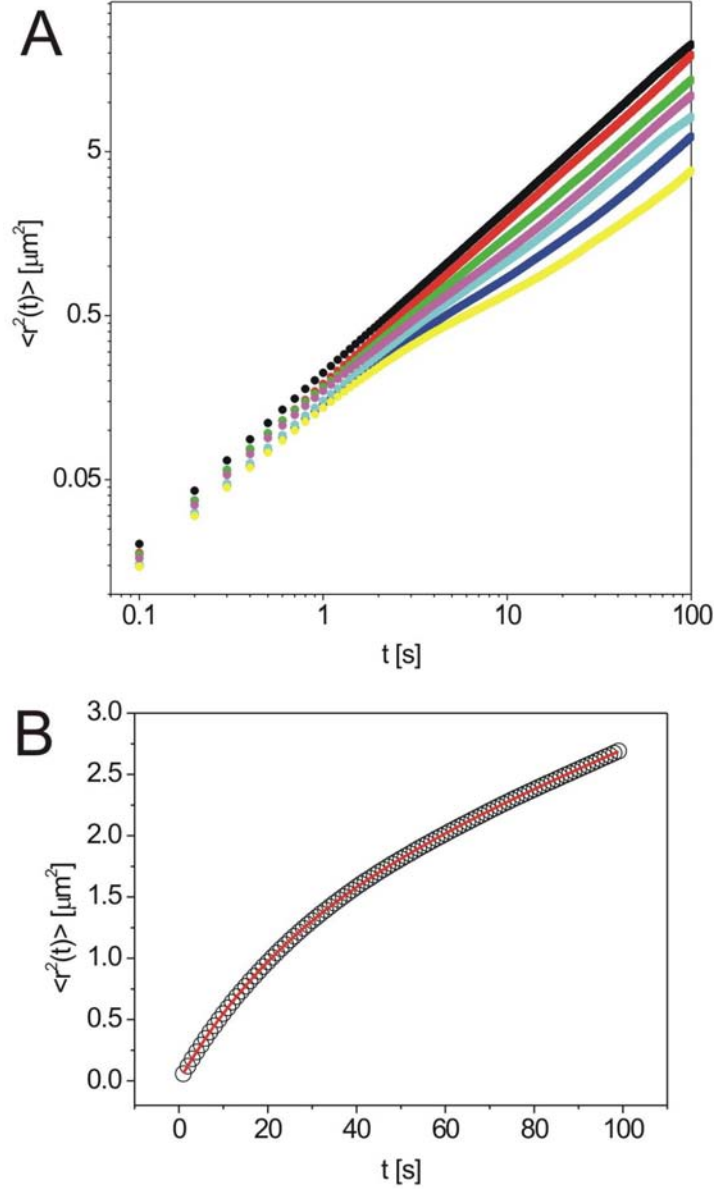


FIGURE 6.4. Mean-square displacement $\langle r^2(t) \rangle$ versus time for particles on a triangular lattice created by three interfering laser beams. A) Logarithmic representation for different potential strengths V_0 : the black, red, green, blue, cyan, magenta, yellow line correspond to $V_0 = 0, 0.5, 1, 1.5, 1.75, 2, 2.5 \cdot \text{const} \cdot k_B T$ with $\text{const} \approx 5$ (estimate, not measured). B) Mean-square displacement measured for highest potential strength versus time (symbols) and fit according to (6.11) (line).

To compare diffusion on non periodic substrates with diffusion on periodic substrates we now discuss mean-square displacements measured for colloidal particles on a triangular light potential at different $V_0/k_B T$. The mean-square displacements are shown in Figure 6.4A in double logarithmic representation. The black symbols represent free diffusion ($V_0/k_B T = 0$) serving as a reference. Similar to diffusion on quasicrystalline substrates, we find that short-time diffusion (D_S) transients into long-time diffusion ($D_L < D_S$) and that D_L becomes smaller upon increasing $V_0/k_B T$. However, we do not observe an intersecting subdiffusive regime. This can be understood in terms of the thermalization process discussed above; to thermalize on periodic substrates, particles have to explore only a single well and therefore display normal diffusive behavior.

There is an intriguing analogy between particle diffusion on triangular substrates and particle diffusion in spontaneous triangular crystals. In the latter case, an analytical expression for the mean-square displacement can be derived in the framework of the so-called single-exponential theory [128–130],

$$\langle r^2(t) \rangle = 4D_L t + 4(D_S - D_L) \left[1 - \exp\left(-\frac{t}{t_c}\right) \right]. \quad (6.11)$$

For $t \ll t_c$ the mean-square displacement is described by the short-time diffusion,

$$t \ll t_c : \quad \langle r^2(t) \rangle = 4D_S t, \quad (6.12)$$

and for $t \gg t_c$ by the long-time diffusion,

$$t \gg t_c : \quad \langle r^2(t) \rangle = \underbrace{4(D_S - D_L)}_{=const} + 4D_L t. \quad (6.13)$$

To demonstrate the analogy, we fitted the measured mean-square displacements associated with particle diffusion on triangular substrates to the analytical expression (6.11). Figure 6.4 exemplarily shows the fit and the corresponding measured data for $V_0/k_B T = 12.5$. At first glance, the excellent agreement appears to be coincidental, but an intuitive explanation can be provided; the transition from short-time to long-time diffusion arises from impeded particle diffusion and it is irrelevant if the impediment is caused by a triangular substrate or by nearest-neighbor particles in a free triangular crystal. The question arising here is whether such an analogy also exists between quasicrystalline substrates and many-particle systems exhibiting subdiffusive behavior such as glasses. Since an analytical expression corresponding to (6.11) has not yet been derived for such many-particle systems, systematic investigations of particle diffusion on quasicrystalline substrates might help to gain new insights. In addition, an analytical expression could serve for detailed quantitative studies on subdiffusion.

So far, our measurements do not allow for quantitative studies. Figure 6.5 exemplarily shows the long-time diffusion constant D_L versus the deepest potential well depth $V_0/k_B T$. As expected, D_L becomes smaller upon increasing $V_0/k_B T$. However, the measured data points clearly fail to uncover a functional dependence of D_L on $V_0/k_B T$.

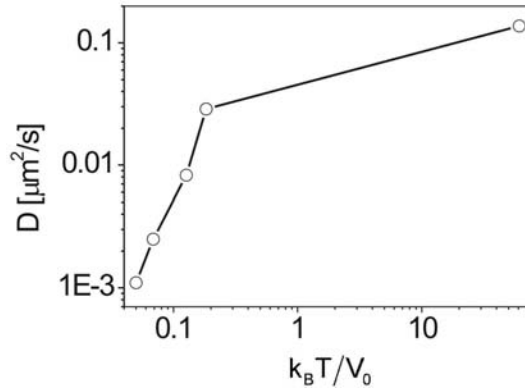


FIGURE 6.5. Long-time diffusion coefficient D_L versus depth V_0 of the deepest potential well evaluated from the measured mean-square displacements. In the theoretical work of Schmiedeberg and Stark, the temperature was varied and D_L was therefore plotted versus $k_B T / V_0$. To compare our data with the theoretical results, we have also chosen this representation.

The basic problem with quantitative investigations is that the substrate considered here is non periodic. Consequently, the number of possible initial conditions increases orders of magnitude compared to a periodic potential, and we therefore only scan a small range of possible initial conditions not representative of the whole set. As a result, the experimental data very sensitively depend on the initial conditions. Our experiments were therefore paralleled by numerical studies performed by Schmiedeberg and Stark. The dependence on initial conditions was investigated employing Brownian dynamics simulations and an analytical rate model, the latter yielding a functional dependence of D_L on $V_0/k_B T$. In addition to quasicrystalline pentagonal substrates, particle diffusion on random substrates was studied. In the following, we present the methods and results of this theoretical study.

6.4. THEORETICAL METHODS AND RESULTS

The theoretical work of Schmiedeberg and Stark is motivated by the studies on diffusive particle motion in a random potential performed by Lacasta et al. [117] and based on the Langevin equation

$$\begin{aligned} m\ddot{x} &= -\frac{\partial}{\partial x}V\left(\frac{x}{l}, \frac{y}{l}\right) - \gamma\dot{x} + \xi_x(t), \\ m\ddot{y} &= -\frac{\partial}{\partial y}V\left(\frac{x}{l}, \frac{y}{l}\right) - \gamma\dot{y} + \xi_y(t), \end{aligned} \quad (6.14)$$

The Langevin equation describes the motion of a particle (mass m) in a solvent (coefficient of friction γ). $V(x, y)$ denotes the external random potential of characteristic

length scale l . The $\xi_i(t)$ are white noise obeying the fluctuation-dissipation relation

$$\langle \xi_i(t)\xi_j(t') \rangle = 2\gamma k_B T \delta_{ij} \delta(t - t') \quad (6.15)$$

with k_B the Boltzmann constant and T the temperature. In the case of colloidal particles the diffusive motion is overdamped [66] and the inertial terms on the left-hand side of (6.14) can be neglected. Typically, the Langevin equation is solved through the use of numerical simulations with the white noise modeled by random kicks exerted on the particle. This method is known as Brownian dynamics simulation. The resulting trajectory $\mathbf{r}(t) = (r_x(t), r_y(t))$ allows evaluation of the mean-square displacement at time t according to (6.9).

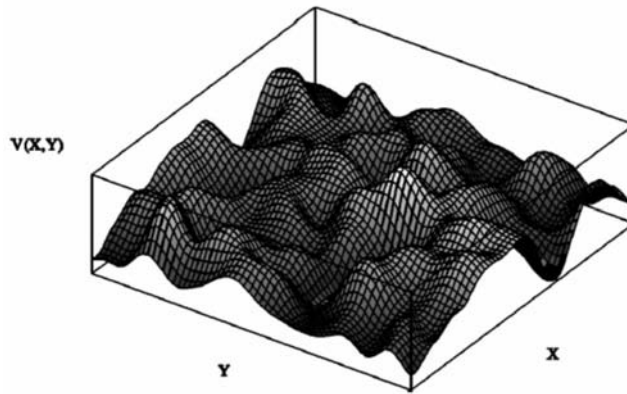


FIGURE 6.6. 3D visualization of a random potential $V(x, y)$ generated from a given spatial short-ranged correlation (6.17) (see text for details, plot copied from [117]).

We now focus on the potentials $V(\mathbf{r})$ used in [117] and employed by Schmiedeberg and Stark. In the first case, an algorithm was used to generate a random potential from a given spatial correlation [131, 132],

$$\langle V(\mathbf{r})V(\mathbf{r}') \rangle = \frac{\epsilon}{2\pi l^2} \exp\left(-\frac{|\mathbf{r} - \mathbf{r}'|^2}{2l^2}\right) \quad (6.16)$$

with ϵ the intensity parameter. An illustration of the created potential landscape $V(\mathbf{r})$ is provided in Figure 6.6. Subdiffusive motion was observed to arise at finite times t and remained over the entire simulation time corresponding to a time-range of several orders of magnitude. Indeed, subdiffusion persists for $t \rightarrow \infty$ in the case of (6.16) because the deepest well V_0 is singular; particles therefore thermalize on this substrate for $t \rightarrow \infty$ according to the interpretation of subdiffusion provided above and the subdiffusive regime does not transient into long-time normal diffusion at finite times $t_{eq} < \infty$.

Schmiedeberg and Stark considered a potential of finite depth, $V_0 < \infty$. While the potential minima were arranged regularly on a square lattice at multiples of the

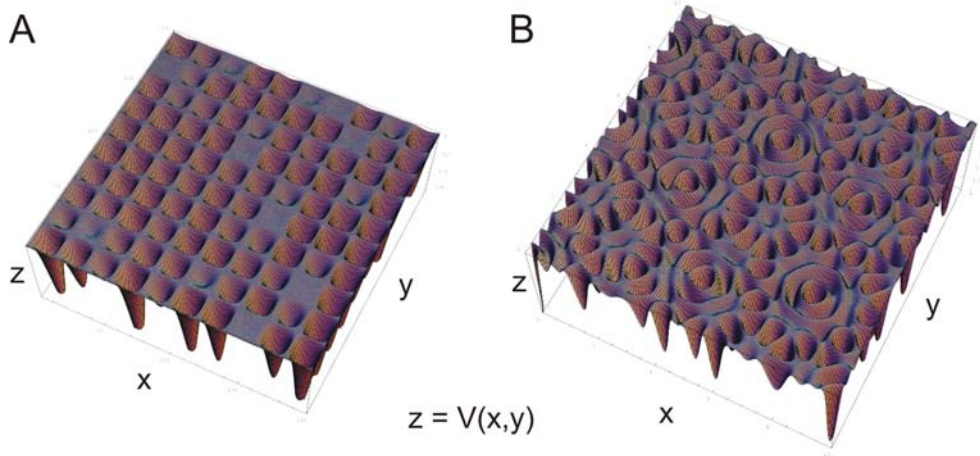


FIGURE 6.7. 3D visualization of A) a random and B) a quasicrystalline, pentagonal potential $V(x, y)$. A) The minima of the potential are located at a characteristic distance l from each other on a regular square grid. The depth V_m of the minima is generated randomly. B) The potential is created according to equation (6.17).

characteristic length scale l , the depths of the minima V_m were chosen randomly between $0 < V_m < V_0$ (see Figure 6.7A). In addition, simulations were performed for a quasicrystalline pentagonal potential (see Figure 6.7B) similar to the light-induced substrate employed in our experiments,

$$V(\mathbf{r}) = -\frac{V_0}{5} \left[\sum_{n=1}^5 \cos(\mathbf{G}_n \cdot \mathbf{r}) \right]^2. \quad (6.17)$$

The lattice vectors \mathbf{G}_n match the wave vectors \mathbf{K}_n (6.2). With (6.17), the distribution $p(V_m)$ of the potential minima V_m was determined (see Figure 6.8).

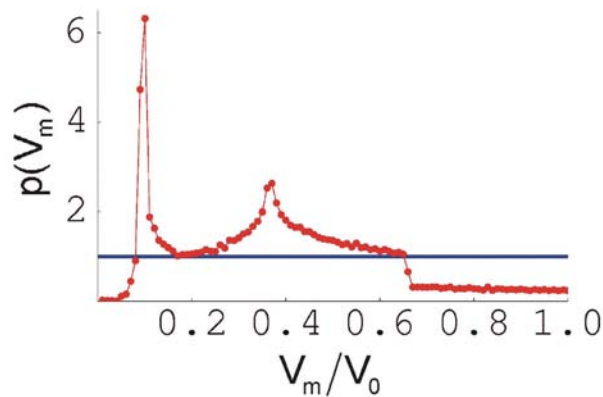


FIGURE 6.8. Distribution $p(V_m)$ of potential minima depths V_m for the quasicrystalline, pentagonal potential (6.17). V_0 denotes the largest minimum depth.

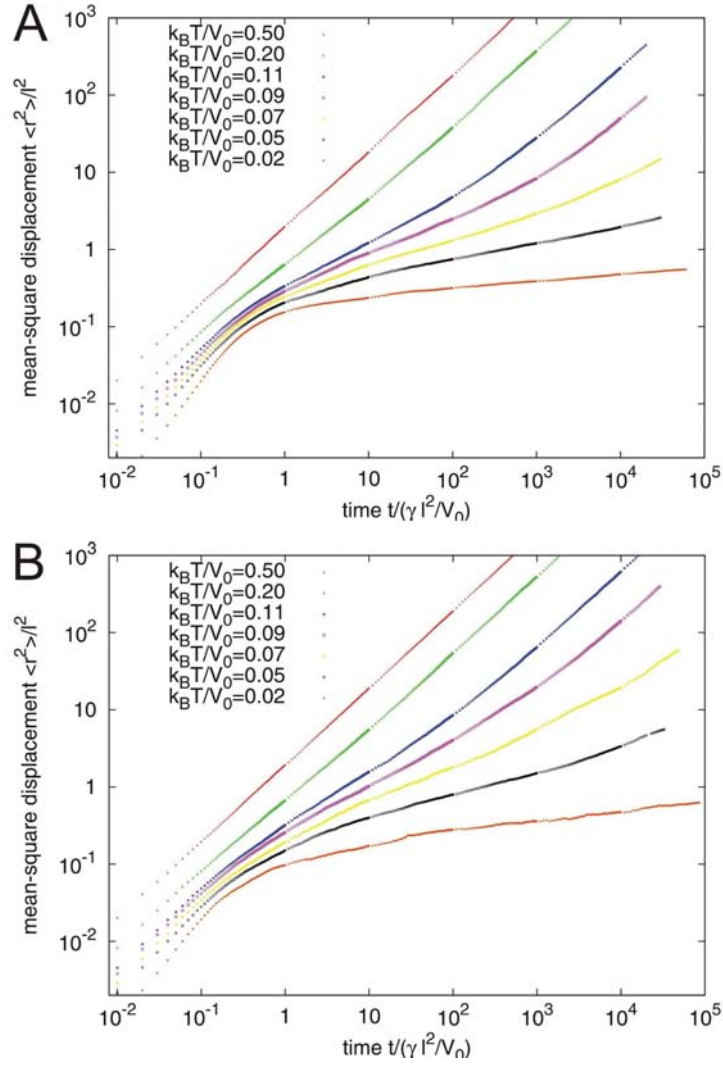


FIGURE 6.9. Mean-square displacement $\langle r^2(t) \rangle$ versus time t determined from the numerical solution $\mathbf{r}(t)$ of the Langevin equation (6.14). A) for the random potential and B) for the quasicrystalline potential (see Figure 6.7). l = characteristic length scale, V_0 = deepest well of the potential and γ = coefficient of friction. The ratio $V_0/k_B T$ was altered by varying the temperature T (see legends). Note that both $\langle r^2(t) \rangle$ and t are plotted logarithmically.

Figure 6.9A and B show the mean-square displacements obtained from Brownian dynamics simulations in the case of random square and quasicrystalline pentagonal substrates, respectively. The red curves correspond to the case where $V_0 = 0.5k_B T$. In this regime the diffusion is normal; particles do not feel the potential and therefore diffuse freely. Similar to our experimental results, a transition from normal short-time diffusion to long-time diffusion and an intersecting subdiffusive regime is observed upon increasing $V_0/k_B T$ (the temperature T was varied in the simulations). At first glance,

the theoretical results seem to confirm the experimental observation that short-time diffusion becomes smaller when $V_0/k_B T$ is increased; however, the mechanism is not the same. As has been mentioned above, the diffusion is lowered in the simulations by decreasing temperature.

In conclusion, the numerical results are in excellent qualitative agreement with the experimental results, but there is poor quantitative agreement. In particular, both the onset of subdiffusion and the transition from subdiffusion to long-time diffusion deviate in experiments and simulations. As mentioned above, this is caused by the large number of initial conditions due to the non-periodicity of the substrates considered here. In addition, non-periodicity might also avoid experimental observation of superdiffusion ($\nu > 1$). This is e.g. found numerically in the case of random square substrates for $k_B T/V_0 < 0.1$ (see Figure 6.9A). Superdiffusion arises from initial conditions because particles diffuse faster than normal if located close to a potential maximum at the initial time.

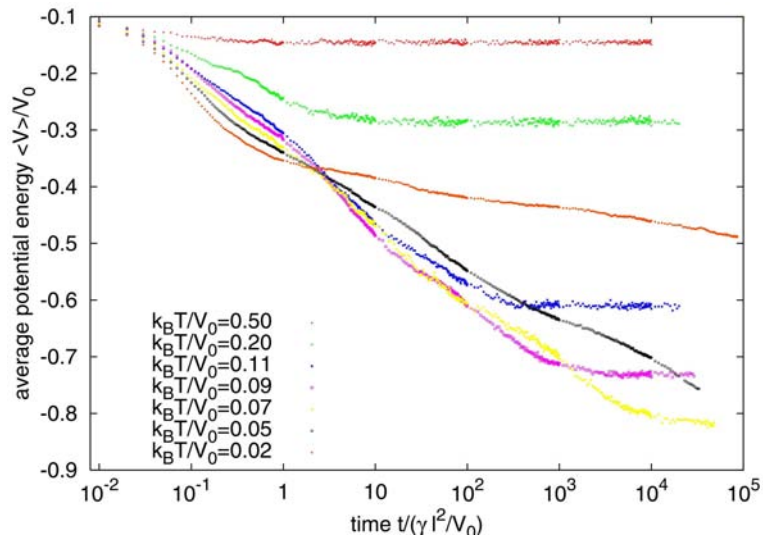


FIGURE 6.10. Averaged potential energy $\langle V \rangle$ of a particle subjected to a quasicrystalline pentagonal potential versus time in dimensionless units for different depths V_0 of the deepest well (see legend). $\langle V \rangle$ first decreases and then saturates reflecting the relaxation process and thermal equilibrium, respectively.

In addition to mean-square displacements, the Brownian dynamics simulations provide a nice illustration of the thermalization process associated with subdiffusion. In Figure 6.10 the average potential energy $\langle V \rangle$ of particles on random square substrates is plotted versus time. While particles thermalize on the substrate, $\langle V \rangle$ decreases continuously and finally saturates after the equilibrium state has been reached. As can be seen, the thermalization time clearly becomes larger upon increasing $V_0/k_B T$.

In addition to numerical simulations, Schmiedeberg and Stark attempted to approach the diffusive motion of particles on random and quasicrystalline substrates by means of the rate equation

$$\frac{d}{dt}P(V_m, t) = -z\Gamma(V_m)P(V_m, t) + \underbrace{\frac{z}{V_0} \int_0^{V_0} dV'_m \Gamma(V'_m) P(V'_m, t) p(V'_m)}_{=\frac{4}{l^2} D(V_0, t)}. \quad (6.18)$$

$P(V_m, t)$ denotes the probability for a particle to occupy a minimum with a depth between V_m and $V_m + dV_m$ at time t . z is the average number of nearest neighbor wells and $\Gamma(V_m)$ describes the rate with which the particle escapes from a well of depth V_m . Here, the famous Kramers rate was used [133],

$$\Gamma(V_m) = \frac{\pi V_m}{\gamma l^2} \exp\left(-\frac{V_m}{k_B T}\right). \quad (6.19)$$

Note that (6.19) is a simplified version because it does not take into account the well the particle jumps to. The rate equation (6.18) therefore is an approximate description which can be interpreted as follows. $P(V_m, t)$ is diminished by particles escaping from wells with a depth V_m (first term on the right hand side of (6.18)). In contrast, $P(V_m, t)$ increases due to the particles jumping from all $p(V'_m)$ (see Figure 6.8) wells with a depth V'_m into the wells with a depth V_m (second term in (6.18)). The correlation of this second contribution to the diffusion constant D and the characteristic length scale l can be derived from the real-space representation of the rate equation (6.19) (see [134, 135] for a detailed discussion). It is intuitively clear, however, that $P(V_m, t)$ increases with D (particles diffuse faster) and decreases with l (larger distance between the minima). An interesting prediction is obtained in the limit $t \rightarrow \infty$ where a stationary distribution of the particles, $\frac{d}{dt}P(V_m) \rightarrow 0$ is assumed. In this case it follows that

$$D_\infty(V_0) = \lim_{t \rightarrow \infty} D(V_0, t) = \frac{z l^2}{4} \left(\int_0^{V_0} \frac{dV'_m}{\Gamma(V'_m)} \right)^{-1} \implies D_\infty(V_0) \propto \exp\left(-\frac{V_0}{k_B T}\right) \quad (6.20)$$

Consequently, the diffusion constant is expected to decay exponentially with the depth V_0 of the deepest well at large times. As a final remark it should be mentioned that the average numbers of nearest neighbors z is known in the case of quasicrystalline pentagonal substrates ($z = 6$) yet the number of nearest neighbors is not identical for each minimum. This therefore emphasizes the approximative nature of the rate equation.

Figure 6.11 shows D_∞ versus V_0 . The analytical expression (6.20) is represented by the red and blue lines in the case of random square and quasicrystalline pentagonal substrates, respectively. To check the analytical expression (6.20), D_∞ was determined from Brownian dynamics simulations as well (red and blue symbols). As can be seen, the analytical model based on the rate equation (6.18) is confirmed excellently by the

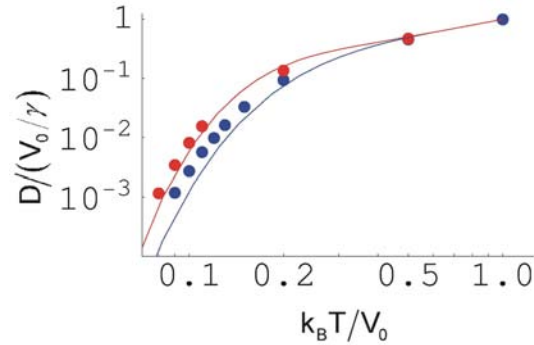


FIGURE 6.11. Long-time diffusion coefficient D_L versus the depth V_0 of the deepest potential well in the case of random (blue) and quasicrystalline pentagonal substrates (red). The symbols represent the results obtained from Brownian dynamics simulations and the solid lines correspond to the approximate analytical expression (6.20) derived from the rate-equation (6.18).

numerical results. Accordingly, rate equations provide a promising method to analytically describe subdiffusive motion. In addition, the theoretical results show good qualitative agreement with the experimental data (see Figure 6.5).

6.5. CONCLUSIONS AND OUTLOOK

We have performed experimental studies on single-particle diffusion in the presence of a quasicrystalline pentagonal light potential. The measured mean-square displacements exhibit an intermediate range of subdiffusive behavior which grows with increasing depth V_0 of the deepest well. Our results demonstrate that subdiffusion is associated with a thermalization process; a particle must explore the whole range of potential well depth to reach thermal equilibrium. In addition, we investigated particle diffusion on periodic triangular substrates. As a result, we do not observe subdiffusive motion due to periodicity, i.e. $V_0 = const.$ Moreover, particle diffusion on triangular substrates exhibits an intriguing analogy to particle diffusion in free triangular crystals. With this, we intend to discover an analogy between particle diffusion on quasicrystalline substrates and particle diffusion in many-particle systems exhibiting subdiffusive behavior such as glasses.

We compared our experimental data with results based on both Brownian dynamics simulations and analytical rate equations and we observe good qualitative agreement. However, experimental and theoretical results show quantitative deviations caused by the non-periodicity of the substrates considered here; the number of initial conditions increases orders of magnitude compared to periodic substrates and it is therefore not possible to measure a representative set of initial conditions.

There is another very interesting feature of quasicrystals left to explore. In addition to phononic excitations, quasicrystals exhibit so-called phasons as well [136]; in brief, a

phase factor depending on the position \mathbf{r} is added to the potential (6.17),

$$V(\mathbf{r}) = \frac{V_0}{5} \left[\sum_{n=1}^5 \cos(\mathbf{G}_n \cdot \mathbf{r} + \phi_n(\mathbf{r})) \right]^2, \quad (6.21)$$

with

$$\phi_n(\mathbf{r}) = \mathbf{G}_n \cdot \mathbf{u}(\mathbf{r}) + a\mathbf{G}_{3n \bmod 5} \cdot \mathbf{w}(\mathbf{r}). \quad (6.22)$$

The first term represents the phonons ($\mathbf{u}(\mathbf{r}) =$ displacement field) and the second one the phasons. Intuitively, the phason degree of freedom arises because a change of the phases $\phi_n(\mathbf{r})$ also leads to a modification of the potential shape in the case of quasicrystalline substrates. As a result, we expect the diffusive behavior to be different if phasonic excitations are present. Experimentally, phasons will be generated by a set of piezo-driven mirrors which will allow control of the $\phi_n(\mathbf{r})$ and creation of single phasons $\mathbf{w}(\mathbf{r})$ [137].

7

New insight on the nature of confinement-induced like-charge attraction

ABSTRACT

It is well known that liked-charged colloidal particles repeal each other. However, since 1994, several groups independently found an unusual long-ranged attractive component in the pair interaction if colloidal suspensions are confined in thin sample cells. Despite of considerable theoretical and experimental effort, this so-called like-charge attraction (LCA) has not yet been explained. Here, we reinvestigate the pair potential of like-charged colloidal particles with video microscopy and demonstrate that LCA arises from an optical artifact leading to erroneous distance measurements. We also provide methods and techniques which allow to avoid or at least to correct for optical artifacts. In addition, we address a light-induced effect termed optical binding and causing attractive contributions to colloidal pair interactions. Similar to LCA, optical binding has been subject to controversial discussions; we, however, demonstrate that optical binding indeed exists.

7.1. INTRODUCTION

The pair interaction in bulk charge-stabilized colloidal suspensions is known to be well described by the Derjaguin Landau Verwey Overbeek (DLVO) theory [138, 139]. Within this theory, the pair interaction arises from a hard core contribution for particle distances smaller than the particle diameter, the short-ranged van-der-Waals interaction (2.6) for distances typically smaller than 100nm and the repulsive Yukawa potential (2.10). The DLVO theory has been verified experimentally by dynamical [140] and equilibrium measurements [40, 141, 142].

Doubts arose in 1994 when Ito et al. [143] observed void formation in intrinsically homogeneous latex polymer dispersions. In addition, Kepler et al. simultaneously reported an anomalous long ranged attraction in colloidal dispersions under confined conditions – i.e., the spacing between the sample’s top and bottom wall is slightly larger than the particle diameter [39]. The existence of this so-called *confinement-induced* like-charge attraction (LCA) was manifested two years later when Larsen et al. found metastable crystallites [144, 145]. Note that confinement-induced LCA is observed in the case of monovalent ions and only in the presence of *two* confining glass plates.

Systematic studies on confinement-induced LCA were started in 1996 when Crocker et al. extracted pair interactions from the dynamics of two colloidal particles under confined conditions [146]. Squires et al. thereupon demonstrated in their calculations that the attraction arises from a non-equilibrium hydrodynamical effect [147]. However, this mechanism cannot explain the observation of confinement-induced LCA in equilibrium; several groups independently measured the pair distribution function $g(r)$ of a dilute equilibrated colloidal system and then extracted the pair interaction through the use of closure relations (see Section 2.4) [39, 41, 148–151]. To manifest the existence of confinement-induced LCA, elaborate numerical cross-checks were performed [149] employing computer simulations and approximate liquid state theories [128, 152–154]. In addition, it has been repeatedly investigated how confinement-induced LCA depends on parameters as type, charge or size of colloidal particles. As a result, no systematic dependence has been discovered.

The experimental evidence of confinement-induced LCA motivated plenty of theoretical studies. In the meanwhile, the existence of attractive pair interactions within mean-field theories is categorically ruled out by rigorous mathematical proofs [155–159]. The studies beyond mean-field theories mostly focused on ion correlations [158, 160–166], i.e. the mechanism inducing LCA in polyelectrolytes [167]. Although an attraction has been found, none of the theoretical approaches reproduces the long-ranged nature of confinement-induced LCA. Recently, it has been proposed that confinement-induced LCA might be caused through violations in ionic charge neutrality [24, 168]. However,

this explanation is speculative and confinement-induced LCA therefore still constitutes a mystery in colloidal science.

This chapter is organized as follows: to provide a more detailed introduction to confinement-induced LCA, we summarize the latest experimental publication on this topic [24] in Section 7.2. We then describe our experimental method to measure pair interactions and optical artifacts in Section 7.3. Next, Section 7.4 contains the description and discussion of our results. In Section 7.5, we discuss methods and techniques which allow to avoid optical artifacts. Section 7.6 addresses an effect termed optical binding which has to be ruled out to occur in our experiments. We finally conclude the chapter in Section 7.7.

7.2. EXPERIMENTAL EVIDENCE OF CONFINEMENT-INDUCED LCA

In the following, we exclusively focus on confinement-induced LCA and therefore omit “confinement-induced”. We now provide a summary of Grier’s and Han’s experimental study [24] on LCA. A dilute system of colloidal particles suspended in water was confined between two glass plates and particle trajectories were recorded with video microscopy (see Figure 7.1A). From the trajectories, the radial distribution function $g(r)$ was evaluated and the pair-interaction was determined employing both the hypernetted chain (2.17) and the Percus-Yevick equations (2.18) to obtain reliable results. To explore the role of confinement more systematically, Grier and Han varied the spacing H between the two confining glass plates of their sample. This was achieved through application of gas pressure. The evaluated pair potentials are shown in Figure 7.1B. For the largest spacing, $H \approx 123\sigma$ ($\sigma = 1.58\mu\text{m}$), the pair potential is purely repulsive and in perfect agreement with Poisson-Boltzmann theory (see Section 2.4); the pair potential, however, displays the onset of an attraction at $H \approx 12\sigma$. Decreasing the spacing further to $H \approx 2\sigma$, the minimum is finally shifted to a smaller distance of approximately 1.3σ and the depth is increased to approximately $0.3k_B T$. In addition, the repulsive core of the measured pair potential shifts to smaller distances. Grier and Han assumed that the shift is associated with the decrease of the screening length arising from the enlarged concentration of counter ions caused by the reduced sample volume; however, the change in the slope of the repulsive core is highly non-systematic and Grier and Han therefore canceled the idea that LCA might be related to the counter ion concentration mediated by the spacing of the confining glass plates. The interpretation of the results was then based on studies performed in the framework of Debye-Hückel theory revealing that correlations between macroions and simple ions can generate local violations of electroneutrality, therefore leading to an attractive contribution to the pair potential [165, 166]. The theoretical and experimental findings, however, display poor quantitative agreement. As a consequence, Grier and Han finally speculated that the counterion distribution’s electroneutrality might be violated in such a manner that

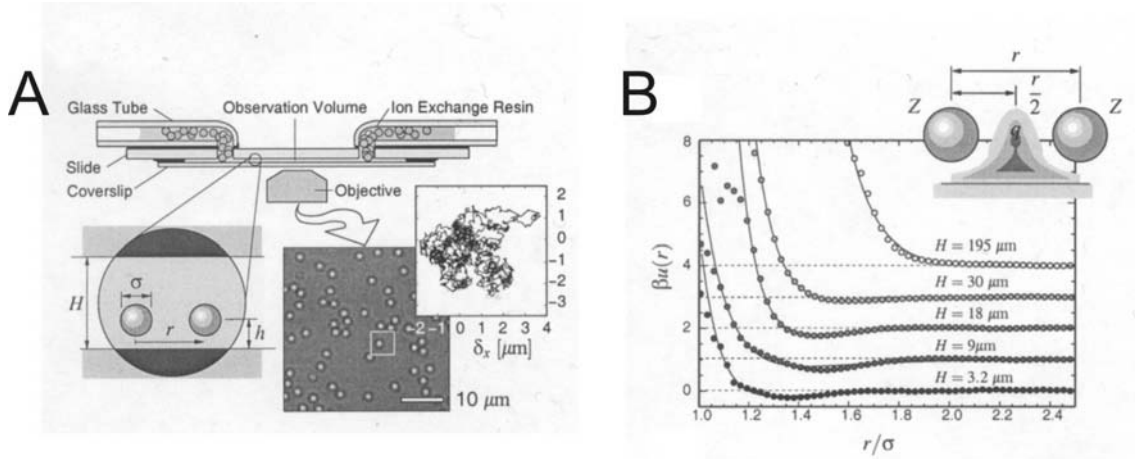


FIGURE 7.1. A) Experimental setup used by Grier and Han [24]. The plot on the right hand side depicts a typical trajectory of a single colloidal particle recorded by means of videomicroscopy. B) Measured pair potentials for different sample heights H (symbols). The solid lines are fits according to the space charge model sketched in the upper right corner. Plots taken from [24].

a space charge is induced right in between two macrions (see illustration in the upper right corner of Figure 7.1B). The attraction was assumed to be of the form (2.10) where one macroion is replaced by the point-like space charge. The corresponding fits are shown in Figure 7.1B as solid lines and yielded a space charge of approximately 10 elementary charges.

In conclusion, confinement-induced LCA still constitutes a mysterious effect although Grier and Han spent quite some effort on improving the resolution. It finally dropped down to $1/20k_B T$ as the thermodynamic self-consistency was checked (see Section 5 in [24] and references therein). Accordingly, the experimental results bear strong evidence for like-charge attraction to exist.

7.3. EXPERIMENTAL METHOD AND DATA ANALYSIS

Motivated by the still hidden nature of LCA, we have performed studies on the subject as well. Our experimental method and data analysis are described in the following.

We used samples of type I and II (see Section 3.5) to measure colloidal pair interactions under unconfined and confined conditions, respectively. To compare our results with those obtained by other groups, we have chosen the same batch of colloidal particles which had been also used in [41] (highly charged silica spheres of diameter $\sigma = 1.5 \pm 0.08 \mu\text{m}$). As a major difference, we did not apply the standard inversion procedures which determine the pair interaction $u(r)$ by inverting the pair distribution function $g(r)$ of semi-dilute suspensions (see Section 2.4). Since it has been shown that inversion procedures do not always produce reliable results [169,170], we evaluated

the pair interaction directly by measuring the distance probability distribution of two colloidal particles as described in the following.

We subjected two colloidal particles to a well-defined radially symmetric light potential $u_{ext}(\mathbf{x})$. In terms of the formalism introduced in Section 3.1, the potential was created with a single, slightly defocussed laser beam aligned to $\mathbf{X} = \mathbf{0}$ (see Section 3.1.4). From the particle trajectories as measured by digital video microscopy (see Section 3.2), we obtained the distribution function $P(\mathbf{x}_1, \mathbf{x}_2)$ with \mathbf{x}_i the position of particle $i = 1, 2$. In the central region of the light trap $u_{ext}(\mathbf{x})$ is approximated very well by a parabolic potential,

$$u_{ext}(\mathbf{x}) = a_{ext}|\mathbf{x}|^2 \quad (7.1)$$

and the total potential energy of the two particles therefore becomes

$$V_{tot} = a_{ext}|\mathbf{x}_1|^2 + a_{ext}|\mathbf{x}_2|^2 + u(r), \quad (7.2)$$

where $r = |\mathbf{x}_1 - \mathbf{x}_2|$. We introduce center of mass coordinates,

$$\mathbf{R} = \frac{1}{2}(\mathbf{x}_1 + \mathbf{x}_2), \quad \mathbf{r} = \mathbf{x}_1 - \mathbf{x}_2, \quad (7.3)$$

which allows to write the total potential energy as

$$V_{tot} = V(R) + V(r) \quad (7.4)$$

with $V(R)$ and $V(r)$ defined as

$$V(R) = 2a_{ext}R^2, \quad V(r) = u(r) + \frac{a_{ext}}{2}r^2. \quad (7.5)$$

Since the center of mass motion decouples from the relative particle motion, a_{ext} and $u(r)$ can be obtained simultaneously by inverting the corresponding Boltzmann factor,

$$\frac{a_{ext}R^2}{k_B T} = -\ln P(R), \quad \frac{u(r)}{k_B T} = -\ln P(r) - \frac{a_{ext}}{2}r^2 \quad (7.6)$$

where $P(R)$ and $P(r)$ denote the probability distributions of the center of mass and the relative coordinate, respectively (otherwise the external potential first must be determined by the probability distribution of a single colloidal particle inside the laser trap [142]).

The data analysis is performed as follows: first, the trajectories $\mathbf{x}_1(t)$ and $\mathbf{x}_2(t)$ are transformed to center of mass coordinates $\mathbf{R}(t)$ and $\mathbf{r}(t)$ according to (7.2). Both, the center of mass coordinate $\mathbf{R}(t) = (R_x(t), R_y(t))$ and the relative coordinate $\mathbf{r}(t) = (r_x(t), r_y(t))$ are then transformed to polar coordinates $(R(t), \theta_R(t))$ and $(r(t), \theta_r(t))$, respectively,

$$R_x(t) = R(t) \cos \theta_R(t), \quad R_y(t) = R(t) \sin \theta_R(t), \quad (7.7)$$

$$r_x(t) = r(t) \cos \theta_r(t), \quad r_y(t) = r(t) \sin \theta_r(t). \quad (7.8)$$

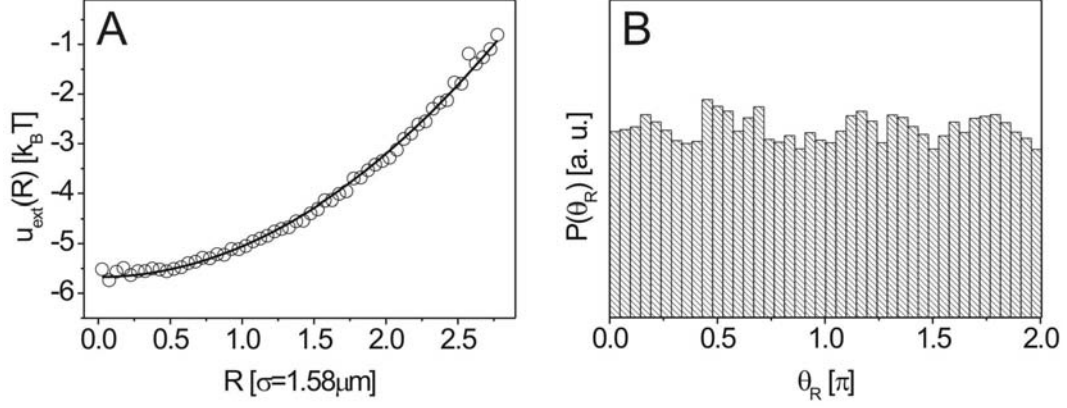


FIGURE 7.2. A) Light potential u_{ext} determined from the measured center of mass distribution (symbols). The solid line is a parabolic fit. B) Distribution $P(\theta_R)$ of the angular coordinate θ_R associated with the center of mass $\mathbf{R} = R(\cos \theta_R, \sin \theta_R)$. With this, one can check if the light potential is radially symmetric.

With this, we determine the probability distribution functions $P_m(R)$, $P_m(r)$, $P_m(\theta_R)$, and $P_m(\theta_r)$ (m =measured), the two latter allowing one to check if the light potential is radially symmetric ($P_m(\theta_R) = const$ and $P_m(\theta_r) = const$). Because of

$$P_m(\mathbf{x}_1, \mathbf{x}_2) d\mathbf{x}_1 d\mathbf{x}_2 = \left(P_m(R) 2\pi R dR \right) P_m(\theta_R) d\theta_R \left(P_m(r) 2\pi r dr \right) P_m(\theta_r) d\theta_r, \quad (7.9)$$

$P_m(R)$ and $P_m(r)$ have to be normalized by the respective factors $2\pi R$ and $2\pi r$. The pair interaction is finally obtained as

$$\begin{aligned} \frac{u(r)}{k_B T} &= -\ln \left(\frac{P_m(r)}{2\pi r} \right) - \frac{a_{ext}}{2} r^2, \\ a_{ext} &= -\frac{k_B T}{2R^2} \ln \left(\frac{P_m(R)}{2\pi R} \right). \end{aligned} \quad (7.10)$$

Figure 7.2A demonstrates the parabolic shape of the measured light potential. In Figure 7.2B, the angular coordinate distribution $P(\theta_R)$ is plotted; the distribution is approximately constant and therefore verifies the radial symmetry of the light potential.

To rule out possible light-induced effects such as optical binding we repeated the pioneering experiment of Burns et al. [171]. We demonstrate in Section 7.6 that at least laser powers of $0.5W$ are required to induce optical binding; the laser powers however were less than $50mW$ in our experiments on LCA.

It is well known and confirmed by numerical calculations [172] that images of colloidal particles are typically much larger than their geometrical size and it has already been noticed by other groups that the overlap of particle images leads to wrong distance measurements at short distances [173]; however, this has not yet been investigated systematically and the impact on measured pair interactions is therefore unclear. We

provide a quantitative measurement of the deviation between the measured and the true distance denoted by $r_m(t)$ and $r(t)$, respectively. The measurement is performed as follows: as an immobile reference position we selected an isolated particle which was irreversibly stuck (due to van der Waals forces) to the substrate and determined its probability distribution. Due to the finite experimental resolution, the theoretically expected delta-like probability distribution is broadened by approximately $20nm$ and the maximum is identified as the true particle position $(\bar{x}_{ref}, \bar{y}_{ref})$. Next, we approached a mobile particle with a laser trap and determined for each video frame the momentary position of the immobile reference particle $(x_{ref}(t), y_{ref}(t))$. Note, that in contrast to $(\bar{x}_{ref}, \bar{y}_{ref})$ the position $(x_{ref}(t), y_{ref}(t))$ is obtained in the presence of another particle. With this, we first calculated the momentary, i.e. the measured distance

$$r_m(t) = \sqrt{(x_{ref}(t) - x(t))^2 + (y_{ref}(t) - y(t))^2}. \quad (7.11)$$

As a quantitative measure of how overlapping particle images modify their measured distance we introduce

$$\Delta r(t) := r_m(t) - \sqrt{(x(t) - \bar{x}_{ref})^2 + (y(t) - \bar{y}_{ref})^2}. \quad (7.12)$$

It is immediately obvious that the temporal average of this expression is zero if the position of the isolated particle is not modified by the presence of another close particle, i.e.

$$(\bar{x}_{ref}, \bar{y}_{ref}) = \langle (x_{ref}(t), y_{ref}(t)) \rangle \implies \langle \Delta r(t) \rangle = 0 \quad (7.13)$$

where the outer bracket corresponds to time averaging. Since both particles are affected symmetrically by the image distortion, the true particle distance $r(t)$ is obtained by

$$r(t) = r_m(t) - 2\Delta r(t). \quad (7.14)$$

We corrected the raw data $\{r(t)\}$ according to (7.14) and then determined the pair interaction from the true distance probability distribution $P(r)$ according to (7.10). Note that the image distortion has no impact on the center of mass coordinate because due to symmetry reasons the positions of the two particles are shifted in opposite direction along their distance vector \mathbf{r} .

7.4. RESULTS AND DISCUSSION

The open symbols in Figure 7.3 represent the measured pair potential under confined conditions (sample type II). In addition to the strong repulsion close to contact, we find a shallow minimum with a depth of approximately $0.2k_B T$ at $r_m \approx 1.3\sigma$ which is in excellent agreement with the characteristic features of LCA (see Figure 7.1). In the following, we will present our measurements of $\Delta r(t)$ which demonstrate that the occurrence of such a minimum must not be interpreted as an attractive component in the pair interaction, but instead is the result of errors in distance measurements.

In Figure 7.4A and C, we plotted the measured $\Delta r(t)$ versus time t . The particles were far apart from each other ($\approx 10\sigma$) in Figure A so that particle images did not overlap. As expected, $\Delta r(t)$ scatters within our resolution around zero and thus demonstrates that video microscopy yields accurate positional information. In contrast, the fluctuations are doubled when the two particles are close to contact (Figure C). Here, the overlapping particle images obviously affect the determination of particle distances. To demonstrate that distance measurements suffer from systematic distortions, we plotted Δr vs. the measured distance r_m as shown in Figure 7.5. As can be seen, Δr is negative for distances between $r_m \approx 1.2\sigma$ and $r_m \approx 1.8\sigma$. Here, the measured distance r_m is smaller than the true distance r according to the definition (7.14). In contrast, the measured distance is too large for distances smaller than $r_m \approx 1.2\sigma$. We smoothed the measured $\Delta r(r_m)$ and corrected our raw data according to (7.14). The pair potential evaluated from the corrected data set is plotted in Figure 7.3 as closed symbols. Indeed, the apparent attractive component has disappeared and the measured pair interaction can be even fitted to the Yukawa potential (2.10) with $Z \approx 8000 \pm 4000$ and $\kappa^{-1} \approx 10 \pm 5nm$.

The effect of optical distortions on measured pair potentials is evident; it is, however, intriguing that deviations of approximately 0.01σ in distance measurements lead to apparent attractions of approximately $0.1k_B T$. To understand this we consider the relation between the measured $P_m(r_m)$ and the true distance probability distribution

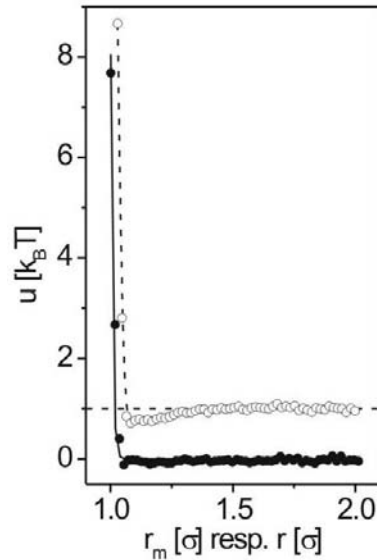


FIGURE 7.3. Measured pair potentials vs. the measured (open symbols) and the corrected (closed symbols) particle distance. The data are shifted in vertical direction for clarity. The solid line corresponds to a least-mean-square fit to the screened Coulomb potential (2.10) with fit parameters $Z \approx 8000 \pm 4000$ and $\kappa^{-1} \approx 10 \pm 5nm$.

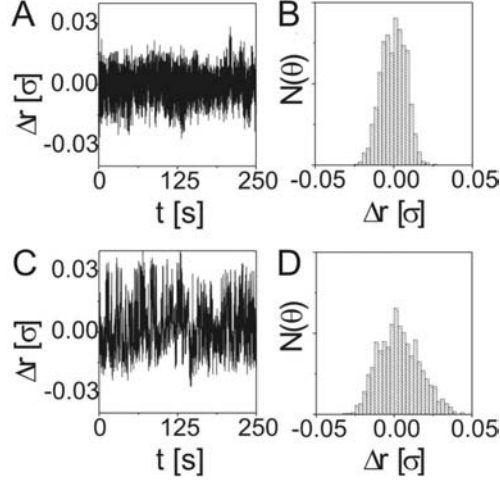


FIGURE 7.4. $\Delta r(t)$ between a fixed and a free fluctuating particle under confined conditions determined by video microscopy A) for large and C) for small particle distances. B), D) Corresponding histograms of the measured distance fluctuations.

$P(r)$,

$$P_m dr_m = P(r) dr \quad (7.15)$$

with dr_m and dr the bin sizes associated with $P_m(r_m)$ and $P(r)$, respectively. With this, it follows that

$$P(r) = P_m(r - 2\Delta r(r)) \left[1 + 2 \frac{d}{dr} \Delta r(r) \right], \quad (7.16)$$

$$P_m(r_m) = P(r_m + 2\Delta r(r_m)) \left[1 - 2 \frac{d}{dr_m} \Delta r(r_m) \right]. \quad (7.17)$$

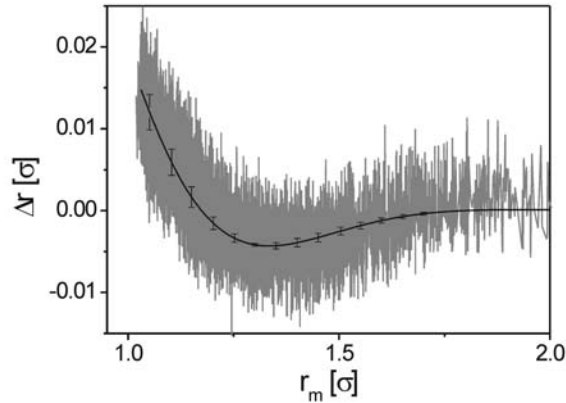


FIGURE 7.5. Δr vs. r_m determined numerically (black solid line) and experimentally (gray solid line). The error bars indicate the change of Δr upon variation of the applied intensity threshold for particle detection by $\pm 10\%$.

Hence, the optical distortions do not only cause a shift of the distance probability distribution but also affect bin sizes which finally causes the crucial modification of measured pair interactions.

To explore the origin of optical distortions we performed numerical calculations mimicking the particle detection used in our experiments and based on a typical snapshot of a transparent colloidal particle under bright field illuminating conditions (see inset of Figure 7.6). The bright central spot and the darker ring around the particles are typical for images of transparent colloids and are in good agreement with the results of other authors [150, 174, 175]. From the digitized intensity distribution we calculated a cross section of the intensity distribution (symbols in Figure 7.6). The solid line is an (arbitrary) analytical expression $I(x)$ which was chosen to yield best agreement with our experimental data. As can be seen the intensity has a maximum at the particle center and rapidly decays in radial direction. It is important to realize that before the intensity reaches a constant background level it falls below this value around $x \approx 0.5\sigma$. When comparing the spatial extension of the intensity distribution with the geometrical size of the particle, it is also obvious that the particle image is blurred over almost twice the sphere diameter σ . Due to the radial symmetry of the problem, from $I(x)$ one easily obtains the corresponding 2D one-particle intensity distribution $I_{1P}(x, y)$. Both, the undershooting of the intensity below the background and the (compared to σ) enlarged optical image of the particles are in qualitative agreement with calculations of Ovrzyn who made a complete numerical analysis of the imaging of transparent colloidal spheres. By means of Mie theory calculations he computed the electromagnetic field

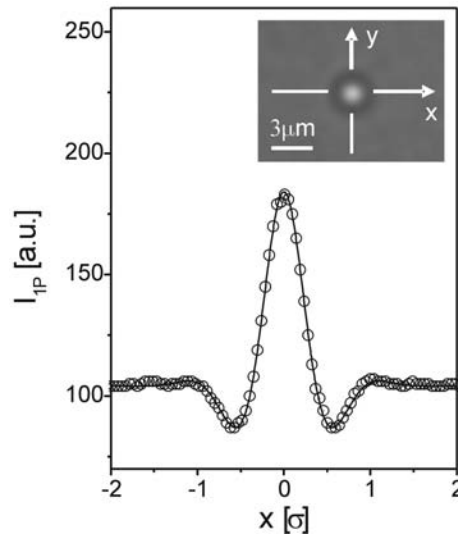


FIGURE 7.6. Cross section of the intensity distribution of a transparent colloidal particle derived from the image in the inset. Experimental data (symbols) and arbitrary analytical fit function (solid line). Inset: typical snapshot of a colloidal particle observed by video microscopy.

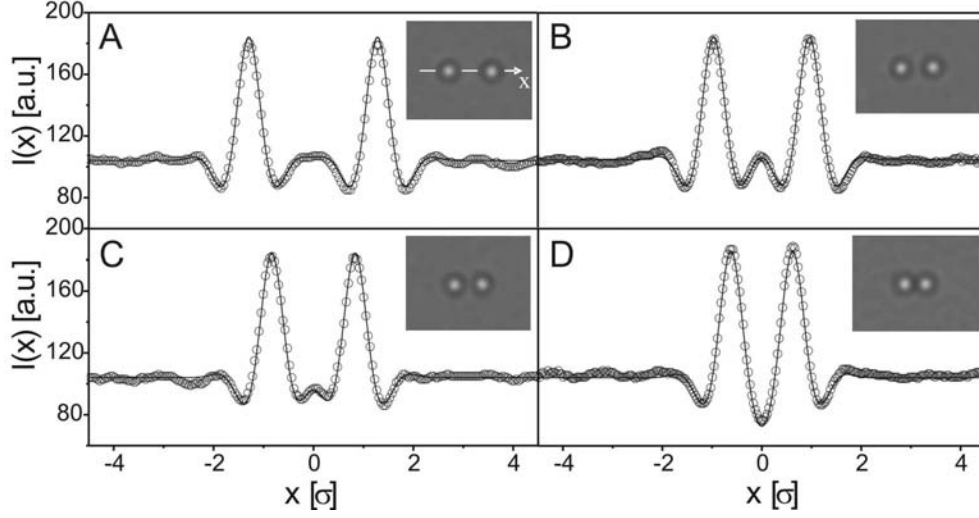


FIGURE 7.7. Intensity cross sections of two particle images for different measured distances r_m : A) $r_m = 2.58\sigma$, B) $r_m = 1.93\sigma$, $r_m = 1.67\sigma$ and D) $r_m = 1.25\sigma$. The symbols represent experimental data and the solid lines refer to numerical calculations. Insets: corresponding video snapshots.

scattered under plane wave illumination conditions by a spherical particle and how it is transmitted through a high numerical aperture microscope to a detector [172, 176]. The open symbols in Figure 7.7 correspond to the intensity cross-section taken from a snapshot (inset of Figure 7.7) of two silica particles close to contact. In contrast to Figure 7.6, in the presence of a second colloidal sphere the intensity distribution becomes slightly asymmetric around the particle centers. This is different compared to Figure 7.6. Assuming that the optical image of a particle pair follows from a linear superposition of single-particle images (incoherent image formation) the intensity distribution of two colloids with center-to-center distance r is given by

$$I_{2P}(x, y; r) = I_{1P}(x - r/2, y) + I_{1P}(x + r/2, y) - I_0, \quad (7.18)$$

where I_0 accounts for the background intensity. The solid lines in Figure 7.7 correspond to the cross-sections $I_{2P}(x, y = 0; r)$. The excellent agreement with the experimental data clearly demonstrates that under our illumination conditions a linear superposition yields accurate results. Having obtained an analytical expression for I_{2P} we now can calculate optical images for different particle distances r . From these images we obtain the optically determined particle center distances r_m through mimicking the image processing algorithm used in our experiments. After subtraction of a uniform threshold T we calculate the intensity weighted centroids of the two particles within the areas defined by $I_{2P}(x, y; r) \geq T$ [89]. From this we obtain the difference between the (via digital video microscopy) measured and the true particle distance according to (7.14). The results are plotted in Figure 7.5 as solid line versus r_m . As can be seen the calculated distortion is in excellent agreement with the measured data. The error bars

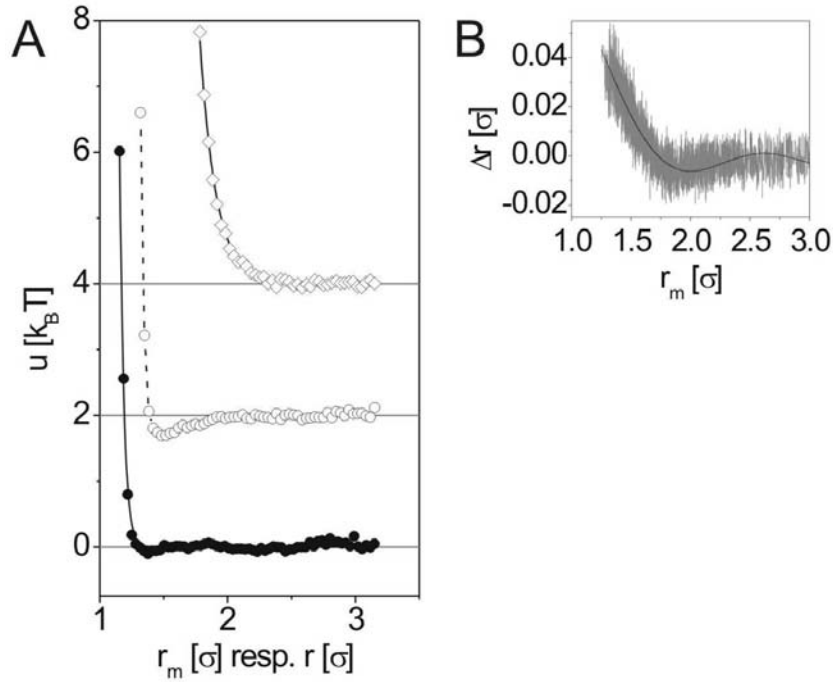


FIGURE 7.8. A) Uncorrected pair potentials measured under unconfined conditions (sample type I, see Section 3.3) for ionic conductivity of $4\mu S/cm$ (diamonds) and $0.8\mu S/cm$ (open circles). After correcting the data (open circles) for imaging artifacts (Δr vs. r_m shown in Figure B) we obtain the lower potential (closed circles). The solid lines are fits to the Yukawa potential (2.10), the dashed line is a guide to the eye. The solid line in Figure B is a polynomial fit.

in Figure 7.5 denote the change of Δr upon variation of the applied intensity threshold T by $\pm 10\%$ and indicate that the threshold value has (within certain limits) only a small influence on Δr . Interestingly, such calculations have already been performed earlier [173]. However, the particle images were modeled by parabolic caps which then resulted in a monotonic behavior of $\Delta r(r_m)$. Our results thus clearly demonstrate that the change in sign of $\Delta r(r_m)$ is crucial to induce an apparent attractive part in the pair interaction. At this point, it is important to mention that the calculation of correction curves by superimposing one-particle images incoherently does not work in general. For instance, we have failed to correct pair potentials obtained from measurements under fluorescent conditions; however, the measurement of the correction curve by means of a stuck and a mobile particle is applicable in general.

So far, we have demonstrated that overlapping particle images lead to an apparent attractive component in the pair interaction. However, an essential aspect is still missing in order to explain all features of LCA; why has LCA been observed exceptionally under confined conditions if it is really caused by an optical artifact? This can be easily explained by recalling (2.9). The screening length κ^{-1} inversely depends on the

concentrations c_{i0} of salt ions and counter ions. If the spacing between the confining plates of the sample cell is decreased the concentrations c_{i0} grow and κ^{-1} is therefore getting smaller. The particle image thus overlap under confined conditions due to the reduced strength of the pair interaction compared to unconfined conditions. As a result, LCA should also be observable in unconfined samples at high salt concentrations. To explore this idea, we measured the pair interaction at different salt concentrations in thick sample cells (sample type I, see Section 3.5). Figure 7.8 (diamonds) shows the pair interaction $u(r)$ obtained under rather deionized conditions (ionic conductivity $0.8\mu S/cm$). Particle distances below 2σ are hardly sampled and as expected the data agree well with a screened Coulomb potential. From a fit we obtain $Z \approx 15900 \pm 1200$ and $\kappa^{-1} \approx 190 \pm 5nm$. Increasing the salt concentration (corresponding to an ionic conductivity of $4\mu S/cm$) leads to a shift of the potential to smaller distances (open circles). In addition, however, the uncorrected potential exhibits a pronounced minimum. Again, the depth and position of this minimum is in excellent agreement with the characteristics of LCA but is here observed in the absence of confinement. Applying the correction procedure as described above, eventually leads to perfect agreement with a screened Coulomb potential with $Z \approx 18700 \pm 1500$ and $\kappa^{-1} \approx 55 \pm 5nm$ (closed circles). Finally we calculated the bare charge Z_{bare} obtained from Z and κ^{-1} using an analytical expression based on the Poisson-Boltzmann mean-field theory [177] and obtain $Z_{bare} = 19210$ and 19275 for the low and high ionic concentrations, respectively. The almost perfect agreement is an independent consistency check for the corrected $u(r)$ and demonstrates that the obtained parameters are correct. Besides, our explanation is also consistent with an observation made in the first paper on LCA where it was reported that even under confinement, a minimum is only observed for sufficiently high ionic concentrations [39].

7.5. METHODS TO AVOID OPTICAL DISTORTIONS

In the following, we explore possible strategies which allow to avoid imaging artifacts instead of correcting them. This is of particular importance for dense colloidal systems where more than two particle images overlap. In this case, both the measurement and the calculation of the correction curve are rather elaborate.

To measure true particle distances, one must avoid the overlap of particle images which are the source of erroneous distance measurements. One approach is to use core-shell particles where e.g. the core is labeled with a fluorescent dye or where the shell is matched exactly to the solvent [13]. For sufficiently large shell thicknesses, in both cases the particle image can be smaller than its geometrical size. This would avoid artefacts even when the particles are in physical contact. The insets of Figure 7.9 shows a highly diluted system of silica spheres with a fluorescent (fluorescein isothiocyanate, FITC) core. The core diameter was $400nm$ and the total radius $1.4\mu m$. In the fluorescence

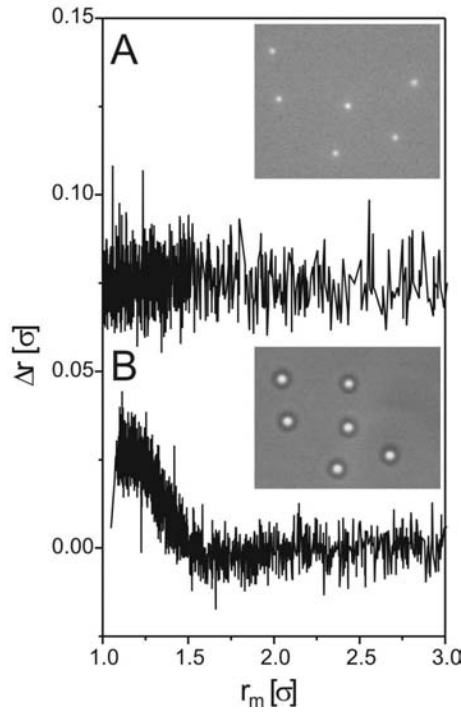


FIGURE 7.9. Δr vs. r_m for core-shell particles with a fluorescent core: A) fluorescent illumination (the data are shifted in vertical direction by 0.075σ) and B) bright-field illumination. The insets display typical snapshots.

image (upper inset) the particles appear even smaller than their geometrical size. As expected, in this case the Δr vs. r_m curve (Figure 7.9A) scatters symmetrically around zero and shows no particular structure (note that the increased noise is due to the smaller particle image [89]). In contrast, white light illumination again leads to images which are blurred over almost twice the particle diameter, and we again observe the characteristic shape of $\Delta r(r_m)$ (Figure 7.9B).

The second approach does not avoid the overlap of particle images, but rather provides a new bright-field particle detection algorithm which intrinsically accounts for optical distortions. The idea is the following: let \mathbf{x}_i denote the true position of the i -th particle of a N -particle system. A typical video image can then be described as

$$I(\mathbf{x}) = \sum_{i=1}^N I_{1P}(|\mathbf{x} - \mathbf{x}_i|) + I_{Noise}(\mathbf{x}) \quad (7.19)$$

with I_{1P} the one-particle intensity determined from the particle image cross section (Figure 7.6). I_{Noise} accounts for noise which is mostly caused by the electronic noise of

the CCD camera chip. The expression (7.19) can be written as

$$\begin{aligned} I(\mathbf{x}) &= \sum_{i=1}^N \delta(\mathbf{x}' - (\mathbf{x} - \mathbf{x}_i)) I_{1P}(|\mathbf{x}'|) + I_{Noise}(\mathbf{x}) \\ &= \sum_{i=1}^N \rho(\mathbf{x} - \mathbf{x}') I_{1P}(\mathbf{x}') + I_{Noise}(\mathbf{x}), \end{aligned} \quad (7.20)$$

with $\rho(\mathbf{x})$ the true particle density,

$$\rho(\mathbf{x}) = \sum_{i=1}^N \delta(\mathbf{x} - \mathbf{x}_i). \quad (7.21)$$

We apply the convolution theorem to (7.20) and obtain

$$\tilde{I}(\mathbf{q}) = \tilde{\rho}(\mathbf{q}) \tilde{I}_{1P}(\mathbf{q}) + \tilde{I}_{Noise}(\mathbf{q}) \quad (7.22)$$

where the tilde refers to the Fourier amplitudes and \mathbf{q} denotes the wave vector. With this, it follows that

$$\tilde{\rho}(\mathbf{q}) = \frac{\tilde{I}(\mathbf{q}) - \tilde{I}_{Noise}(\mathbf{q})}{\tilde{I}_{1P}(\mathbf{q})}. \quad (7.23)$$

Since the right-hand side of this expression can be determined from video images, the true particle positions can be obtained by deconvolution.

7.6. OPTICAL BINDING

In the following we focus on an effect termed optical binding (OB) which as LCA has been discussed controversially during the last 20 years. Here, a strong light field induces alternating attractive and repulsive components in the colloidal pair interaction. We therefore had to check whether OB plays a role in our experiments.

OB can be understood as follows: we consider a single dielectric particle in a strong electrical field \mathbf{E} and denote the wave vector as \mathbf{k} . The electric field induces an oscillating dipole moment \mathbf{p} in the particle which gives rise to scattering (Mie scattering in the case of colloidal particles [172, 176, 178]). In the presence of a second particle, the dipole induced in the first sphere interacts with the gradient of the electrical field scattered by the second sphere and vice versa. Solving the Maxwell equations yields an approximate analytical expression for the interaction energy depending on the electrical field polarization [171]. If the polarization is perpendicular to the particle distance vector \mathbf{r} , the analytical expression explicitly becomes

$$W = -\frac{1}{2} \alpha^2 \mathbf{E}^2 \mathbf{k}^2 \frac{\cos(\mathbf{k} \cdot \mathbf{r})}{r} \quad (7.24)$$

with α the polarizability and $r = |\mathbf{r}|$. Accordingly, the two dielectric particles experience an alternating attractive and repulsive force depending on the distance r ; note that the oscillation period equals the electric field wavelength $\lambda = 2\pi/|\mathbf{k}|$.

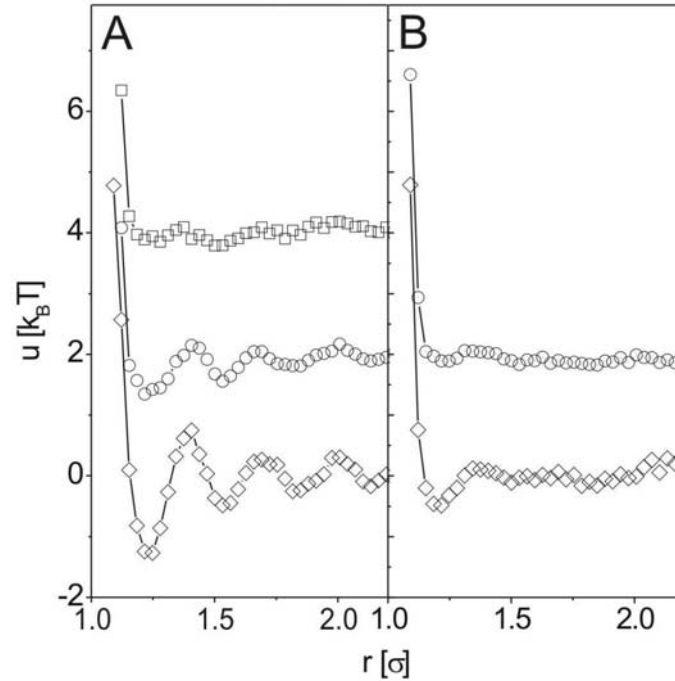


FIGURE 7.10. Pair interaction $u(r)$ in the presence of a strong light-field versus distance r measured with video microscopy (the solid lines are a guide to the eye); the light-field is a line shaped focus created through the use of two cylindrical lenses [171]. A) The laser beam polarization is perpendicular to the line shaped focus and the laser powers are $P = 0.2W$ (squares), $P = 0.4W$ (circles), and $P = 0.8W$ (diamonds). B) The laser beam polarization is parallel to the line shaped focus and the laser powers are $P = 0.4W$ (circles) and $P = 0.8W$ (diamonds).

In their pioneering work, Burns et al. performed experimental studies on OB and subjected two polystyrene spheres ($\sigma = 1.43\mu m$) to a line shaped light potential created through the use of two cylindrical lenses (see [171] for details). As a result, the particle distance histogram evaluated along the line potential clearly revealed the oscillatory structure as expected from (7.24). The existence of OB has therefore been proved experimentally, but no effort has been employed to investigate OB systematically. In particular, the electrical field strength required to induce OB has not yet been measured.

We repeated the experiment of Burns et al. and evaluated the pair interaction according to the procedure described in Section 7.3; the extension to line shaped light potentials is straightforward where (7.1) must be substituted by $u_{ext}(\mathbf{x}) = a_{ext,x}x^2 + a_{ext,y}y^2$ with $\mathbf{x} = (x, y)$. Our results are shown in Figure 7.10A and the laser powers from top to bottom are $P = 0.2W$, $P = 0.4W$, and $P = 0.8W$. As can be seen, the pair potentials clearly confirm the existence of OB and show that OB occurs at powers between $P = 0.2W$ and $P = 0.4W$. Concerning our studies on LCA where $P = 0.05W$, we must recall that the laser beam creating the light potential was defocused in contrast

to the experiments on OB; we can therefore conclude that the potential strength in LCA measurements has considerably been too small (leastwise an order of magnitude) to induce OB effects.

The pair potentials shown in Figure 7.10B are obtained if the electrical field polarization is parallel to the line trap. Here, the OB effect is reduced tremendously since the oscillating dipole moments scatter the least in the oscillation direction.

In addition, our studies on OB are of general relevance for experiments employing strong laser fields to create extended light potentials [8–11, 179, 180]. For instance, it has not been definitely proven to date that OB does not affect the results of experimental studies on light-induced freezing and melting [8–11]; our studies on OB now demonstrate that the strengths of extended light potentials are by far too weak to induce OB.

7.7. CONCLUSIONS

We have experimentally determined colloidal pair interactions by confining two colloidal particles in a circular light trap and inverting the measured distance distribution. As a result, we observed LCA similarly to previous studies done on the subject; however, we could demonstrate that LCA is caused by an optical artifact arising from overlapping particle images and causing erroneous distance measurements. We have also shown that LCA is not a confinement effect; the observation of LCA only requires sufficiently high screening of the repulsive Yukawa interaction to allow overlap of particle images. Accordingly, we also found LCA in the case of unconfined samples at sufficiently high salt concentrations. In addition, we provided a couple of strategies to account for optical artifacts; first, optical distortions can be measured to correct measured distances and can be calculated in the case of bright-field microscopy, and second, optical distortions are intrinsically avoided through fluorescent imaging of core-shell particles with a fluorescent core and through a new deconvolution method for particle detection under bright-field conditions.

In the meanwhile, two groups reported further mechanisms that might be responsible for LCA; first, Monte-Carlo studies have uncovered attractive contributions to colloidal pair interactions arising from polydispersity [170] and second, it has been shown in [181] that inversion procedures based on closure relations (see Section 2.4) can produce apparent attractive interactions. Moreover, the pair correlation function of a confined dilute colloidal system has been recently measured using core-shell particles [182]. As a result, a purely short-ranged repulsive behavior was observed in the case of fluorescent illumination. In contrast, the pair correlation function exhibited deviations under bright-field conditions pretending apparent attractive interactions.

8

Summary

We used colloids as model systems for condensed matter employing charged-stabilized colloidal suspensions, optical tweezers and video microscopy. In charged colloidal suspensions, particles interact via a repulsive screened Coulomb potential with the screening length determined through the concentration of salt ions. Optical tweezers refer to strong laser-intensity fields which allow trapping of dielectric colloids in regions of maximum intensity. We used optical tweezers to induce extended 2D substrates by means of overlapping expanded laser beams. In addition, we controlled the particle density with a scanned focused laser beam creating 1D boundary potentials. Particle trajectories were measured with video microscopy and we determined pair interactions, pair correlation functions, mean-square displacements and nearest-neighbor bonds from the trajectories.

In this thesis, we have presented the following theoretical and experimental studies: we first determined the phonon band structure of 2D triangular colloidal crystals in the presence of commensurate 1D and 2D periodic substrates. The numerical studies were based on the harmonic approximation where springs describe both the particle pair interaction and the particle-substrate interaction. Our results demonstrate that a substrate can both shift and deform phonon-band structures and, in addition, can even induce band gaps. As a consequence, a substrate can modify sound and thermal properties which both crucially depend on the phonon-band structure. In the experiments, we prepared a 2D triangular crystal under highly deionized conditions and created 1D and 2D periodic substrates by means of two overlapping expanded laser beams. The phonon-band structure was determined from the measured particle trajectories and our experimental results confirm the theoretical findings. Moreover, we theoretically investigated phonon dynamics. As a result, we found that a Laplace transformation relates

the mean-square displacement to the phonon spectrum. The experimental verification of this relation is subject of future research.

We then investigated the structural properties of a binary colloidal hard-sphere mixture using confocal microscopy. Our results confirm the existence of structural crossover, an effect predicted by theoretical studies employing density-functional theory and the Ornstein-Zernike formalism. Structural crossover refers to a marked change in the wavelength of damped oscillatory pair correlation functions; depending on the packing fraction of the two particle species, the wavelength is slightly larger than the diameter of either the big or the small particles. Furthermore, we found that structural crossover is related to the size of networks consisting of only equally sized particles connected through nearest-neighbor bonds. This is supported by Monte-Carlo simulations which were performed at different ratios of the particle sizes and total packing fractions.

Next, we studied single-particle diffusion on a quasicrystalline light-induced substrate. As a result, we observed subdiffusive behavior characterized through an increase of the mean-square displacement in time according to a power law with the power smaller than unity. We interpreted the subdiffusive particle motion as a thermalization process; to thermalize, the particle must explore the entire distribution of potential well depth which is characteristic for non-periodic quasicrystalline substrates. In addition, we found normal diffusion at large times when the particle has thermalized. Our experiments were paralleled by theoretical studies employing Brownian dynamics simulations and rate equations. The numerical results agree qualitatively with the experimental findings.

We finally focused on confinement-induced like-charge attraction, a mysterious phenomenon since an anomalous long-ranged attractive pair interaction is observed in confined charged colloidal suspensions. Two particles were subjected to a radially symmetric light-induced trap and the measured particle-distance distribution yielded the pair interaction. As a result, we found that like-charge attraction is caused by an optical artifact arising from overlapping particle images and leading to erroneous distance measurements. The corrected pair potentials show excellent agreement with mean-field theories. This clearly manifests that the pair interaction in charged colloidal suspensions is indeed purely repulsive. Moreover, we demonstrated that the role of confinement is simply associated with a strong screening of the repulsive interaction which leads to overlapping images. We finally demonstrated that one can avoid optical artifacts through the use of core-shell particles or a particle-detection algorithm based on particle-image deconvolution.

Bibliography

- [1] J. M. Kosterlitz and D. J. Thouless. Long range order and metastability in two dimensional solids and superfluids. *J. Phys. C*, 5:L124, 1972.
- [2] D. R. Nelson and B. I. Halperin. Dislocation-mediated melting in two dimensions. *Phys. Rev. B*, 19(5):2457, 1979.
- [3] A. P. Young. Melting and the vector coulomb gas in two dimensions. *Phys. Rev. B*, 19(4):1855, 1979.
- [4] K. Zahn, R. Lenke, and G. Maret. Two-stage melting of paramagnetic colloidal crystals in two dimensions. *Phys. Rev. Lett.*, 82(13):2721, 1999.
- [5] C. Eisenmann, U. Gasser, P. Keim, G. Maret, and H. H. von Grünberg. Pair interaction of dislocations in two-dimensional crystals. *Phys. Rev. Lett.*, 95:185502, 2005.
- [6] J. Chakrabarti, H. R. Krishnamurthy, and A. K. Sood. Density functional theory of laser-induced freezing in colloidal suspensions. *Phys. Rev. Lett.*, 73 [Issue 21 (21):2923, 1994.
- [7] L. Radzihovsky, E. Frey, and D. R. Nelson. Novel phases and reentrant melting of two-dimensional colloidal crystals. *Phys. Rev. E*, 63(3):031503, 2001.
- [8] A. Chowdhury, B. J. Ackerson, and N. A. Clark. Laser-induced freezing. *Phys. Rev. Lett.*, 55(8):833, 1985.
- [9] Q. H. Wei, C. Bechinger, D. Rudhardt, and P. Leiderer. Experimental study of laser-induced melting in two-dimensional colloids. *Phys. Rev. Lett.*, 81(12):2606, 1998.
- [10] C. Bechinger, M. Brunner, and P. Leiderer. Phase behavior of two-dimensional colloidal systems in the presence of periodic light fields. *Phys. Rev. Lett.*, 86(5):930, 2001.
- [11] J. Baumgartl, M. C. Brunner, and C. Bechinger. Locked-floating-solid to locked-smectic transition in colloidal systems. *Phys. Rev. Lett.*, 93:168301, 2004.
- [12] R. H. Webb. Confocal optical microscopy. *Rep. Prog. Phys.*, 59:427, 1996.
- [13] A. van Blaaderen and P. Wiltzius. Real-space structure of colloidal hard-sphere glasses. *Science*, 270:1177, 1995.
- [14] E. R. Weeks, C. J. Crocker, A. C. Levitt, A. B. Schofield, and D. A. Weitz. Three-dimensional direct imaging of structural relaxation near the colloidal glass transition. *Science*, 287:627, 2000.
- [15] E. R. Weeks and D. A. Weitz. Subdiffusion and the cage effect studied near the colloidal glass transition. *Chem. Phys.*, 284:361, 2002.
- [16] E. R. Weeks and D. A. Weitz. Properties of cage rearrangements observed near the colloidal glass transition. *Phys. Rev. Lett.*, 89:095704, 2002.
- [17] A. van Blaaderen, R. Ruel, and P. Wiltzius. Template-directed colloidal crystallization. *Nature*, 385:321, 1997.
- [18] A. Yethiraj and A. van Blaaderen. A colloidal model system with an interaction tunable from hard sphere to soft and dipolar. *Nature*, 421:513, 2003.
- [19] V. W. A. de Villeneuve, R. P. A. Dullens, D. G. A. L. Aarts, E. Groeneveld, J. H. Scherff, W. K. Kegel, and H. N. W. Lekkerkerker. Colloidal hard-sphere crystal growth frustrated by large spherical impurities. *Science*, 309:1231, 2005.

- [20] J. D. Joannopoulos, P. R. Villeneuve, and S. Fan. Photonic crystals: putting a new twist on light. *Nature*, 405:437, 2000.
- [21] S. Russell, D. A. Saville, and W. R. Schowalter. *Colloidal dispersions*. Cambridge University Press, Cambridge, 1989.
- [22] J. N. Israelachvili. *Intermolecular and surface forces*. Academic Press, London, 1992.
- [23] C. Grodon. Structure and solvation forces in binary hard-sphere mixtures. *Diploma thesis*, 2003.
- [24] D. G. Grier and Y. Han. Anomalous interactions in confined charge-stabilized colloid. *J. Phys.: Condens. Matter*, 16:S4145, 2004.
- [25] A. Ashkin. Acceleration and trapping of particles by radiation pressure. 24:156, 1970.
- [26] A. Ashkin, J. M. Dziedzic, J. E. Bjorkholm, and S. Chu. Observation of a single-beam gradient force optical trap for dielectric particles. *Opt. Lett.*, 11(5):288, 1986.
- [27] A. Ashkin. Forces of a single-beam gradient laser trap on a dielectric sphere in the ray optics regime. *Biophys. J.*, 61(2):61, 1992.
- [28] J. P. Gordon. Radiation forces and momenta in dielectric media. *Phys. Rev. A*, 8(1):14, 1973.
- [29] J. A. Stratton. *Electromagnetic Theory*. McGraw-Hill Book Company, Inc., New York, 1941.
- [30] J. D. Jackson. *Classical Electrodynamics*. Wiley, New York, 1999.
- [31] M. Kerker. *The Scattering of Light and Other Electromagnetic Radiation*. Academic, New York, 1969, 1969.
- [32] K. Loudiyi and B. J. Ackerson. Monte carlo simulation of laser induced freezing. *Physica A*, 184(1-2):26, 1992.
- [33] M. Brunner. Lichtinduziertes gefrieren und schmelzen eines zweidimensionalen kolloidsystems. *Diploma thesis*, 2000.
- [34] R. Bubeck. Zweidimensionale kolloidale systeme in äußeren potentialen. *Ph.D. thesis*, 2001.
- [35] M. E. Briggs, J. V. Sengers, M. K. Francis, P. Gaspardd, R. W. Gammonc, J. R. Dorfmanc, and R. V. Calabrese. Tracking a colloidal particle for the measurement of dynamic entropies. *Physica A*, 296(1-2):42, 2001.
- [36] R. Aveyard and D. A. Haydon. *An Introduction to the Principles of Surface Chemistry*. Cambridge University Press, Cambridge, 1973.
- [37] D. Rudhardt. Kolloidale teilchen in der nähe einer wand. *Ph.D. thesis*, 1999.
- [38] D. Rudhardt, C. Bechinger, and P. Leiderer. Direct measurement of depletion potentials in mixtures of colloids and nonionic polymers. *Phys. Rev. Lett.*, 81(6):1330, 1998.
- [39] G. M. Kepler and S. Fraden. Attractive potential between confined colloids at low ionic strength. *Phys. Rev. Lett.*, 73(2):356, 1994.
- [40] S. H. Behrens and D. G. Grier. Pair interaction of charged colloidal spheres near a charged wall. *Phys. Rev. E*, 64(5):050401, 2001.
- [41] A. Ramirez-Saito, M. Chavez-Paez, J. Santana-Solano, and J. L. Arauz-Lara. Effective pair potential between confined charged colloidal particles. *Phys. Rev. E*, 67(5):050403, 2003.
- [42] J. Baumgartl. Lichtinduzierte phasenübergänge in kolloidalen suspensionen. *Diploma thesis*, 2003.
- [43] M. Zvyagolskaya. Bandstruktur von 2d kolloidkristallen auf periodischen substratpotentialen. *Diploma thesis*, 2007.
- [44] M. Born and K. Huang. *Dynamical theory of crystal lattices*. Clarendon Press, Oxford, 1956.
- [45] H. Ibach and H. Lüth. *Festkörperphysik*. Springer-Verlag Berlin Heidelberg New York, 1999.
- [46] S. E. Trullinger, V. E. Zakharov, and V. L. Prokrovsky. *Solitons*. North-Holland, Amsterdam, 1996.

- [47] L. W. Bruch, M. W. Cole, and E. Zaremba. *Physical adsorption: forces and phenomena*. Clarendon Press, Oxford, 1997.
- [48] K. D. Gibson and S. J. Sibener. Determination of the surface phonon dispersion relations for monolayer, bilayer, trilayer, and thick kr(111) films physisorbed on ag(111) by inelastic he scattering. *Phys. Rev. Lett.*, 55(14):1514, 1985.
- [49] K. D. Gibson, S. J. Sibener, B. M. Hall, D. L. Mills, and J. E. Black. Lattice dynamics of rare gas multilayers on the ag(111) surface: Theory and experiment. *J. Chem. Phys.*, 83(8):4256, 1985.
- [50] R. D. Boutchko and L. W. Bruch. Brownian friction of gas molecules on the graphite surface. *Phys. Rev. B*, 59(16):10992, 1999.
- [51] A. P. Graham, M. F. Bertino, F. Hofmann, J. P. Toennies, and C. Wöll. Experimental determination of a longitudinal phonon dispersion curve in a quasi-two-dimensional system. *J. Chem. Phys.*, 106(14):6194, 1997.
- [52] C. Wöll. Phonons on surfaces: The importance of structure and adsorbates. *Appl. Phys. A*, 53(5):377, 1991.
- [53] R. S. Penciu, G. Fytas, E. N. Economou, W. Steffen, and S. N. Yannopoulos. Acoustic excitations in suspensions of soft colloids. *Phys. Rev. Lett.*, 85(21):4622, 2000.
- [54] R. S. Penciu, M. Kafesaki, G. Fytas, E. N. Economou, W. Steffen, A. Hollingsworth, and W. B. Russel. Phonons in colloidal crystals. *Europhys. Lett.*, 58(5):699, 2002.
- [55] R. S. Penciu, H. Kriegs, G. Petekidis, G. Fytas, and E. N. Economou. Phonons in colloidal systems. *J. Chem. Phys.*, 118(11):5224, 2003.
- [56] H. Kriegs, G. Petekidis, G. Fytas, R. S. Penciu, E. N. Economou, and A. B. Schofield. Phonons in suspensions of hard sphere colloids: Volume fraction dependence. *J. Chem. Phys.*, 121(16):7849, 2004.
- [57] G. Tommaseo, G. Petekidis, W. Steffen, G. Fytas, A. B. Schofield, and N. Stefanou. Hypersonic acoustic excitations in binary colloidal crystals: Big versus small hard sphere control. *J. Chem. Phys.*, 126:014707, 2007.
- [58] Z. Cheng, J. Zhu, W. B. Russel, and P. M. Chaikin. Phonons in an entropic crystal. *Phys. Rev. Lett.*, 85(7):1460, 2000.
- [59] B. V. R. Tata, P. S. Mohanty, M. C. Valsakumar, and J. Yamanaka. Long-wavelength transverse modes in charged colloidal crystals. *Phys. Rev. Lett.*, 93:268303, 2004.
- [60] P. Keim, G. Maret, U. Herz, and H.H. von Grnberg. Harmonic lattice behavior of two-dimensional colloidal crystals. *Phys. Rev. Lett.*, 92:215504, 2004.
- [61] T. Gorishnyy, C. K. Ullal, M. Maldovan, G. Fytas, and E. L. Thomas. Hypersonic phononic crystals. *Phys. Rev. Lett.*, 94:115501, 2005.
- [62] T. Gorishnyy, M. Maldovan, C. Ullal, and E. Thomas. Sound ideas (<http://physicsweb.org/articles/world/18/12/3/1>). *physicsweb*, December, 2005.
- [63] E. L. Thomas, T. Gorishnyy, and M. Maldovan. Phononics: Colloidal crystals go hypersonic. *Nat. Mater.*, 5(10):773, 2006.
- [64] A. Khelif, B. Aoubiza, S. Mohammadi, A. Adibi, and V. Laude. Complete band gaps in two-dimensional phononic crystal slabs. *Phys. Rev. E*, 74:046610, 2006.
- [65] W. Cheng, J. Wang, U. Jonas, G. Fytas, and N. Stefanou. Observation and tuning of hypersonic bandgaps in colloidal crystals. *Nat. Mater.*, 5(10):830, 2006.
- [66] J. K. G. Dhont. *An Introduction to Dynamics of Colloids*. Elsevier New York, 1996.
- [67] W. Nolting. *Grundkurs Theoretische Physik 7 Vielteilchen-Theorie*. Friedr. Vieweg & Sohn Verlagsgesellschaft mbH, Braunschweig/Wiesbaden, 1997.

- [68] Y. N. Ohshima and I. Nishio. Colloidal crystal: beadspring lattice immersed in viscous media. *J. Chem. Phys.*, 114(19):8649, 2001.
- [69] R. E. Peierls. Transition temperatures. *Helv. Phys. Acta*, 7:81, 1934.
- [70] Y. Imry and L. Gunther. Fluctuations and physical properties of the two-dimensional crystal lattice. *Phys. Rev. B*, 3(11):3939, 1971.
- [71] Y. Imry. *CRC Critical Reviews in Solid State and Materials Science*. CRC, West Palm Beach, Fla., 1979.
- [72] D. R. Nelson. *Phase Transitions and Critical Phenomena*. Academic Press, London, 1971.
- [73] P. Bartlett, R. H. Ottewill, and P. N. Pusey. Superlattice formation in binary mixtures of hard-sphere colloids. *Phys. Rev. Lett.*, 68:3801, 1992.
- [74] A. B. Schofield. Binary hard-sphere crystals with the cesium chloride structure. *Phys. Rev. E*, 64:51403, 2001.
- [75] M. D. Eldridge, P. A. Maaden, and D. Frenkel. Entropy-driven formation of a superlattice in a hard-sphere binary mixture. *Nature*, 365:35, 1993.
- [76] D. C. Hong, P. V. Quinn, and S. Luding. Reverse brazil nut problem: Competition between percolation and condensation. *Phys. Rev. Lett.*, 86:3423, 2001.
- [77] T. Eckert and E. Bartsch. Re-entrant glass transition in a colloid-polymer mixture with depletion attractions. *Phys. Rev. Lett.*, 89:125701, 2002.
- [78] D. N. Perera and P. Harrowell. Stability and structure of a supercooled liquid mixture in two dimensions. *Phys. Rev. E*, 59:5721, 1999.
- [79] R. Roth and D. Gillespie. Physics of size selectivity. *Phys. Rev. Lett.*, 95:247801, 2005.
- [80] S. Sastry, T. M. Truskett, P. G. Debenedetti, S. Torquato, and F. H. Stillinger. Free volume in the hard sphere liquid. *Mol. Phys.*, 95:289, 1998.
- [81] W. Poon, P. N. Pusey, and H. N. W. Lekkerkerker. Colloids in suspense. *Physics World*, April:27, 1996.
- [82] C. Grodon, M. Dijkstra, R. Evans, and R. Roth. Decay of correlation functions in hard-sphere mixtures: Structural crossover. *J. Chem. Phys.*, 121:7869, 2004.
- [83] C. Grodon, M. Dijkstra, R. Evans, and R. Roth. Homogeneous and inhomogeneous hard-sphere mixtures: manifestations of structural crossover. *Mol. Phys.*, 103:3009, 2005.
- [84] R. Evans. The nature of the liquid-vapour interface and other topics in the statistical mechanics of non-uniform, classical fluids. *Adv. Phys.*, 28:143, 1979.
- [85] N. D. Mermin. Thermal properties of the inhomogeneous electron gas. *Phys. Rev.*, 137:A1441, 1965.
- [86] Y. Rosenfeld. Free-energy model for the inhomogeneous hard-sphere fluid mixture and density-functional theory of freezing. *Phys. Rev. Lett.*, 63:980, 1989.
- [87] Y. Rosenfeld. Geometrically based density functional theory of liquids. *J. Phys.: Condens. Matter*, 8:9289, 1996.
- [88] R. Evans, R. J. Leote de Carvalho, J. R. Henderson, and D. C. Hoyle. Asymptotic decay of correlations in liquids and their mixtures. *J. Chem. Phys.*, 100:591, 1994.
- [89] C. J. Crocker and D. G. Grier. Methods of digital video microscopy for colloidal studies. *J. Colloid Interface Sci.*, 179(1):298, 1996.
- [90] AY Grosberg and AR Khokhlov. *Statistical Physics of Macromolecules (translated by Atanov YA)*. AIP Press. ISBN 1563960710, 1994.
- [91] P. J. Flory. *Principles of Polymer Chemistry, Cornell University*, 1953.

- [92] C. S. O'Hern, S. A. Langer, A. J. Liu¹, and S. R. Nagel. Force distributions near jamming and glass transitions. *Phys. Rev. Lett.*, 86:111, 2001.
- [93] N. Hoffmann, F. Ebert, C. N. Likos, H. Löwen, and G. Maret. Partial clustering in binary two-dimensional colloidal suspensions. *Phys. Rev. Lett.*, 97:078301, 2006.
- [94] A. Einstein. über die von der molekularkinetischen theorie der wärme geforderte bewegung von in ruhenden flüssigkeiten suspendierten teilchen. *Ann. Phys. (Leipzig)*, 17:549, 1905.
- [95] H. König, R. Hund, K. Zahn, and G. Maret. Experimental realization of a model glass former in 2d. *Eur. Phys. J. E*, 18(3):287, 2005.
- [96] C. Donati, S. C. Glotzer, P. H. Poole, W. Kob, and S. J. Plimpton. Spatial correlations of mobility and immobility in a glass-forming lennard-jones liquid. *Phys. Rev. E*, 60(3):3107, 1999.
- [97] G. Marty and O. Dauchot. Subdiffusion and cage effect in a sheared granular material. *Phys. Rev. Lett.*, 94:015701, 2005.
- [98] R. N. Ghosh. *Mobility and clustering of individual low density lipoprotein receptor molecules on the surface of human skin fibroblasts*. Ph.d. thesis, Cornell University, Ithaca, NY, 1991.
- [99] R. N. Ghosh and W. W. Webb. Automated detection and tracking of individual and clustered cell surface low density lipoprotein receptor molecules. *Biophys. J.*, 66:1301, 1994.
- [100] J. P. Slattery. *Lateral mobility of FCRI on rat basophilic leukemia cells as measured by single particle tracking using a novel bright fluorescent probe*. Ph.d. thesis, Cornell University, Ithaca, NY, 1995.
- [101] T. J. Feder, I. Brust-Mascher, J. P. Slattery, B. Baird, and W. W. Webb. Constrained diffusion or immobile fraction on cell surfaces: a new interpretation. *Biophys. J.*, 70:2767, 1996.
- [102] E. D. Sheets, G. M. Lee, R. Simson, and K. Jacobson. Transient confinement of a glycosylphosphatidylinositol-anchored protein in the plasma membrane. *Biochemistry*, 36:12449, 1997.
- [103] R. Simson, B. Yang, S. E. Moore, P. Doherty, F. S. Walsh, and K. A. Jacobson. Structural mosaicism on the submicron scale in the plasma membrane. *Biophys. J.*, 74:297, 1998.
- [104] P. Schwille, U. Haupts, Sudipta Maiti, and W. W. Webb. Molecular dynamics in living cells observed by fluorescence correlation spectroscopy with one- and two-photon excitation. *Biophys. J.*, 77:2251, 1999.
- [105] P. Schwille, J. Korlach, and W. W. Webb. Fluorescence correlation spectroscopy with single-molecule sensitivity on cell and model membranes. *Cytometry*, 36(3):176, 1999.
- [106] P. R. Smith, I. E. G. Morrison, K. M. Wilson, N. Fernandez, and R. J. Cherry. Anomalous diffusion of major histocompatibility complex class i molecules on hela cells determined by single particle tracking. *Biophys. J.*, 76(6):3331, 1999.
- [107] A. L. Hodgkin and R. D. Keynes. The potassium permeability of a giant nerve fibre. *J. Physiol. (London)*, 128(1):61, 1955.
- [108] E. J. A. Lea. Permeation through long narrow pores. *J. Theor. Biol.*, 5(1):102, 1963.
- [109] H. Rickert. Diffusion through a linear chain (single-file diffusion). *Z. Phys. Chem. Neue Folge*, 43:129, 1964.
- [110] A. C. Levitt. New theory of transport for cell membrane pores. i. general theory and application to red cell. *Biochim. Biophys. Acta*, 373:115, 1974.
- [111] P. A. Rosenberg and A. Finkelstein. Water permeability of gramicidin a-treated lipid bilayer membranes. *J. Gen. Physiol.*, 72:341, 1978.

- [112] S. Draber, R. Schultze, and U.-P. Hansen. Patch-clamp studies on the anomalous mole fraction effect of the K^+ channel in cytoplasmic droplets of *onitella*: An attempt to distinguish between a multi-ion single-file pore and an enzyme kinetic model with lazy state. *J. Membr. Biol.*, 123(2):183, 1991.
- [113] J. A. Hernandez and J. Fischbarg. Kinetic analysis of water transport through a single-file pore. *J. Gen. Physiol.*, 99(4):645, 1992.
- [114] T. Chou and D. Lohse. Entropy-driven pumping in zeolites and biological channels. *Phys. Rev. Lett.*, 82(17):3552, 1999.
- [115] Q.-H. Wei, C. Bechinger, and P. Leiderer. Single-file diffusion of colloids in one-dimensional channels. *Science*, 287:625, 2000.
- [116] C. Lutz, M. Kollmann, and C. Bechinger. Single-file diffusion of colloids in one-dimensional channels. *Phys. Rev. Lett.*, 93(026001), 2004.
- [117] A. M. Lacasta, J. M. Sancho, A. H. Romero, I. M. Sokolov, and K. Lindberg. From subdiffusion to superdiffusion of particles on solid surfaces. *Phys. Rev. E*, 70:051104, 2004.
- [118] J. Honkonen and Y. M. Pis'mak. Exact calculation of the anomalous dimension of the diffusion coefficient for a model of a random walk in a random potential. *J. Phys. A: Math. Gen.*, 22:899, 1989.
- [119] A. H. Romero and J. M. Sancho. Brownian motion in short range random potentials. *Phys. Rev. E*, 58(3):2833, 1998.
- [120] J. W. Goodman. Some fundamental properties of speckle. *J. Opt. Soc. Am*, 66(11):1145, 1976.
- [121] D. Babic, C. Schmitt, I. Poberaj, and C. Bechinger. Stochastic resonance in colloidal systems. *Eur. Phys. Lett.*, 67(2):158, 2004.
- [122] M. F. Shlesinger, G. M. Zaslavsky, and J. Klafter. Strange kinetics. *Nature*, 363:31, 1993.
- [123] E. R. Weeks and H. L. Swinney. Anomalous diffusion resulting from strongly asymmetric random walks. *Phys. Rev. E*, 57(5):4915, 1998.
- [124] C. Das and H. R. Krishnamurthy. Laser-induced quasicrystalline order in charge-stabilized colloidal systems. *Phys. Rev. B*, 58(10):R5889, 1998.
- [125] M. Schmiedeberg, J. Roth, and H. Stark. Freezing and melting of a colloidal adsorbate on a 1d quasicrystalline substrate. *Phys. Rev. Lett.*, 97:158304, 2006.
- [126] H. Brenner. The slow motion of a sphere through a viscous fluid towards a plane surface. *Chem. Eng. Sci*, 16:242, 1961.
- [127] A. J. Goldmann, R. G. Cox, and H. Brenner. Slow viscous motion of a sphere parallel to a plane wall. i. motion through a quiescent fluid. *Chem. Eng. Sci*, 22:637, 1967.
- [128] R. Krause, J. L. Arauz-Lara, G. Nägele, H. Ruiz-Estrada, M. Medina-Noyola, R. Weber, and R. Klein. Statics and tracer-diffusion in binary suspensions of polystyrene spheres: experiment vs. theory. *Physica A*, 178(2):241, 1991.
- [129] R. Krause, G. Nägele, J. L. Arauz-Lara, and R. Weber. Brownian motion in binary colloidal suspensions. *J. Coll. Int. Sci*, 148(231):347, 1992.
- [130] G. Nägele, T. Zwick, R. Krause, and R. Klein. Brownian motion in polydisperse charged colloidal suspensions. *J. Coll. Int. Sci*, 161:347, 1993.
- [131] H. A. Makse, S. Havlin, M. Schwartz, and H. E. Stanley. Method for generating long-range correlations for large systems. *Phys. Rev. E*, 53(5):5445, 1996.
- [132] E. Koscielny-Bunde, A. Bunde, S. Havlin, H. E. Roman, Y. Goldreich, and H.-J. Schnellhuber. Indication of a universal persistence law governing atmospheric variability. *Phys. Rev. Lett.*, 81(3):729, 1998.

- [133] H. A. Kramer. Brownian motion in a field of force and the diffusion model of chemical reactions. *Physica*, 7(4):284, 1940.
- [134] J. W. Haus, K. W. Kehr, and J. W. Lyklema. Diffusion in a disordered medium. *Phys. Rev. B*, 25(4):2905, 1982.
- [135] J. W. Haus and K. W. Kehr. Diffusion in regular and disordered lattices. *Phys. Rep.*, 150(5-6):263, 1987.
- [136] C. Janot. *Quasicrystals - a primer*. Oxford University Press, 1995.
- [137] J. Mikhael, L. Helden, and C. Bechinger. work in progress. 2007.
- [138] B. V. Derjaguin and L. Landau. Theory of the stability of strongly charged lyophobic sols and the adhesion of strongly charged particles in solutions of electrolytes. *Acta Physico-chimica (URSS)*, 14:633, 1941.
- [139] E. J. W. Verwey and J. Overbeek. *Theory of the Stability of Lyophobic Colloids*. Elsevier, Amsterdam, 1948.
- [140] C. J. Crocker and D. G. Grier. Microscopic measurement of the pair interaction potential of charge-stabilized colloid. *Phys. Rev. Lett.*, 73(2):352, 1994.
- [141] K. Vondermassen, J. Bongers, A. Mueller, and H. Versmold. Brownian motion: A tool to determine the pair potential between colloid particles. *Langmuir*, 10:1351, 1994.
- [142] M. Brunner, J. Dobnikar, H.H. von Grünberg, and C. Bechinger. Direct measurement of three-body interactions amongst charged colloids. *Phys. Rev. Lett.*, 92:078301, 2004.
- [143] K. Ito, H. Yoshida, and N. Ise. Void structure in colloidal dispersions. *Science*, 263:66, 1994.
- [144] A. E. Larsen and D. G. Grier. Melting of metastable crystallites in charge-stabilized colloidal suspensions. *Phys. Rev. Lett.*, 76(20):3862, 1996.
- [145] A. E. Larsen and D. G. Grier. Like-charge attractions in metastable colloid crystallites. *Nature*, 385:230, 1997.
- [146] C. J. Crocker and D. G. Grier. When like charges attract: The effects of geometrical confinement on long-range colloidal interactions. *Phys. Rev. Lett.*, 77(9):1897, 1996.
- [147] T. M. Squires and M. P. Brenner. Like-charge attraction and hydrodynamic interaction. *Phys. Rev. Lett.*, 85(23):4976, 2000.
- [148] M. D. Carbajal-Tinoco, F. Castro-Roman, and J. L. Arauz-Lara. Static properties of confined colloidal suspensions. *Phys. Rev. E*, 53(4):3745, 1996.
- [149] H. Acuna-Campa, M. D. Carbajal-Tinoco, J. L. Arauz-Lara, and M. Medina-Noyola. Collective dynamics in quasibidimensional colloidal suspensions. *Phys. Rev. Lett.*, 80(26):5802, 1998.
- [150] D. G. Grier and Y. Han. Confinement-induced colloidal attractions in equilibrium. *Phys. Rev. Lett.*, 91(3):038302, 2003.
- [151] H. M. Ho, B. Cui, S. Repel, B. Lin, and S. A. Rice. Influence of a depletion interaction on dynamical heterogeneity in a dense quasi-two-dimensional colloid liquid. *J. Chem. Phys.*, 121(17):8627, 2004.
- [152] W. van Meegen and S. M. Underwood. Tracer diffusion in concentrated colloidal dispersions. ii. non-gaussian effects. *J. Chem. Phys.*, 88(12):7841, 1988.
- [153] G. Nägele, M. Medina-Noyola, R. Klein, and J. L. Arauz-Lara. Time-dependent self-diffusion in model suspensions of highly charged brownian particles. *Physica A*, 149(1-2):123, 1987.
- [154] R. Krause, G. Nägele, D. Karrer, J. Schneider, R. Klein, and R. Weber. Structure and self-diffusion in dilute suspensions of polystyrene spheres: Experiment vs. computer simulation and theory. *Physica A*, 153(3):400, 1988.

- [155] J. C. Neu. Wall-mediated forces between like-charged bodies in an electrolyte. *Phys. Rev. Lett.*, 82(5):1072, 1999.
- [156] J. E. Sader and D. Y. C. Chan. Long-range electrostatic attractions between identically charged particles in confined geometries: An unresolved problem. *J. Coll. Int. Sci.*, 213(1):268, 1999.
- [157] J. E. Sader and D. Y. C. Chan. Long-range electrostatic attractions between identically charged particles in confined geometries and the poisson-boltzmann theory. *Langmuir*, 16:324, 2000.
- [158] E. Trizac and J. L. Raimbault. Long-range electrostatic interactions between like-charged colloids: Steric and confinement effects. *Phys. Rev. E*, 60(6):6530, 1999.
- [159] E. Trizac. Effective interactions between like-charged macromolecules. *Phys. Rev. E*, 62(2):R1465, 2000.
- [160] A. Gopinathan, T. Zhou, S. N. Coppersmith, L. P. Kadanoff, and D. G. Grier. Weak long-ranged casimir attraction in colloidal crystals. *Europhys. Lett.*, 57:451, 2002.
- [161] P. Attard. Recent advances in the electric double layer in colloid science. *Cur. Opin. Colloid Interface Sci.*, 6(4):366, 2001.
- [162] D. Goulding and J. P. Hansen. Attraction between like-charged colloidal particles induced by a surface: A density-functional analysis. *Europhys. Lett.*, 46(3):407, 1999.
- [163] D. Goulding and J. P. Hansen. Effective interaction between charged colloidal particles near a surface. *Mol. Phys.*, 95(3):649, 1998.
- [164] E. M. Mateescu. Comment on long-range electrostatic interactions between like-charged colloids: Steric and confinement effects. *Phys. Rev. E*, 64(1):013401, 2001.
- [165] J. G. Kirkwood and J. C. Poirier. The statistical mechanics basis of the debye-hueckel theory of strong electrolytes. *J. Chem. Phys.*, 58:591, 1954.
- [166] R. Hastings. On the crystalization of macroionic solutions. *J. Chem. Phys.*, 68:675, 1978.
- [167] J. C. Butler, T. Angelini, J. X Tang, and G. C. L. Wong. Ion multivalence and like-charge polyelectrolyte attraction. *Phys. Rev. Lett.*, 91(2):028301, 2003.
- [168] D. G. Grier and Y. Han. Configurational temperature of charge-stabilized colloidal monolayers. *Phys. Rev. Lett.*, 92:148301, 2004.
- [169] V. Lobaskin, M. Brunner, C. Bechinger, and H.H. von Grünberg. On the nature of long-range contributions to pair interactions between charged colloids in two dimensions. *J. Phys.: Condens. Matter*, 15:6693, 2003.
- [170] T. O. Pangburn and M. A. Bevan. Role of polydispersity in anomalous interactions in electrostatically levitated colloidal systems. *J. Chem. Phys.*, 123:174904, 2005.
- [171] M. M. Burns, J.-M. Fournier, and J. A. Golovchenko. Optical binding. *Phys. Rev. Lett.*, 63(12):1233, 1989.
- [172] B. Ovrzyn and S. H. Izen. Imaging of transparent spheres through a planar interface using a high-numerical optical microscope. *J. Opt. Soc. Am. A*, 17(7):1202, 2000.
- [173] R. Verma, C. J. Crocker, T. C. Lubensky, and A. G. Yodh. Attractions between hard colloidal spheres in semi-flexible polymer solutions. *Macromolecules*, 33:177, 2000.
- [174] G. C. d. Len, J. M. Saucedo-Solorio, and J. L. Arauz-Lara. Colloidal interactions in partially quenched suspensions of charged particles. *Phys. Rev. Lett.*, 81:1122, 1998.
- [175] M. M. Baksh, M. Jaros, and J. T. Groves. Detection of molecular interactions at membrane surfaces through colloid phase transitions. *Nature*, 427:139, 2004.
- [176] B. Ovrzyn. Three-dimensional forward scattering particle image velocimetry applied to a microscopic field-of-view. *Exp. Fluids*, 29(7):S175, 2000.

- [177] M. Aubouy, E. Trizac, and L. Bocquet. Effective charge versus bare charge: an analytical estimate for colloids in the infinite dilution limit. *J. Phys. A: Math. Gen.*, 36:5835, 2003.
- [178] G. Mie. Contributions to the optics of turbid media, especially colloidal metal solutions. *Ann. Phys. (Leipzig)*, 25:377, 1908.
- [179] M. C. Brunner and C. Bechinger. Phase behavior of colloidal molecular crystals on triangular light lattices. *Phys. Rev. Lett.*, 88(24):248302, 2002.
- [180] S. Bleil, H. H. von Grünberg, J. Dobnikar, R. Castaneda-Priego, and C. Bechinger. Strain-induced domain formation in two-dimensional colloidal systems. *Eur. Phys. Lett.*, 73:450, 2006.
- [181] R. N. Behera and P. Gupta-Bhaya. On attractive interaction of a colloid pair of like charge at infinite dilution. *J. Chem. Phys.*, 126:044908, 2007.
- [182] A. Ramirez-Saito, C. Bechinger, and J. L. Arauz-Lara. Optical microscopy measurement of pair correlation functions. *Phys. Rev. E*, 74:030401, 2006.

Acknowledgement

The following people are acknowledged:

- Prof. Dr. Clemens Bechinger (for initializing, supervising and guiding the projects presented in this thesis).
- Chapter 4: Maria Zvyagolskaya (for producing the very nice experimental results) and Prof. Dr. Hans Henning von Grünberg (for theoretical supervision of the project).
- Chapter 5: Dr. Roel P. A. Dullens (for participating in the experiments and on analyzing and discussing the results), Prof. Dr. Clemens Bechinger (for the great idea to perform the connectivity analysis), Dr. Marjolein Dijkstra (for the MC simulation data and for discussing the results), Dr. Roland Roth, Christian Grodon and Prof. Dr. Robert Evans (for having a critical view on the experimental results from a theoretical point of view), and Jules Mikhael (for performing test measurements on 2D samples).
- Chapter 6: Michael Schmiedeberg and Prof. Dr. Holger Stark (for designing, performing and developing the theoretical study and for all the helpful and fruitful discussions), and Priv.-Doz. Dr. Johannes Roth (for helpful ideas and discussions).
- Chapter 7: Dr. Jose-Luis Arauz-Lara (for having a critical view on our results), Dr. Laurent Helden (for the great idea to measure optical artifacts by means of stuck particles), Dr. Dusan Babic and Valentin Blickle (for helpful discussions and comments), Angeles Ramirez-Saito (for sample preparation), Carlos van Kats, and Prof. Dr. Alfons van Blaaderen (for providing core-shell particles).

Persönliche Danksagung:

Ich bedanke mich ganz herzlich bei allen, die zum Gelingen dieser Doktorarbeit beigetragen haben.

Mein ganz besonderer Dank gilt Prof. Clemens Bechinger, der mir die Durchführung einer Doktorarbeit unter hervorragenden Bedingungen ermöglicht und mich sehr gefördert hat. Durch sein Vertrauen und seine Motivation, durch seine immer hilfreichen Kommentare und Ratschläge sowie insbesondere durch seine Spürnase für interessante Projekte konnte ich in den letzten dreieinhalb Jahren Physik so erleben, wie ich Physik erleben möchte; als spannende und fordernde Wissenschaft, die ihre Geheimnisse immer dann preisgibt, wenn man sich am meisten darüber freut. Bedanken möchte ich mich auch für die Hilfe beim Erstellen dieses Manuskripts.

Sehr viel Freude hat mir auch die Zusammenarbeit mit Prof. Hans Henning von Grünberg bereitet. Den kommenden gemeinsamen Studien blicke ich mit sehr viel Motivation und Zuversicht entgegen.

Bei Prof. Tilman Pfau bedanke ich mich, dass er sich als Zweitgutachter zur Verfügung gestellt hat.

Prof. David Marr danke ich für das Korrekturlesen des Manuskripts und die vielen hilfreichen Hinweise und Verbesserungsvorschläge.

Die letzten eineinhalb Jahre hat mich Roel P. A. Dullens – ein äußerst kompetenter und sympathischer Zeitgenosse – tatkräftig unterstützt. Danke für all die guten Ideen und fruchtbaren Diskussionen.

An dieser Stelle möchte ich Matthias Brunner noch einmal meinen Dank aussprechen. Er hat mich während meiner Diplomarbeit direkt betreut und meine Doktorarbeit auf ein sehr solides Fundament gestellt.

Maria Zvyagolskaya danke ich für ihren unglaublichen und erfolgreichen Einsatz während ihrer Diplomarbeit, von dem ich sehr profitiert habe.

Roland Roth danke ich für seine außerordentliche Geduld, die sich in $n = 52$ widerspiegelt.

Meinen Kollegen danke ich für die Unterstützung und die nette Arbeitsatmosphäre. Ich möchte mich insbesondere bei Dusan Babic und meinen langjährigen Wegbegleitern Stefan Bleil und Valentin Blickle, seines Zeichens bester Büronachbar der Welt, bedanken.

Die morgendliche Kaffeerrunde mit Ulrike Offenbeck, Christa Mayer, Denis Kobasevic und Uwe Rau hat mir stets einen entspannten Start in den Tag ermöglicht. Dafür und für die professionelle Unterstützung bedanke ich mich bei den Beteiligten ganz herzlich.

Ich danke außerdem den “Stuttgartern” Andreas Heidebrecht, Robert Schumann und Hermann Neumann, die den neuen “Konstanzer” Kollegen einen netten Empfang bereitet und diese dann tatkräftig unterstützt haben.

Meiner Familie danke ich ganz besonders für die langjährige Unterstützung, das Vertrauen und den moralischen Rückhalt.

Zu guter Letzt möchte ich mich bei all den Menschen bedanken, die mich mit ihrer Musik beglücken. Stellvertretend für viele danke ich “Blind Guardian” für “Somewhere far beyond” und die vier darauf folgenden Meisterwerke.

...and then there was silence...

Erklärung

Hiermit erkläre ich, dass ich die vorliegende Arbeit selbstständig verfasst und keine anderen als die angegebenen Quellen und Hilfsmittel verwendet habe.

Stuttgart, den 7. Mai 2007

Jörg Baumgartl

Lebenslauf

Jörg Baumgartl

Diplom-Physiker

*20. Oktober 1977 in Basel (CH)

Forstraße 156A

70193 Stuttgart

Tel.: +49 (0)711 685 65220, +49 (0)711 6938703

Email: j.baumgartl@physik.uni-stuttgart.de

Familienstand: ledig

Staatsangehörigkeit: Deutsch

- | | |
|-------------------|---|
| 10/1998 - 11/2003 | Physikstudium, Universität Konstanz.
Abschluss des Diplom-Studiengangs Physik.
Prüfung und Anfertigung der Diplomarbeit, Thema:
<i>“Lichtinduzierte Phasenübergänge in kolloidalen Suspension”</i> . |
| 03/2002-10/2002 | Wissenschaftliche Hilfskraft am Lehrstuhl von
Prof. Dr. P. Leiderer,
Fachbereich Physik, Universität Konstanz. |
| 12/2003-heute | Wissenschaftlicher Mitarbeiter
am 2. Physikalischen Institut der Universität Stuttgart,
Leitung: Prof. Dr. C. Bechinger.
Durchführung von physikalischen Experimenten
im Rahmen einer Dissertation. |
| 3/2006 | Forschungsaufenthalt bei Prof. Dr. H. H. von Grünberg,
Karl-Franzens-Universität, Graz (A). |
| 12/2003-heute | Betreuung von Studenten im Fortgeschrittenen-Praktikum
der Universität Stuttgart. |